DEVELOPMENT OF PERMANENT MAGNET BASED HELICON PLASMA SOURCE

By

ARUN PANDEY

ENGG06201404004

INSTITUTE FOR PLASMA RESEARCH, BHAT

GANDHINAGAR 382428, INDIA

A thesis submitted to the
Board of Studies in Engineering Sciences

In partial fulfillment of the requirements

For the Degree of

DOCTOR OF PHILOSOPHY
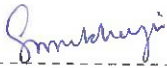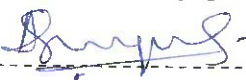
of

HOMI BHABHA NATIONAL INSTITUTE

May, 2019

Homi Bhabha National Institute

## Recommendations of the Viva Voce Committee

As members of the Viva Voce Committee, we certify that we have read the dissertation prepared by **ARUN PANDEY** entitled "Development of permanent magnet based Helicon Plasma Source" and recommend that it may be accepted as fulfilling the thesis requirement for the award of Degree of Doctor of Philosophy.

-- Date : 01 / 05 / 2019
Chairman : Prof. Subrato Mukherjee

-- Date : 01 / 05 / 2019
Guide/ Convener : Dr. Mainak Bandyopadhyay

-- Date : 01 / 05 / 2019
Examiner : Prof. Ashish Ganguli
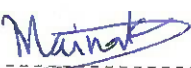
-- Date : 01 / 05 / 2019
Co-Guide : Dr. Shantanu Karkari

-- Date : 01 / 05 / 2019
Member : Prof. Prabal Chattopadhyay

-- Date : 01 / 05 / 2019
Member : Mr. Arun K. Chakraborty

Final approval and acceptance of this thesis is contingent upon the candidate's submission of the final copies of the thesis to HBNI.

I hereby certify that I have read this thesis prepared under my direction and recommend that it may be accepted as fulfilling the thesis requirement.

-- Date : 01 / 05 / 2019
Guide : Dr. Mainak Bandyopadhyay   Place: IPR, Gandhinagar

STATEMENT BY AUTHOR

This dissertation has been submitted in partial fulfillment of requirements for an advanced degree at Homi Bhabha National Institute (HBNI) and is deposited in the Library to be made available to borrowers under rules of the HBNI.

Brief quotations from this dissertation are allowable without special permission, provided that accurate acknowledgement of source is made. Requests for permission for extended quotation from or reproduction of this manuscript in whole or in part may be granted by the Competent Authority of HBNI when in his or her judgement the proposed use of the material is in the interests of scholarship. In all other instances, however, permission must be obtained from the author.

ARUN PANDEY

DECLARATION

I, hereby declare that the investigation presented in the thesis has been carried out by me. The work is original and the work has not been submitted earlier as a whole or in part for a degree/diploma at this or any other Institution or University.

ARUN PANDEY

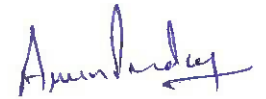# List of Publications arising from the thesis

List of Publications

Publications in Peer Reviewed Journals:

- **Conceptual design of a permanent ring magnet based helicon plasma source module intended to be used in a large size fusion grade ion source**

  A. Pandey, Dass Sudhir, M. Bandyopadhyay, A. Chakraborty. *Fusion Engineering and Design* **103**, 1-7 (2016).

- **Performance evaluation of a permanent ring magnet based helicon plasma source for negative ion source research**

  A. Pandey, M. Bandyopadhyay, Dass Sudhir, A. Chakraborty. *Rev. Sci. Intrum.* **88**, 103509 (2017).

- **Characterization of hydrogen plasma in a permanent ring magnet based helicon plasma source for negative ion source research**

  A. Pandey, D. Mukhopadhyay, M. Bandyopadhyay, Dipshikha Bora, Himanshu Tyagi, Ratnakar Yadav, A. Chakraborty. *Plasma Phys. Control. Fusion* **61** 065003 (2019).

Conferences/Schools:

- **Characterization of the permanent magnet based hydrogen helicon plasma source for ion source application**

  Arun Pandey, Dass Sudhir, M. Bandyopadhyay, A. Chakraborty. 10th *Asian Plasma Fusion Association, December 2015*, Gujarat, India.

- **Helicon Wave field measurements using a B-dot probe in the HELicon Experiment for Negative ion (HELEN-1) source**

  Arun Pandey, M. Bandyopadhyay, Dass Sudhir, A. Chakraborty. 31st *National Symposium on Plasma Science Technology (PLASMA-2017), November 2017*, Gujarat, India.

- **Density measurement techniques for Negative Hydrogen ion source**
  Arun Pandey, D. Mukhopadhyay, M. Bandyopadhyay, H. Tyagi, R. Yadav, A. Chakraborty. 32nd *National Symposium on Plasma Science Technology (PLASMA-2018), December 2018,* Delhi, India.

- **High density hydrogen plasma for negative hydrogen ion production in HELicon Experiment for Negative ion source (HELEN-I).**
  Arun Pandey, D. Mukherjee, M. Bandyopadhyay, A. Chakraborty. *6th PSSI-Plasma Scholars? Colloquium (PSC-2018), Sikkim, India.*

ARUN PANDEY

ACKNOWLEDGEMENTS

I had imagined myself going through the PhD experience numerous times during my masters. I had never anticipated, then, that a PhD degree offers much more than just academic advancement. Throughout this journey, I have had the privilege to work with extremely helpful and knowledgeable people and I want to express my sincere gratitude to all those who have helped me during my PhD journey.

I would be endlessly grateful to my PhD supervisor Dr. Mainak Bandyopadhyay for giving me an opportunity to work with him and for the immense help and persistent support and requisite guidance that he has provided me throughout the PhD. The evening Physics discussions during a paper writing were always inspiring and motivating. I have learned countless things from him apart from the obvious plasma physics and experimental techniques. I would like to thank him for his incessant encouragement and for being patient with me throughout this period. His assiduous carefulness at all times from the initial simulation days in the ITER-India office to writing this thesis has been a great teaching tool.

I am indebted to my co-advisor Dr. Shantanu Karkari for actively supporting me in my research and publications. He made my second publication rich in Physics at the same time made it easily publishable. He has always been a friendly presence in my doctoral committee. I would also like to thank him for taking out time to frame my synopsis and guiding me through academic writing process and also for teaching me the construction of the emissive probe.

I express my sincere thanks to Prof. Subroto Mukherjee, who is the chairman of my doctoral committee, for always showing me the most feasible and practical approach to any problem. I thank him for always setting up deadlines for me to get things done in time and for his Research Methodology classes.

I would also like to thank Prof. Prabal Chattopadhyay, whose ever so inspiring presence in my doctoral committee was necessary for me to strive for a better performance. I thank him for his invaluable critiquing opinions, which helped shaped my thesis into the present form. I also want to thank him for his Experimental Plasma Physics lectures.

I am grateful to Mr. Arun Chakraborty, who has given me the opportunity to

14

Contents

SYNOPSIS

Helicon plasma sources are power efficient plasma devices having the ability to produce high plasmas densities typically in range of $10^{18} - 10^{19} m^{-3}$ at relatively low Radio Frequncy (RF) power as compared to other RF discharges. This property has made them highly attractive for plasma processing applications, helicon thrusters used in space exploration and a variety of ion sources. The basic configuration of a helicon plasma source comprises of a vacuum chamber, a radiating antenna, radio-frequency (RF) generator and external magnetic fields, which are produced by permanent, or electromagnet coils. The magnetic field dramatically changes the electron dynamics inside the discharge. This leads to triggering of different power absorbing modes inside the plasma. Typically, the excitation frequency ω of the helicon wave lies in the range: $\omega_{ci} << \omega_{LH} << \omega << \omega_{ce} << \omega_{pe}$. Here, ω_{LH} is the lower hybrid frequency, ω_{ci} is the ion cyclotron frequency, ω_{ce} is the electron cyclotron frequency and ω_{pe} is the plasma frequency. The conventional helicon plasma sources are generally based on electromagnets, which have flexibility of magnetic field variation, but also have various complexities due to being bulky. Furthermore, due to the high current required for producing magnetic fields, the coils need external cooling. This adds to the interface issues and poses a practical challenge. Therefore, the present thesis is primarily motivated to address these problems by designing a compact helicon source using permanent magnets. The fields generated by the permanent magnet along with external parameters such as RF power and operational frequency are tailored to generate the desired high plasma density, which is a requisite for positive or negative ion sources. This research work focuses on development of a helicon plasma source. The use of helicon plasma source as a negative hydrogen ion source has been demonstrated. One

of the challenges is to effectively couple the RF power from the RF generator to the exciter coils and reduce losses to enhance the plasma density. This requires optimization of the RF antenna design and the plasma source geometry. In addition to this, the optimization of the spatial profile of the magnetic field as well as the field strength are also necessary to enable efficient power coupling to the plasma and reduce losses. The optimization of these parameters have been done based on computer simulations using the codes HELIC and BfieldM. The HELIC code computes the power deposition spectra in the plasma for a given antenna configuration, magnetic field and geometrical parameters with different gases, vessel materials and RF frequencies; whereas, the magnetic field topology produced by permanent ring magnet is calculated by BfieldM code. The experiments are carried out in two stages. In the first stage, the experiments are performed with argon gas. This is essential in order to understand the power coupling to the plasma and benchmarking the helicon wave characteristics considering the relatively more abundant literature available on argon helicon plasmas. The work with hydrogen is carried out in the next stage. The motivation behind this is to demonstrate the utility of the helicon plasma source as an ion source and study the formation of negative hydrogen ions for application in a negative ion source. The experimental setup consists of a source tube made of glass, a permanent ring magnet, and single loop antenna capable of exciting m = 0 helicon mode in the argon plasma. A stainless steel expansion chamber is attached below the glass chamber. Linear cusp magnetic field configuration formed by an array of permanent magnets arranged circumferentially around the expansion chamber is used for plasma confinement. Plasma parameters in argon plasma are measured using two double-probes, an emissive probe and a magnetic probe for the initial source characterization. Oper-

ation of the Langmuir probes is difficult in the RF environment due to the presence of RF noise. To overcome this issue, two double Langmuir probes and a RF compensated Langmuir probe have been fabricated. The circuits for these diagnostics are developed keeping in mind the frequency and magnitude of the interfering RF noise. To study the helicon wave propagation in the plasma, a magnetic probe is used for measuring the electromagnetic signal. However, it might pick up electrostatic noise while inside the plasma. The differential loop design of the probe helps to cancel the electrostatic noise pick up and gives only the electromagnetic signal at the output. It is calibrated by measuring an oscillating axial field created by a solenoid when a 10A, 13.56 MHz signal is passed through the solenoid. The important highlights of the studies carried out in the argon plasma are the transition from a low to high-density mode as RF power is increased beyond 150W and the density peaking at low magnetic field values. These are some of the characteristics of helicon plasma. In addition to this, the radial profile of the wave field B_z is found to match with the theoretically expected profile of the helicon waves confirming the presence of the helicon mode in the plasma. Experimentally measured plasma parameters such as electron temperature and plasma density are compared with theoretical estimations using particle and energy conservation equations. The experimental results are found to be in agreement with the theoretical model. The particle balance model for non-uniform plasma is used to theoretically determine the electron temperature. To estimate the density value theoretically, power deposition profile is calculated from the HELIC code. This result is used in the energy balance model, which incorporates the cross-field diffusion of electrons in order to calculate the transport and subsequent loss of electrons to the walls. After characterization with argon plasma, performance evaluation in hydrogen plasma

is carried out to understand its suitability as a hydrogen ion source, specifically as a negative hydrogen ion (H^-) source. The excitation of helicon wave in hydrogen discharge requires higher electric field strength. The major challenge in exciting the helicon wave in the hydrogen plasma is the low induced field in the plasma by the loop antenna. Therefore, the experiments are carried out using Nagoya-III antenna in place of the loop antenna to ensure better RF electric field coupling. This corresponds to $m = 1$ helicon mode. The variation of ion saturation current with RF power is compared for the two gases, i.e. argon and hydrogen. The transition from inductively coupled plasma mode to helicon mode is observed in hydrogen (argon) plasma at $P_{RF} \sim 800W$ (~ 200 W) marked with a sudden rise in plasma density. In the experiments with hydrogen plasma, an important feature observed is the spatial cooling of electrons when they are moving downstream along the expanding magnetic field. In the expansion chamber, plasma density and temperature gradually decrease. These conditions are conducive to negative hydrogen ion formation. The negative hydrogen ion density is measured by two independent non-invasive techniques. The first H^- ion diagnostic technique, used for H^- ion density measurement is based on Optical Emission Spectroscopy (OES) method by analyzing the Balmer line ratios, H_α/H_β and H_α/H_γ. The negative ion density values, obtained from the OES are experimentally verified by another diagnostic technique, known as Cavity Ring Down Spectroscopic (CRDS) diagnostic. The CRDS is a highly sensitive laser aided diagnostic based on laser absorption technique. The H^- ions with an electron affinity of 0.76 eV can absorb laser photons of 1.2 eV energy (1064 nm) and get neutralized by detaching the loosely bound extra electron by photo-detachment reaction. A photo detector is placed just outside the cavity (near one mirror) to receive the photons transmitted through that mirror.

x

This photo signal decays exponentially in time due to photon absorption inside the cavity in the photo-detachment reaction. Time constant of the time varying photodiode signal is measured to compute the negative hydrogen ion density. In the present experiment, the measurement value of H^- ion is of the order of $10^{16}m^{-3}$ at 6 mTorr pressure, which is similar in order as that obtained from OES. Both OES and CRDS give average H^- ion density over the line of sight plasma volume. The measured H^- density is validated with a particle balance model considering experimental plasma conditions. It is also observed that, in the source region (near the antenna) the density peaks and decreases downstream as axial length increases Interestingly, the density profile shows another density rise away from the antenna in the expansion chamber accompanied with a rise in the electron temperature at that location. To understand this phenomenon wave fields are measured using a B-dot probe and based on these measurements a qualitative description of this phenomenon is presented. Thus, it is seen that the control of wave propagation through magnetic fields in the downstream can be established. The phenomenon is still under investigation due to the fact that expansion chamber will be coupled to the ion source beam extraction system in future. Downstream physics will influence the ion beam characteristics. In summary, a permanent magnet based, compact and energy efficient high-density helicon plasma source is designed and developed based on a conceptual design. A power balance model is developed for argon plasma applicable to helicon plasmas with axial magnetic field and non-uniform power absorption. The permanent ring-magnet setup in helicon plasma provides appropriate field topology that is desirable for the formation of negative ions. This is possible due to the expanding magnetic field line configuration, which cools the electrons as they move downstream. Volume production of H^- ions is

demonstrated without the use of Caesium (Cs). Negative hydrogen ion source without the use of Caesium is important for negative ion source research. Operation without Cs ensures minimum maintenance and operational reliability. It has also been shown that the permanent ring magnet, in addition to providing the axial field, can also be used as a control knob for exploring various propagation regimes of the helicon plasma

The thesis is organized as follows. Chapter-1 gives an introduction to the helicon waves in plasma, helicon sources and their applications. The advantages of helicon plasmas over other RF plasmas are discussed. It also describes the advantages of using permanent magnets in lieu of electromagnets. The basic helicon wave theory and associated physics behind the engineering design of the helicon plasma source is described in chapter-2. This chapter also elaborates on the wave properties, various antenna designs, which correspond to different helicon wave structures. Chapter 3 contains the details of the conceptual design using computer codes. In this chapter, design optimization results are presented. In chapter-4, the detailed description of experimental setup and associated plasma diagnostics are presented. In the chapter-5 detailed analyses of the experiments performed in the argon helicon plasma is given and associated physics observations are discussed. The hydrogen helicon plasma and its associated downstream physics in the expansion chamber, is presented in chapter-6. Chapter-7 discusses solely the negative hydrogen ion (H^- ion) measurement results including a theoretical model based on particle balance using production and destruction reactions and shows the utility of helicon plasmas in negative hydrogen ion sources. The summary of the findings and the proposed future work has been outlined in chapter-8 of the thesis.

List of Figures

xviii

xx

List of Tables

1

Introduction And Motivation

The present thesis work concentrates on design, development and characterization of a permanent magnet based helicon plasma source. The performance of the present helicon plasma source is investigated for two different gases: Argon and Hydrogen. The helicon source development is part of a project with an eventual goal of developing a negative hydrogen ion source. It is an electrode-less plasma source and possesses advantages over filament based and Capacitively coupled plasma (CCP) sources. Helicon plasmas are more efficient than inductively coupled plasmas (ICP), due to their high ionization efficiency at relatively low input power compared to ICP. Helicon plasmas have found applications in a variety of fields like plasma processing, plasma thrusters, ion sources and current drive and heating systems in Nuclear Fusion reactors. The NBI (Neutral Beam Injection) heating system in such reactors uses a negative hydrogen ion source, where the negative hydrogen ions are accelerated and subsequently neutralized to generate a high-energy neutral beam.

1.1 Introduction

Helicon plasma discharges are very efficient due to their high ionization capability [12]. Ever since Boswell demonstrated this phenomenon in RF plasmas with an axial magnetic field configuration [6], helicon plasma sources have been a topic of research for their usefulness in different technological applications. The physical processes leading to such a high efficiency are still not well understood. Typical helicon discharges have plasma densities in the range of $10^{18} - 10^{19} m^{-3}$ [12] and plasma temperature $\sim$ few eV in an Argon plasma with neutral fill pressures in the range of $\sim 10^{-3} - 10^{-2}$ mbar and with $1 - 2$ kW RF power. In hydrogen gas the density is reduced by few factors (3 - 10 times) but its still much higher compared to other high frequency plasma sources. Since, high density plasmas can be produced with helicon sources at relatively low RF power ($\sim$ few kW) and pressure, these plasma sources are being used for plasma processing [13], space exploration [14] and ion sources [15].

Configurationally, helicon plasma sources are cylindrical ICP type sources with an axial magnetic field (10 - 100G) which makes the plasma electron magnetized but keep ions unmagnetized. The axial dc magnetic field restricts the transport of electrons across the field leading to an improved confinement of the energetic electrons which helps in maintaining a higher ionization in the plasma volume. The presence of DC field affects the skin depth calculations in a non-trivial manner. It is justified to consider that the skin depth increases in magnetized plasmas with an axially propagating wave (helicon wave). Large skin depth improves better RF power coupling to the plasma. If the frequency of excitation ω, (by the RF antenna connected to a RF generator), lies in the range $\omega_{ci} << \omega_{LH} << \omega << \omega_{ce} << \omega_{pe}$, where the ion cyclotron frequency is denoted by ω_{ci}, and electron cyclotron frequency by ω_{ce}) helicon waves can propagate in the RF plasma [16]. Helicon waves are bounded whistler waves propagating parallel to the external magnetic field.

2

The boundary effects, among many other things, lead to coupling of the helicon wave with its electrostatic counterpart (Trivelpiece-Gould wave), thus altering its propagation and polarization. The proposed reasons behind characteristic large RF power absorption and high degree of ionization with low RF power in helicon plasmas are collisionless Landau damping [5,17], coupling of helicon wave with the strongly damped surface wave (Trivelpiece-Gould or TG mode) [18] and parametric decay of the helicon wave and subsequent Landau damping.

Another consequence arising from the applied axial magnetic field is that the hot plasma is confined near the axis, whereas outer side of the plasma column is relative cooler and suitable for negative ion formation. This effect can be exploited for the production of negative hydrogen ions in the plasma. A clever arrangement of the axial field would make helicon plasma an ideal candidate for developing a large size negative ion source. Future negative ion based neutral beam injector (NNBI) system for DEMO reactor is being developed based on helicon ion source [19].

In this thesis, development of a compact permanent magnet based helicon plasma device is described which is being studied for negative ion source application. The experimental setup is named HELEN-I (HELicon Experiment for Negative ion source-I). The conventional helicon plasma sources are generally based on electromagnets, which have flexibility of magnetic field variation but also have various interface complexities due to being bulky. The requirement of passing high currents and external cooling also add more interfaces. The present thesis is therefore motivated towards building a compact helicon source using permanent ring magnets to produce required axial magnetic field and further optimizing it to achieve high density at relatively low RF power input. This shall be desirable for positive or negative ion sources and may have applications in other fields as well. Since the induction of permanent ring-magnets against conventional electromagnet design is a new aspect; therefore this needs to be systematically researched and developed.

The device comprises of a permanent NdFeB ring magnet for producing the axial field. The first step toward the development of the helicon source is framing of a conceptual design on the basis of which the plasma source can be realized. This is done using two computer codes HELIC [16] and BfieldM [13]. HELIC is developed by Donald Arnush and Francis F. Chen [16] for helicon plasma sources. It can be used to obtain the power deposition spectra for various operating conditions. The operating parameters here include the RF antenna, gas used, geometry of the source, magnetic field, gas pressure, electron temperature, and plasma density. By varying these conditions in the code systematically and analysing the results, we can come to an optimised conceptual design. The uniformity of the magnetic field lines in such sources can affect the wave propagation and affect the plasma formation. The magnetic field due to permanent ring magnets is calculated by BfieldM code.

Various other research groups have also developed such sources using permanent magnets. Virko et al. [20] had demonstrated the performance of such a source with radially magnetized cylindrical magnet assembly whereas, Torreblanca and Chen [21] used annular permanent magnets for providing a diverging dc field. Takahashi [22] on the other hand used a double concentric array of permanent magnets to provide a constant field area inside the field area and a diverging magnetic field at the outlet of the source. This setup is similar to the field configuration for the HELicon Experiment for Negative ion source-I (HELEN-I) developed at IPR. Another important feature of the HELEN source is the use of a line cusp configuration in the expansion chamber for plasma confinement. This configuration affects the Ion Energy Distribution Function (IEDF) and enhances the charge exchange collisions [23]. This type of confinement can increase the plasma density by two orders of magnitude [24]. Such effects can also be studied in HELEN-I because of the presence of the confining cusp magnetic field in the expansion chamber. Devices like the Mega Ampere Generator for Plasma Implosion Experiments (MAGPIE) [25],

Resonant Antenna Ion Device (RAID) [26] and PM-expanded plasma sources [22] are being developed for hydrogen ion source configurational RD. These ion source devices use helicon wave for plasma production and have different magnetic field configurations.

Since HELEN-I device is being developed for a negative ion source application, a plasma expansion chamber is attached to it. For plasma confinement in the expansion chamber, permanent NdFeB bar magnet based line cusp configuration is used. This type of confinement can increase the plasma density by two orders of magnitude leung but influence the wave propagation downstream, as uniformity of axial field is affected. This line cusp plasma confinement configuration affects the Ion Energy Distribution Function (IEDF) in the plasma and enhances the charge exchange collisions charles. Since plasma confinement magnet configuration influences IEDF and so affects ion source performance, it is important to understand its effect on negative hydrogen ion density in such configuration. In the present experiment, study on negative hydrogen ion density in the expansion volume with cusp magnetic field configuration for plasma confinement has been carried out for different operational pressure, RF power and axial magnetic field. It is to be noted that the magnetic field configuration for a conventional negative hydrogen ion sources is different compared to the configuration used in the present experimental system. The difference is in the sense that conventional negative ion source uses a transverse filter field to divide the plasma chamber virtually into two plasma volumes. Such transverse magnetic field configurations have not been employed in HELEN yet however the negative hydrogen ion yield in the present setup is comparable to that with conventional configuration. Nevertheless, transverse magnetic field configuration would be used later along with different plasma confinement configurations (different line cusp, checkerboard cusp, and ring-cusp).

1.2 Helicon sources in plasma applications

1.2.1 Plasma Processing

In plasma processing the conventional plasma source candidates are capacitively coupled plasmas and inductively coupled plasmas which are usually operated at high neutral pressures to obtain a high density plasma for good etching. The helicon plasmas are extremely useful in such cases due to their ability to generate high ionization at low neutral pressures with comparatively low power consumption. The operation at low pressures creates a relatively stable plasma and reduces the ion energy spread because of very low collision rates. Shima et al. (2001) [27] demonstrated the use of helicon plasmas in plasma processing by preparing antimony films by helicon wave plasma sputtering method. Sadaki et al. [28] used the helicon wave heated nitrogen plasma to develop a compact, permanent magnet based, low pressure ($< 1mTorr$) Nitrogen radical source with high electron and radical densities for the production of various nitride films such as GaN. Commercial helicon plasma reactors capable of etching wafers having 200 cm diameter are used [G. A. Campbell, D. I .C. Pearson and A. P. deChambrier, Proc. 33rd Ann. Techn. Conf., Society of Vacuum Coaters, (1990); B. Chapman, N. Benjamin, C F A van Os, R. W. Boswell and A. J. Perry, Proc. 12th Symp. on Dry Process (Denki-Gakkai, Tokyo, (1991) successfully. A prototype source for 300 mm wafers has been built and shown to give uniform coverage [G. R. Tynan et al., J. Vac. Sci. Technol. A 15, 2885, (1997)]. G. R. Tynan et al., described another such source, $m = 0$ Resonant Inductive ($M\varnothing RI^{TM}$), which uses an azimuthally symmetric helicon plasma [29]. The source is used for deep-submicron etching of poly-silicon, oxide, and metal films. They showed that the wafer etch rate and etching uniformity depends on the divergence of the source magnetic field and can be controlled using the magnetic field configuration. Several other examples can

be found which use the helicon plasmas for investigating the etch selectivity of Silicon and Silicon dioxide using an electronegative gas as demonstrated by Boswell in 1985 and 1987 [30, 31].

1.2.2 Helicon Plasma Thrusters

The plasma based thrusters are much more efficient than the chemical thrusters due to their ability to provide high specific pulse [32]. In this regard, helicon sources are an excellent candidate for plasma thrusters as in the conventional Hall thrusters and Ion engines the electrodes are immersed inside the plasma cavity which results in the subsequent erosion of the electrodes and plasma contamination. The helicon sources, on the other hand, are electrode-less, hence avoiding plasma contamination in addition to providing higher power consumption efficiency. The VASIMR project is a promising example of one such thruster device where a helicon wave heated plasma is created by applying a high RF power (200 kW) and exhausted through a magnetic nozzle [32] designed to generate a thrust of $\sim$ 6N and a specific pulse of 4,900 s. Initial experiments on development of helicon thrusters were single helicon thrusters with no acceleration electrode [33]. Toki et al., showed the possible use of the helicon plasma source for electric propulsion in a small helicon plasma source with an argon plasma density of $8 \times 10^{12} cm^{-3}$ at 100 G field. Winglee [34] et al., showed the affect of magnetic nozzles in increasing the efficiency of helicon plasma thrusters by making the plasma stream highly focused. They demostrated that the specific impulse of the system can be increased by 30% by the addition of the nozzle due to the conversion of thermal energy into directed energy in association with a highly collimated profile. Several other thruster configurations exploit the double layer created in the helicon plasma due to a non-uniformity in the axial magnetic field. In this case there exists a sharp potential drop in the plasma and hence an electric field which is capable of accelerating the ions to tens of eV [35]. When an additional acceleration is used in the thruster configuration

Harada et al., have showed that in the downstream region, the ion beam energy of the order of the applied acceleration voltage is obtained where the ion beam energy profile strongly depends on the helicon power and the applied acceleration voltage. Several other examples include the Gridded Helicon Ion Thruster (GHIT) [36], the Helicon Electrodeless Advanced Thruster (HEAT) [37] and the helicon electrostatic thruster (HEST) [38]. GHIT is operated at at 13.56 MHz, with a magnetic field 50-250 G in the plasma. The ion production cost determined is 132-212 ś 28-46 eV/ion, driven primarily by ion loss to the walls and anode, as well as energy loss in the anode and grid sheaths. In HEST the specific impulse, thrust efficiency, and propellant utilization efficiency were reported to be 2000 s, 9.7%, and 9.8%, respectively.

1.2.3 Negative Hydrogen Ion Sources for Neutral Beams

The neutral Beam Injection mechanism is one of the most efficient ways to heat the magnetically confined tokamak plasmas. NBI system requires a hydrogen ion source to generate a high energy neutral beam to heat the tokamak plasmas to fusion relevant temperatures. The NBI penetration depth in the plasma decreases with increasing plasma density and approximately given by: $\lambda_{NB} \sim (E_{NB}/A_{NB})^{1/2}(na^{-1})$, where E_{NB} is the energy of the neutral beam in eV, A_{NB} is the atomic mass of the beam species, n is the plasma density and a is the minor radius of the tokamak. Therefore, beam energies in the range of MeV are required to penetrate to the core and heat high density tokamak plasmas in an ITER (International Thermonuclear Experimental Reactor) like machine [39].

For such high beam energies, the negative hydrogen ion (H^-) sources have proven to be better than the positive hydrogen ion sources in terms of the neutralization efficiency of the H^- ions figure 1.1. Due to the low binding energy of the electron in the H^- ion, it can be easily detached. This has led to the development of H^- sources as potential ion source options for NBI applications in fusion

devices [40].
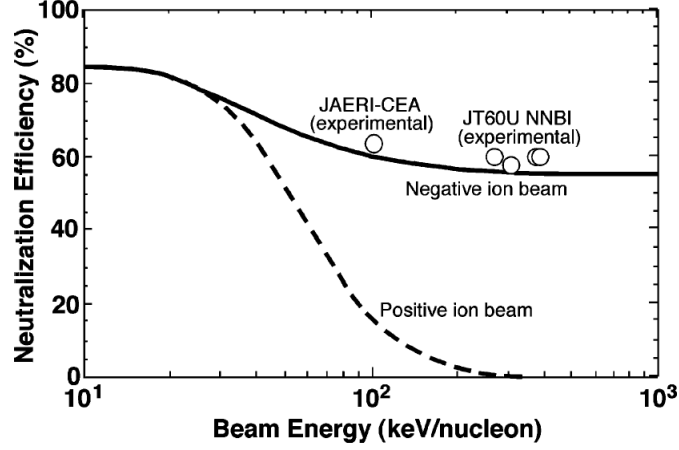
Figure 1.1: Variation of neutralization efficiency of the ions with beam energy. Source: [1]

This requires the production of high density of hydrogen ions, accelerating them to very high energies and their subsequent neutralization to H^0. The neutralization efficiency of positive hydrogen ions practically goes to zero at energies $> 200 keV$. Therefore, negative hydrogen ion sources are preferred for this purpose as their neutralization efficiency is higher ($\sim 60\%$) in the energy range in question. In the ITER-NBI, negative ion sources producing energies as high as 1 MeV and 17 MW power and beam current reaching up to 40 A for one hour have to be developed. Therefore, a great deal of interest is drawn towards the development of high current negative ion sources. A prerequisite for the development of a high current negative ion source is a uniform and high density hydrogen plasma source [41]. The ion source for the NBI system of ITER is going to be an ICP based negative hydrogen ion source using caesium coated surface for the surface production of negative hydrogen ions. Many prototype experiments have been developed to optimise the ELISE (Extraction from a Large Ion Source Experiment) test facility is a half-ITER-size ion source developed by IPP, Germany. It is an intermediate step

between the RF driven ITER prototype source [42] and the ion source for the ITER NBI system [43]. ELISE is developed with the aim of producing a uniform beam with extracted current densities of $28.5 mA/cm^2$ in deuterium and $33 mA/cm^2$ in hydrogen, a low fraction of co-extracted electrons at a filling pressure of 0.3 Pa and one hour long pulse lengths [44]. The ion source has four drivers for creating plasma by using a rf power of $< 90 kW/driver$ which expands into the extraction system [45]. H^- production takes place primarily through the surface process.An ITER-NBI size ion source for testing and optimizing of the ITER Injector prototype MITICA (Megavolt ITer Injector and Concept Advancement) 1MV beam source is under development in Padua, Italy. It aims at achieving the specified negative ion yield and study the beam uniformity and high voltage holding. The investigation of beam particle trajectories is also an aspect of the source development along with optimization of the neutralization process [46].

Santoso et al., (2015) [47] suggested that the utilization of the helicon heated plasmas in negative hydrogen ion sources would be able to "reduce power requirements and potentially obviate the need for caesiation due to the high plasma densities achievable." Helicon sources for negative hydrogen ion source configurational RD has already been proposed in many devices, e.g. MAGPIE [25], RAID [26] and PM-expanded plasma source [22]. All these devices have different magnetic field configurations for plasma creation and the filtering the electron population based on their energy groups (low and high). The mechanical structure (or boundary) as well as virtual boundary like transverse magnetic field on the axis of a helicon source affect the wave propagation and hence the plasma formation efficiency. This particular issue is vividly studied by Takahashi [22]. On the other hand, in PE-GASES [14], configuration grids and axial magnetic field for helicon operation are orthogonal. Figure 1.2 shows a prototype helicon plasma based ion source device developed at the Swiss Plasma Center. It uses a special Birdcage antenna to generate helicon plasma by applying a rf power as high as 10 kW at 13.56 MHz and

0.3 Pa pressure. Electron density of $10^{18}m^{-3}$ can be attained in hydrogen plasma. The electromagnets surrounding the vessel produce an on-axis magnetic field up to 800 G. H^- production is through volume process and H^- densities in the order of 10^{16} are measured CRDS diagnostic [2].
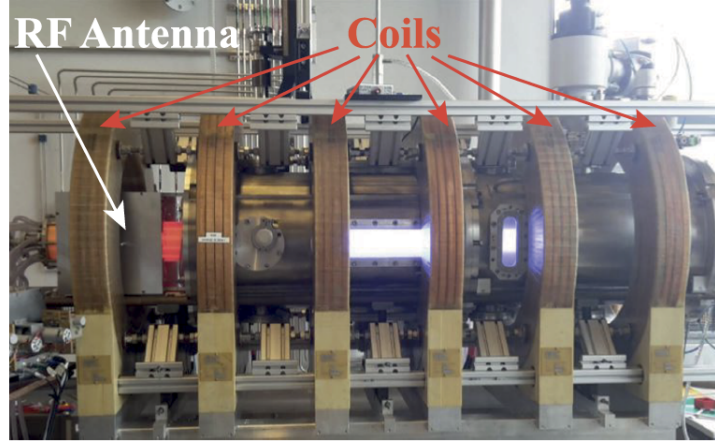
Figure 1.2: A picture of the RAID plasma device. Source: [2]
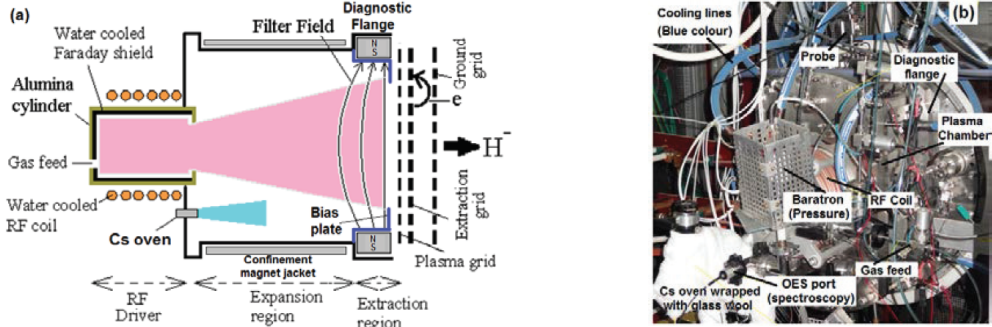
Figure 1.3: (a) Schematic of ROBIN and (b) picture of RF ion source for ROBIN. Source: [3]

The H^- sources are also required for the DNB (Diagnostic Neutral Beam) systems in fusion devices like ITER. The ITER-DNB is going to be a H^- source based 100 keV hydrogen neutral beam. It will be used during D-T phase of ITER for

estimating the helium ash content with CXRS (Charge Exchange Recombination Spectroscopy) [48]. Therefore, an inductively coupled single driver based negative hydrogen ion source facility ROBIN (RF Operated Beam source in India for Negative ion source RD) is developed and is in operation [49] at IPR, India. A schematic of the in source along with the experimental setup is shown in figure 1.3. It can be seen from the schematic in figure 1.3 that the plasma is virtually divided into two parts, i.e. before the filter field with high and low energy electrons and after the filter field with only low energy electrons. The plasma grid is coated with Cs to facilitate the formation of H^- and since there are no fast electrons the destruction of H^- is hindered and H^- is yield is improved because of the filter field. Pandya et al. [3] have demonstrated the performance of ROBIN source, an ICP based H^- source operating at 0.3-0.6 Pa and at 30-70kW of 1 MHz RF power operating in surface conversion mode. In addition to this, to understand the multi-driver source operation of DNB configuration, a two-driver based TWIN source experimental facility is also being developed at IPR [50–52].

1.3 Other popular high frequency and high density plasma sources

Plasma is normally created by transferring energy from energetic electrons or ions or photons to neutral gas molecules/atoms causing the ionization due to collisions. There are various ways to supply the necessary energy to the electrons for plasma generation inside vacuum chamber filled with neutral gases. Based on different mechanisms of transferring energy to the electrons, different plasma sources are developed. In high frequency plasma sources power is transferred from the power supply to the plasma by a suitable antenna or electrode. The power transfer is based on impedance matching between the power supply system and the plasma

by means of an adequate impedance matching circuit. Different plasma sources are suitable for different applications based on their characteristics in terms of plasma parameters space (plasma density, temperature, plasma size, plasma uniformity etc.), operational parameter space (setup dimension, pressure, power, magnetic field etc.), and cost effectiveness (efficiency, reliability, maintenance, environment sensitivity). Therefore, the selection of one particular plasma source over another is influenced by many factors, which include technical as well as non-technical reasons.

1.3.1 Electron cyclotron resonance (ECR) source

In Electron cyclotron resonance (ECR) plasma, the energy is given to the electrons by an electromagnetic (EM) wave resonantly. This means that the frequency of the power source matches with the frequency of the cyclotron motion of the electron in presence of a static magnetic field. An electron in a static and uniform magnetic field will move in a circle or helical path (cyclotron motion) due to the Lorentz force. If the electron cyclotron frequency matches with the EM wave frequency, electron will see the same phase of the electric field of the time dependent EM wave and gets accelerated. It is like a situation where an electron is gaining energy while surfing on the EM wave. However, with increase in energy, the collisions with neutrals and other charged species also increase. These collisions are responsible for de-phasing the electron from the resonance condition and eventually leading to a steady-state condition. The driving frequency for electron cyclotron resonance lies in GHz (microwave) range. The most popular frequency is 2.45GHz, which corresponds to 875G magnetic field for the electron cyclotron motion frequency for the resonance heating. Therefore, a 2.45GHz ECR source is on with a strong magnetic field > 875G [53]. For 2.45GHz EM wave, the critical plasma density is $\sim 7.4 10^{16} m^{-3}$ beyond which the EM wave cannot penetrate inside the plasma and therefore, the power deposition zone is primarily limited to a narrow resonance

area only. However, due to non-linear interaction of EM wave and the plasma few other channels are also present through which over dense plasmas are created in some ECR sources [54]. Usually, the ECR plasma sources are smaller in volume. For bigger size plasma, multi-ECR configuration is utilized [55,56]. Typical plasma density that can be achieved in an overdense plasma is $\sim 10^{17} m^{-3}$ with few kW of microwave power. Plasma temperature in ECR sources is normally high ($> 5eV$) with a very large fraction of hot electron population [57], which is not favourable for a negative ion source but suitable for positive ion sources with multiple charged states [58].

1.3.2 Surface wave discharge plasma source

Surface-wave discharge (SWD) can be sustained far away from the active zone where surface wave launcher antenna is placed and so plasma columns as long as ~ 6m can be created. The surface wave launchers have the widest band of applied field frequency from the microwave (GHz) to the RF (MHz) range [59] - from less than one MHz up to 10GHz. However the gas pressure ranges are relatively higher from sub-mbar to atmospheric pressure and corresponding density varies within the range from $10^8 cm^{-3}$ to $10^{15} cm^{-3}$. Compared to other RF and Microwave plasma sources, SWDs are the most flexible ones not only in terms of operating parameters zone but also the plasma shape [60]. The electric field supporting the discharge is from an electromagnetic surface wave that carries away the power from the launcher antenna and solely guided by the bounded plasma column within the dielectric discharge tube [61–64]. Surface wave can only propagate along the discharge column if the electron density exceeds a critical value $n_c = 1.2 \times 10^{-8} (1 + \epsilon) f^2$, where f is the launch frequency in Hz and ϵ is the discharge tube relative permittivity. Though SWD can create long plasma column, but there is a plasma density gradient (dn/dz) that exists along the plasma length from the antenna location which is proportional to the pressure inside the tube and applied frequency

and inversely proportional to the radius of the tube [65]. SWDs are normally having narrow diameter ($\sim$ few cm) with extended length ($\sim$ 100 cm) and have applications in broadcasting in the form of plasma antenna. Application for large area plasma source suitable for large area ion source for beam application is not yet reported. Reviews on SWDs and its properties and can be found [66–70].

1.3.3 Capacitively coupled plasma (CCP) source

Capacitively coupled plasmas (CCP) are the earliest and most popular radio-frequency (RF) plasma reactors in industrial applications due to their easy operating procedure for moderate plasma density requirements. In a CCP device, the plasma is sustained by applying a sinusoidal electrostatic potential across a gap between two electrodes, kept inside a chamber filled with gas at low pressure. As this configuration is similar to a capacitor in an electric circuit, the plasma formed in this electrode configuration is called capacitively coupled plasma (CCP). Considering electron as a single charged particle placed in a sinusoidally varying electric field, the velocity and hence energy of electrons increase and decrease through the cycle. But averaged over a single cycle, the net energy does not change. The electrons gain energy from the input RF power either by collisional or by collision-less processes. However, if the velocity of the electron is such that the time required to reach from the negative electrode to positive electrode is exactly same or less than the sinusoidal polarity change time period, the electron starts gaining energy. This is due to the fact that when the electron is about to hit the positive terminal electrode, the polarity change occurs and the same electrons start repelling the approaching electrons and push them back in the opposite direction which helps the electrons to gain energy for next half cycle while moving towards the other electrode. In this way, energy of the electron increases cycle after cycle. The mechanism of power deposition into a CCP reactor is highly nonlinear and the system needs sufficient RF cycles in order to reach a periodic steady-state solution.

The sinusoidal polarity change frequency lies in $\sim$ 100 kHz - 100 MHz range (Radio Frequency range). While traversing between two electrodes, the energetic electrons collide with the background gas and create plasma. If the electrons are faster in timescale with respect to the RF frequency (electrode polarity change timescale), electrons start hitting the positive electrode before getting repelled due to polarity reversal and so no more energy gaining is possible and rise in plasma density saturates. At higher plasma density, electron plasma frequency becomes much higher than that of applied RF frequency, so the applied voltage is essentially limited within the electrode sheath only which also restricts the electrons to gain further energy during travel between two electrodes. Due to sheath potential, positive ions gain energy in the sheath and sputter the electrode material. This phenomenon is utilized for etching or coating through sputtering. However, it also possesses threat to contaminate the plasma, etching anisotropy due to directed motion of the ions in the sheath. To reduce this anisotropy CCPs are normally operated in higher pressure utilizing neutral collisions to randomize the ion motion within the sheath. Plasma density in CCP is increased by increasing the peak-to-peak voltage of the RF field, which increases the plasma potential and plasma temperature. These are not favorable for negative ion source plasma. Typical plasma density in CCP lies in the range $10^{15}m^{-3} - 10^{11}m^{-3}$ having plasma potential $\sim$ 100V and characterized with low ion-to neutral ratio $\sim 10^{-4}$ to 10^{-2}.

1.3.4 Inductively coupled plasma (ICP) source

Inductively coupled plasmas (ICP) are having plasma density in the range of $10^{16}m^{-3} - 10^{12}m^{-3}$ with plasma potential $\sim$10 V for 1 - 10 kW RF power and having pressure in the order of $\sim 10^{-3} - 10^{-2}$ mbar. Contrast to electrode placed inside the plasma in CCP, in ICP inductive antenna coil can be kept away from the plasma or outside the dielectric vacuum encapsulation chamber due to inductive power coupling mechanism. Therefore, the contamination from antenna coil

electrode can be completely avoided in such configurations. However, sputtering from dielectric vacuum barrier is still present which normally is avoided by placing a Faraday shield (FS) made of non-magnetic substance between the plasma and the dielectric wall. The antenna coil is placed on the other side of the dielectric wall. To avoid eddy current losses in metallic FS, it is designed with slots on the metal body to reduce conducting path for the eddy currents. Some details of ICP sources can be found in the review of ICP sources by J. Hopwood [71]. FS also reduces capacitive coupling between the coil (as one electrode) and plasma (as another electrode) and help to reduce the plasma potential.

An inductively coupled plasma (ICP) is also known as transformer coupled plasma (TCP) because energy is supplied to the plasma (as secondary coil of a transformer) inductively by a time varying electric currents passing through antenna coil (working as primary of the transformer). There are different types of ICP geometries available based on requirements. Out of them planar coil, cylindrical coil geometries are the most popular ones. ICP has flexibility to build large area plasma sources and does not required additional external magnetic field for plasma production which helps to maintain plasma uniformity over large area. ITER ion source are designed based on ICP configuration [39].

1.4 Motivation behind HELEN research

As discussed previously, In ICP based ion sources, RF power is coupled to the plasma through inductive manner and therefore the antenna can be kept outside the plasma and ICP can be considered as electrode-less. Since antenna is not in direct contact with plasma, there is no erosion and less maintenance is required, which ensures higher machine availability. As a consequence, ITER NBI ion sources are all ICP type [72], and future generation NBI sources will also be electrode-less. In an ITER type fusion grade ion source, ~ 1MW of RF power is used for plasma

production out of which ~ 880kW power is removed by the water-cooling circuit in the ion source plasma box (without considering accelerator cooling) [73]. The reason behind high cooling requirements in RF circuit is due to relatively inefficient power coupling by ICP configuration. High power RF generators of total power ~ 1MW are used to create plasma inside the ion source which needs large space in high voltage deck and also correspondingly large cooling system. These are expensive in terms of real equipment cost, running cost as well as the required space. If an alternate efficient electrode less plasma mechanism with minimum interface issues can be identified, it will be beneficial to reduce the overall NBI cost. More importantly, fusion reactors like ITER are going to have a hostile neutron radiation environment and it is imperative to think of means by which the maintenance of the auxiliary systems could be reduced and interfaces could be minimized. Due to having high ionization efficiency, Helicon source with multi-driver configuration [74] would be a promising candidate for a large size ion source. Normal helicon sources are based on large electromagnets, which need large current power supplies and cooling arrangement; i.e. two major interfaces with auxiliary systems. However, permanent magnet based helicon source is free from these interfaces. The use of permanent magnets makes the operation of the plasma source much more convenient and requires much less maintenance.

The negative hydrogen ion sources can operate in two modes depending on the production mechanism of H^- ions in the plasma, a) surface mode and b) volume mode of H^- production. In the surface mode of H^- production a low work function material like caesium (Cs), is used to provide low energy electrons to create H^- ions. A good H^- yield can be achieved by Cs injection into the plasma. But, the handling and maintenance of Cs make it cumbersome to use. Cs deposition on surfaces is poses another problem in the ion source operation. For instance, Cs is deposited on the plasma grid during extraction to obtain a low work function surface to facilitate a high yield of negative ion production. But

18

the plasma redistributes the Cs in the volume, which eventually leads to temporal instabilities of the extracted negative ion current [45].

In the volume process, the electron energy distribution function and the temperature profile in the plasma device are very important parameters. There are two reactions involved in the volume process namely, the vibrational excitation of hydrogen molecule by fast electrons and their conversion to H^- ions by slow electrons. Therefore, it is important two have a temperature gradient in the plasma, which virtually separates the plasma into two parts. This separation can be achieved by applying transverse filter fields, which doubles as a electron discriminator and reduces the co-extracted electron current during beam extraction. But the filter field would also produce plasma drifts and eventually lead to non-uniformities in the ion source and result in deflection of the ion beam trajectories [11].

Another important parameter in optimising the H^- yield is the neutral pressure. At high pressures, the H^- might go down due to increased stripping losses, which result from the collision of H^- with the neutrals. Low pressures are also desirable because of the desired uniformity of the discharge. But, low pressure discharges usually have higher electron temperatures and lower electron densities. The problems encountered for the development of an effective H^- ion source are addressed in this thesis and a possible solution is proposed in the form of a compact, permanent magnet based helicon plasma discharge with expanding plasma. Along with these issues, several other limitations of the currently used Cs fed, ICP based negative ion sources with filter fields are discussed in section 1.2.3. All of these limitations are individually addressed and the possible solutions are practically demonstrated in this thesis work.

In the NBI systems developed so far, the cylindrical insulator walls are protected from the power load and sputtering via co-axial cylindrical metallic Faraday shields. Faraday shield (FS) is designed and fabricated in such a way that the RF field induced eddy current loss in the metallic part of the FS is minimum, so that

RF field can penetrate up to the skin depth and plasma can be generated inductively based on transformer action. However, in presence of strong axial DC magnetic field, charge separation due to different mobility of the charged species of the plasma can takes place inside the ICP region which lead to an radial oscillating electric field. The induced oscillating magnetic field by the RF and produced electric field together forms the required EM waves inside the plasma and effectively RF power is coupled to plasma through this produced EM wave.

Institute for Plasma Research (IPR) has long term research and development (RD) programs on fusion related technologies, Neutral Beam Injector (NBI) system is one of them. Large area, high plasma density sources are needed in NBI ion sources [75]. Present day technology relies either on filament based [11] or on inductively coupled plasma (ICP) based ion sources [76], however efficiency of such technologies is low. Due to high ionization efficiency Helicon source configuration would be a promising candidate to explore further in this regard. This thesis explores the developmental and possible exploitation aspect of the helicon plasma source as a negative ion source.

A flow chart showing the PhD thesis work is given in the figure 1.4.

The thesis is organized as follows. The **chapter 1** is an introduction of helicon wave interaction with plasma and its application for development of different plasma sources. Different applications including for ion sources, which form the motivation behind using helicon plasma source as an H^- ion source. This chapter also describes the advantages of Helicon wave heated plasmas over other RF plasmas. It also describes the advantages of using permanent magnets in lieu of electromagnets for the required axial magnetic field for helicon wave heated plasma source. The basic Helicon wave theory and associated physics behind the engineering design of the Helicon plasma source is described in **chapter 2**. This chapter also elaborates on wave properties, various antenna design which corresponds to different helicon wave structures. **chapter 3** contains the details of the concep-
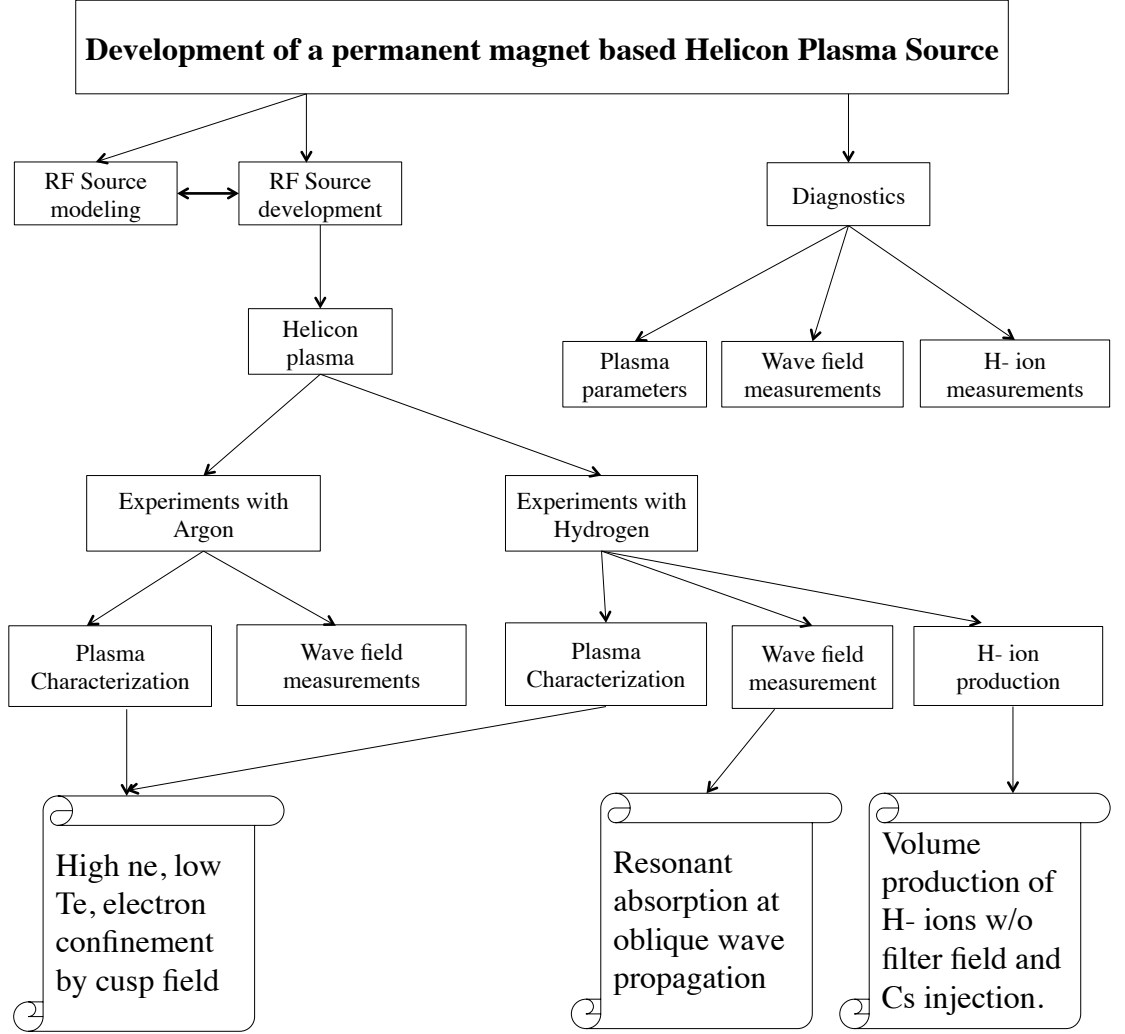
Figure 1.4: Schematic of the PhD thesis work.

tual design using computer codes. In this chapter, design optimization results are presented. Dimensions optimized in the design process are used for fabricating the helicon plasma source. In **chapter 4**, the detailed description of experimental setup and associated plasma diagnostics, those have been used to characterize the plasma (Argon and Hydrogen) and carry out wave measurements. In the **chapter 5** detailed analysis of the experiments performed in the Argon helicon plasma is

given and associated physics observations are discussed. The hydrogen helicon plasma and its associated downstream physics in the expansion chamber, is presented in **chapter 6**. **chapter 7** discusses solely on the negative hydrogen ion (H^- ion) measurement results including a theoretical model based on particle balance using production and destruction reactions and shows the utility of helicon plasmas in the negative hydrogen ion sources. The summary of the thesis finding and the proposed future work have been outlined in **chapter 8** of the thesis.

2

Helicon Source Physics

This chapter describes briefly the basic physics of helicon waves starting from the history of helicon wave plasma in laboratories along with the recently explored applications. As a prelude to the experiments carried out in the Argon and Hydrogen plasmas, this chapter discusses the typical experimental observations in helicon plasmas and their physical mechanisms understood so far.

2.1 History

Whistler waves are low frequency electromagnetic waves with right circular polarization which propagate parallel to the magnetic field in free space. Helicon waves are basically bounded whistler waves [6], which are shown to exhibit both right as well as left circular polarization. The study of whistler waves in space started in the year 1919 when Barkhausen published his work on the observation of ionospheric whistlers [77, 78] . Ever since, numerous theoretical research have been published describing the nature of whistlers and helicon waves in plasmas ([79], [80], [81], [82], [5], [83], [16]). Although it was not until 1970, that their extraordinarily efficient plasma producing quality was discovered by Boswell [12].

Boswell [6], Chen [21], Harada [84] and Briefi and Fantz [15] further demonstrated their use in various practical applications like material processing, plasma lenses, ion sources for Nuclear Fusion, plasma thrusters and as gas laser media. Helicon waves are radially confined whistler waves in magnetized plasmas and propagate with a circular or elliptical polarization if following criterion is met:

$$\omega_{ci} << \omega_{LH} < \omega << \omega_{ce} << \omega_{pe} \qquad (2.1)$$

where, Ω_{ci} and ω_{ce} are the ion cyclotron and electron cyclotron frequencies respectively, ω_{LH} (lower hybrid frequency) $= \omega_{pi} \left[1 + (\omega_{pe}/\omega_e)^2\right]^{-1/2} \sim (\omega_{ci}\omega_{ce})^{1/2}$ and ω_{pe} is the frequency of the electron plasma oscillations. The criterion in equation 2.1 gives an important information about the motion of electrons. The frequency of the helicons is small compared to the electron cyclotron frequency and thus, only the guiding centre motions of electrons are important and not their gyration motion. Whereas, the bounded nature of helicons puts another interesting constraint that the modes excited in the plasma are not purely electromagnetic. The earlier treatment of helicon waves had considered the electron mass to be negligible as compared to the ion mass and formulated the dispersion relation. This treatment could not account for the Trivelpiece Gould (TG) mode propagating at the plasma boundary, which was later on included by Shamrai [18] as a consequence of the finite electron mass correction. Although it is intuitive to assume the TE (Transverse Electric) nature of the helicon modes in plasma but there exists a finite E_z, which is shown to arise from the electron inertia [18], [83]. Theoretically, the helicon wave is treated as a right handed, circularly polarized, electromagnetic wave propagating parallel to the magnetic field. Experimental observations, on the other hand, indicate that helicon waves can be elliptically polarized, in either a left or right handed manner and propagate obliquely to the magnetic field with a finite perpendicular wave vector, which contributes to the wave amplitude. There

is also an associated electrostatic mode propagating near the boundary. Thus, it is necessary to study helicon waves in a more generalized manner as obliquely propagating waves, of which parallel propagation is a special case.

2.2   Cold plasma waves with oblique propagation

The dispersion relation for the cold plasma waves was obtained by E. Åström [85], Sitenko and Stepanov [86] and W. P. Allis [87] separately. The description of the dispersion relation and the wave normal surfaces thus obtained from the dispersion relations is compiled in detail by Stix [88]. The final expression derived in Stix for describing the natural modes of oscillation of a cold plasma is given by,

$$
\begin{pmatrix}
S - n^2 cos^2\theta & -iD & n^2 cos\theta sin\theta \\
iD & S - n^2 & 0 \\
n^2 cos\theta sin\theta & 0 & P - n^2 sin^2\theta
\end{pmatrix}
\begin{pmatrix}
E_x \\
E_y \\
E_z
\end{pmatrix} = 0. \tag{2.2}
$$

where, θ is the angle between the external magnetic field propagation vector, β of the wave. If s denotes the species present in the plasma, ω_s, ω_{ps} are the cyclotron frequency and plasma oscillation frequency of the species s, then

$$
S = \frac{1}{2}(R + L), \qquad D = \frac{1}{2}(R - L) \tag{2.3}
$$

$$
R = 1 - \sum_s \frac{\omega_{ps}^2}{\omega(\omega + \omega_s)} \tag{2.4}
$$

$$
L = 1 - \sum_s \frac{\omega_{ps}^2}{\omega(\omega - \omega_s)} \tag{2.5}
$$

$$
L = 1 - \sum_s \frac{\omega_{ps}^2}{\omega^2} \tag{2.6}
$$

Astrom and Allis [87] rearranged the dispersion relation 2.2 into a more convenient

form:

$$\tan^2\theta = \frac{-P(n^2 - R)(n^2 - L)}{(Sn^2 - RL)(n^2 - P)} \tag{2.7}$$

where, n is the refractive index of the medium for a wave of the type $E = E_0 e^{(ikz - \omega t)}$. We can obtain different solutions of equation 2.7 by varying the value of θ.

taking $\theta = 0$:

$$P = 0 \quad or \quad n^2 = R \quad or \quad n^2 = L; \tag{2.8}$$

taking $\theta = \pi/2$:

$$n^2 = RL/S \quad or \quad n^2 = P. \tag{2.9}$$

Electron waves propagating at arbitrary angles

Here, we have narrowed down our focus toward the electron waves with frequency ω which follow the criterion given in equation 2.1. The dispersion relation obtained earlier can be expressed as the Appleton-Hartree equation for such a wave as:

$$n^2 = 1 - \frac{\omega_{pe}^2}{\omega(\omega_{ce}\cos\theta - \omega)} \tag{2.10}$$

putting $n = \mathbf{k}c/\omega$) and rearranging we get,

$$\frac{k^2 c^2}{\omega^2} = \frac{\omega_{pe}^2}{\omega(\omega_{ce}\cos\theta - \omega)} \tag{2.11}$$

where, $k = (k_\perp^2 + k_\parallel^2)^{1/2} = \beta = $ total wave number.

We can include the electron collisions in equation 2.15 and obtain an expression for ω:

$$\omega = \omega_{ce}\cos\theta \frac{k^2 c^2}{\omega_{pe}^2 + k^2 c^2}\left(1 - i\frac{\nu}{\omega_{ce}\cos\theta}\right) \tag{2.12}$$

where the last term on the right is the dissipation term containing the electron collision frequency, ν. The relation 2.12 can be analyzed in two limits,

Long wavelength limit

The long waves, for which $kc << \omega_{pe}$ are the helicon waves with their dispersion relation given by

$$\omega = \omega_{ce}\frac{k_{\parallel}kc^2}{\omega_{pe}^2} - i\nu\frac{k^2c^2}{\omega_{pe}^2} \tag{2.13}$$

Short wavelength limit

For these waves $kc >> \omega_{pe}$ and they are the strongly damped electrostatic Trivelpiece Gould modes.

$$\omega = \omega_{ce}\frac{k_{\parallel}}{k} - i\nu \tag{2.14}$$

These two branches of the same dispersion relation 2.12 merge when the wavelength is comparative to the anomalous skin depth [18].

2.3   Resonance Cones in Helicon Plasmas

To analyze the dispersion relation Degeling et al. [89] in 2004 showed that for ω lying in the range $\omega_{LH} << \omega << \omega_{ce}$ in a magnetoplasma, the refractive index is anisotropic and shows resonances at certain angles caused by electron inertia. For a radiating antenna in a plasma, the short wavelengths near this resonance angle may contribute to the radiation pattern of the antenna. Let us, for simplicity, take the case of a collisionless plasma. In a collisionless plasma the dispersion relation is given by 2.15.

$$\frac{k^2c^2}{\omega^2} = \frac{\omega_{pe}^2}{\omega(\omega_{ce}cos\theta - \omega)} \tag{2.15}$$

At resonance k→ ∞, which would mean the denominator in equation 2.15 should vanish at resonance. This implies that at resonance:

$$cos\theta = \omega/\omega_{ce} = cos\theta_{RC} \qquad (2.16)$$

where θ is the angle between the external magnetic field and the phase velocity of the wave such that, $k_\parallel = kcos\theta$ and $k_\perp = ksin\theta$ and θ_{RC} is called the phase velocity resonance cone angle. For $\theta > \theta_{RC}$ field oscillations are evanescent as the the refractive index becomes imaginary. Fisher and Gould [90] showed that for $\omega_{LH} << \omega$ the group velocity resonance cone angle is given by

$$sin^2\phi_{RC} = sin^2\left(\frac{\pi}{2} - \theta_{RC}\right). \qquad (2.17)$$

and

$$tan\theta = \frac{-tan\phi}{1 - \frac{\omega_{ce}^2}{\omega^2}} \qquad (2.18)$$

The wave propagation along the resonance cone leads to resonant absorption of energy by the plasma. Recently, Nazarov et al. [91] have shown such an effect experimentally in magnetized plasmas and Prabal et al. [92] in helicon plasmas. This might happen in the region of low magnetic field in a helicon plasma setup because of lower dc magnetic field in that region, which may satisfy the criterion given by equation 2.16.

2.4   Helicon wave field structures

Cold plasma theory is applicable when the thermal velocity of the particles is smaller than the wave phase velocity. Furthermore, in helicon plasmas electron temperature ($\sim$ 5 eV), as we shall see in the upcoming chapters, is much smaller than the antenna wave potentials ($>$ 100 V) making the pressure term negligible

as compared to the electric force. Following this approach, we can use the cold plasma fluid equations for deriving an expression for the dispersion relation for the helicon waves. Consider the following Maxwell's equations,

$$\nabla \cdot \mathbf{B} = 0, \tag{2.19a}$$

$$\nabla \times \mathbf{E} = i\omega \mathbf{B} \tag{2.19b}$$

$$\nabla \times \mathbf{B} = \mu_0(\mathbf{j}) \tag{2.19c}$$

and

$$-i\omega m_e \mathbf{v} = -e(\mathbf{E} + \mathbf{v} \times \mathbf{B_0}) - m_e \nu \mathbf{v} \tag{2.20}$$

is the electron momentum equation. Displacement current is neglected in equation 2.19c on account of the wave frequency ω being small. The pressure term is neglected in the fluid equation 2.20 using the cold plasma assumption. We neglect ion motion since we are focusing in the frequency range above LH (Lower Hybrid) frequency. The plasma current $\mathbf{j}$ consists of only electron current:

$$\mathbf{j} = -en_0 v \tag{2.21}$$

Using this in equation 2.20,

$$\mathbf{E} = -\frac{B_0}{en_0} \left(i\frac{(\omega + i\nu)}{\omega_{ce}} \mathbf{j} + \hat{\mathbf{z}} \times \mathbf{j} \right) \tag{2.22}$$

Substituting equations 2.36 and 2.22 in equation 2.19b we get,

$$i\omega \mathbf{B} = -\frac{B_0}{en_0\mu_0} \left(i\frac{(\omega + i\nu)}{\omega_{ce}} \nabla \times \nabla \times \mathbf{B} + \nabla \times [\hat{\mathbf{z}} \times (\nabla \times \mathbf{B})] \right) \tag{2.23}$$

Equation 2.23 can be simplified to

$$i\omega \mathbf{B} = -\frac{B_0}{en_0\mu_0}\left(i\frac{(\omega + i\nu)}{\omega_{ce}}\nabla \times \nabla \times \mathbf{B} + ik_\parallel \nabla \times \mathbf{B}\right) \quad (2.24)$$

where $k_\parallel$ is the longitudinal wave number this can be reduces to a second order Bessel differential equation,

$$(\beta - \nabla\times)(\beta' - \nabla\times)\mathbf{B} = 0 \quad (2.25)$$

where, β and β' are the roots of the quadratic equation:

$$\delta\beta^2 - k_\parallel\beta + k_w^2 = 0. \quad (2.26)$$

here, $k_w = (\omega n_0\mu_0 e/B_0)^{1/2}$ is the wave number for the whistler wave in free space, and $\delta = (\omega + i\nu)/\omega_{ce}$. The two roots , β and β can be easily calculated and are given by

$$\beta = \frac{k_\parallel}{2\delta}\left(1 - \left[1 - \frac{4\delta k_w^2}{k_\parallel^2}\right]^{1/2}\right) \quad (2.27)$$

$$\beta' = \frac{k_\parallel}{2\delta}\left(1 + \left[1 - \frac{4\delta k_w^2}{k_\parallel^2}\right]^{1/2}\right) \quad (2.28)$$

Equation 2.27 represents the helicon waves and equation 2.28 represents the electrostatic TG modes mentioned earlier. In the limit $\omega k_w^2 << \omega_{ce}k_\parallel^2$, i.e. when the wavelength of the bounded helicon wave is smaller than the whistler in free space, we can write

$$\beta = \frac{k_w^2}{k_\parallel} = \frac{\omega}{k_\parallel}\frac{n_0 e\mu_0}{B_0} \quad (2.29a)$$

$$\beta' = \frac{k_\parallel}{\delta} \quad (2.29b)$$

once we know the value of β and β' we can use these values in the solution of

equation 2.25, $\mathbf{B} = \mathbf{B_1} + \mathbf{B_2}$. B_1 and B_2 correspond to the fields of the two distinct modes. For calculating the fields of the helicon wave we focus on the first root in equation 2.27 and write the corresponding wave equation,

$$\nabla \times \mathbf{B} = \beta \mathbf{B}, \tag{2.30}$$

Taking curl of equation 2.30 we get

$$\nabla^2 \mathbf{B} + \beta^2 \mathbf{B} = 0, \tag{2.31}$$

where β is the total wave number of either roots. For obtaining the helicon wave fields we take the z-component of equation 2.31, which is written as

$$\frac{\partial^2 B_z}{\partial r^2} + \frac{1}{r}\frac{\partial B_z}{r} + \left(k_\perp^2 - \frac{m^2}{r^2}\right) B_z = 0 \tag{2.32}$$

where $k_\perp$ is the transverse wave number such that, $\beta^2 = k_\parallel^2 + k_\perp^2$. The solution of the Bessel equation 2.32 is obtained by using the finite conducting boundary conditions as

$$B_z(r) = A J_m k_\perp (k_\perp r) \tag{2.33}$$

where A is a constant. The transverse components of the wave field are calculated from equation 2.30 as

$$B_r(r) = i\frac{A}{k_\perp^2}\left((\beta + k_\parallel)J_{m-1}(k_\perp r) + (\beta - k_\parallel)J_{m+1}(k_\perp r)\right) \tag{2.34}$$

$$B_\theta(r) = i\frac{A}{k_\perp^2}\left((\beta + k_\parallel)J_{m-1}(k_\perp r) - (\beta - k_\parallel)J_{m+1}(k_\perp r)\right) \tag{2.35}$$

From equation 2.19c and equation 2.30 we can write:

$$\mathbf{j} = \beta \mathbf{B}/\mu_0 \tag{2.36}$$

which when substituted in equation 2.22 gives

$$E_z = -\frac{i\omega m_e \beta}{n_0 e^2 \mu_0} B_z \tag{2.37}$$

and from equation 2.19b we have

$$E_r = \frac{1}{k_{\parallel}} \left(\omega B_\theta - i\frac{\partial E_z}{\partial r} \right) \tag{2.38}$$

$$E_\theta = \frac{1}{k_{\parallel}} \left(\frac{m}{r} E_z - \omega B_r \right) \tag{2.39}$$

For an insulating boundary $j_r(r = a) = 0$; where a is the plasma radius. By putting this condition in equation 2.36 it is seen that B_r must also vanish at the boundary so would E_θ. For a conducting boundary, the tangential component of the electric field must vanish at the boundary, which means $E_\theta(r = a) = 0$. This would again put the same constraint on B_θ that it should vanish at the boundary. Therefore, B_r and E_θ both would go to zero at the boundary irrespective of the type of boundary. This fact is used in calculating the $k_{\perp}$ of the wave. This can be seen by putting $B_r(r = a) = 0$ in equation 2.34 and rearranging to obtain

- for m = 0

$$J_1(k_{\perp} a) = 0 \tag{2.40}$$

- for m = 1

$$J_1(k_{\perp} a) = \frac{k_{\parallel} k_{\perp} a}{2\beta_1} \left[J_2(k_{\perp} a) J_0(k_{\perp} a) \right] \approx 0 \tag{2.41}$$

for both of these conditions $k_{\perp} = 3.83/a$.

Typical experimentally obtained wave field profiles in a helicon plasma are shown in figure 2.1. Figure shows the radial profiles of B_r, B_θ and B_z components

of the wave field for a $m = \pm 1$ helicon mode. These field components obtained experimentally follow the relations 2.33, 2.34 and 2.35 for $m = 1$ case, implying a stronger $m = 1$ mode existing in the plasma. Through the wave field profiles we can directly infer the presence of helicon waves in the plasma as well as the excited azimuthal mode of the wave.
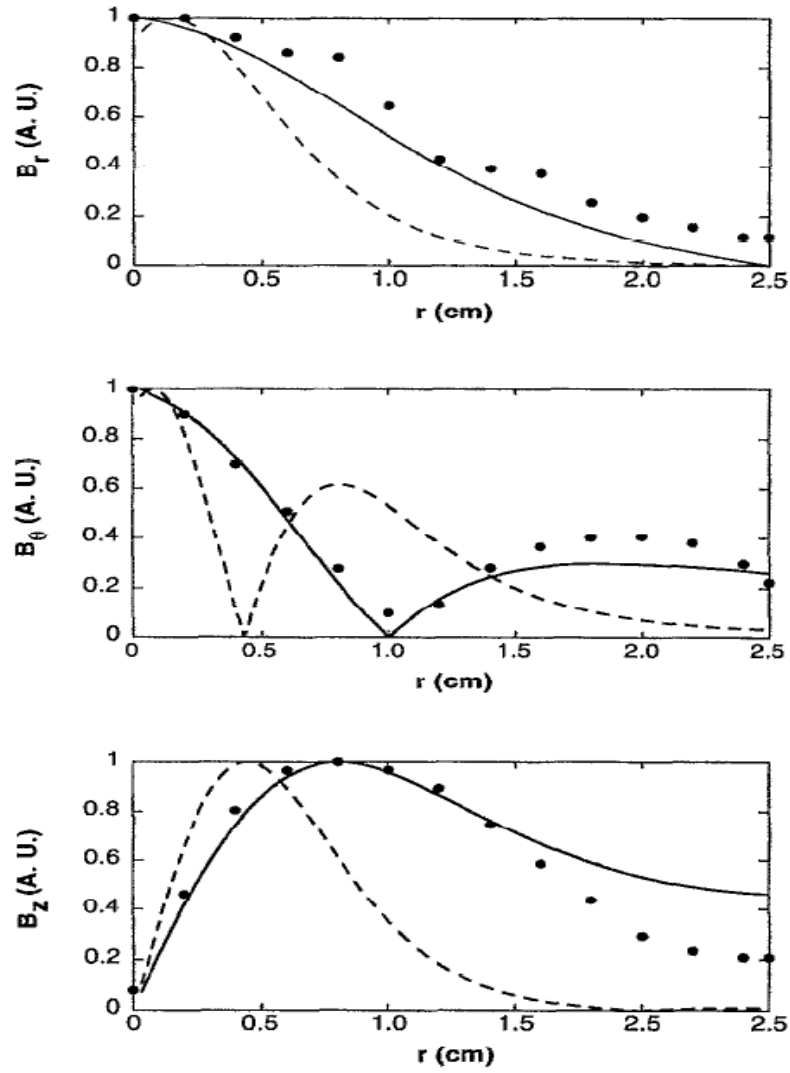
Figure 2.1: Normalized radial profiles of the helicon wave fields. Points: experimental, solid lines: m = + 1 theory; dashed lines: m = - 1 theory. Source: [4].

2.5 Helicon Wavefronts

The equations 2.33 to 2.35 and from 2.37 to 2.39 give the wave profiles in r and θ of the magnetic and electric fields of the wave without taking into account the temporal variation or the axial propagation. To understand the helicon wavefronts we include the propagation in these equations and re-write them:

$$B_z(r) = AJ_m k_\perp(k_\perp r) sin(kz - \omega t) \tag{2.42a}$$

$$B_r(r) = i\frac{A}{k_\perp^2}\left((\beta + k_\parallel)J_{m-1}(k_\perp r) + (\beta - k_\parallel)J_{m+1}(k_\perp r)\right)cos(kz - \omega t) \tag{2.42b}$$

$$B_\theta(r) = i\frac{A}{k_\perp^2}\left((\beta + k_\parallel)J_{m-1}(k_\perp r) - (\beta - k_\parallel)J_{m+1}(k_\perp r)\right)sin(kz - \omega t) \tag{2.42c}$$

$$E_z = -(\frac{i\omega m_e \beta}{n_0 e^2 \mu_0}B_z)sin(kz - \omega t) \tag{2.43a}$$

$$E_r = \frac{1}{k_\parallel}\left(\omega B_\theta - i\frac{\partial E_z}{\partial r}\right)sin(kz - \omega t) \tag{2.43b}$$

$$E_\theta = \frac{1}{k_\parallel}\left(\frac{m}{r}E_z - \omega B_r\right)cos(kz - \omega t) \tag{2.43c}$$

let $\xi = kz - \omega t$, then we can draw the wavefronts by assuming different values of ξ. We describe the two cases relevant to this thesis work, representing the two azimuthal modes, below:

- **m = 0 mode**

   By putting $m = 0$ in the equations above we see that when $\xi = 0$, the radial field, E_r becomes zero, whereas the $cos\xi$ in the azimuthal component attains its maximum value. Therefore, the electric field is purely azimuthal. As ξ increases the radial component of the field starts coming into play and the bet result is a spiral field line wavefront. At $\xi = \pi/2$ the azimuthal component vanishes and the field is purely radial. This is the half cycle of the wave and

Electric field line patterns for the m = 0 mode.

Electric field line patterns for the m = 1 mode.
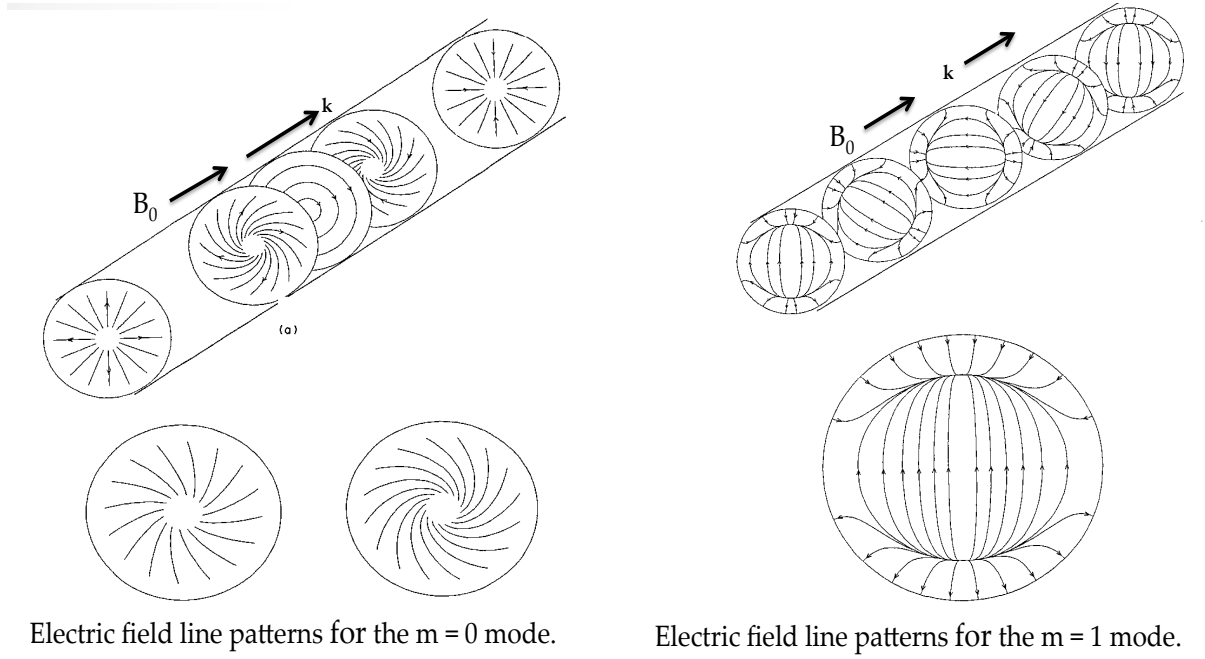
Figure 2.2: The wavefronts of the helicon wave shown for the two cases $m = 0$ and $m = +1$ helicon mode. Source: F. F. Chen, Plasma Physics and Controlled Fusion, **33**, 4, p. 339, 1991 [5].

is shown schematically in the figure 2.2.

- **m = 1 mode**

  In the $m = 1$ mode the field pattern remains the same spatially but the whole pattern simply rotates as we move along z [5]. The wavefront of the $m = 1$ mode is shown in figure 2.2.

2.6   Mode transition in Helicon Plasma

The helicon plasma has several signatures, one of the most important being the mode transition density jump from a lower density mode to higher density mode when either rf power or the axial dc magnetic field is increased. At low rf power the antenna is capacitively coupled with the plasma. At this stage, the plasma is

characterized by high electron temperature and plasma potential and low plasma density. The capacitive mode of operation has larger skin depth such that the electric field from the antenna can couple directly to the plasma.

(a)   (b)
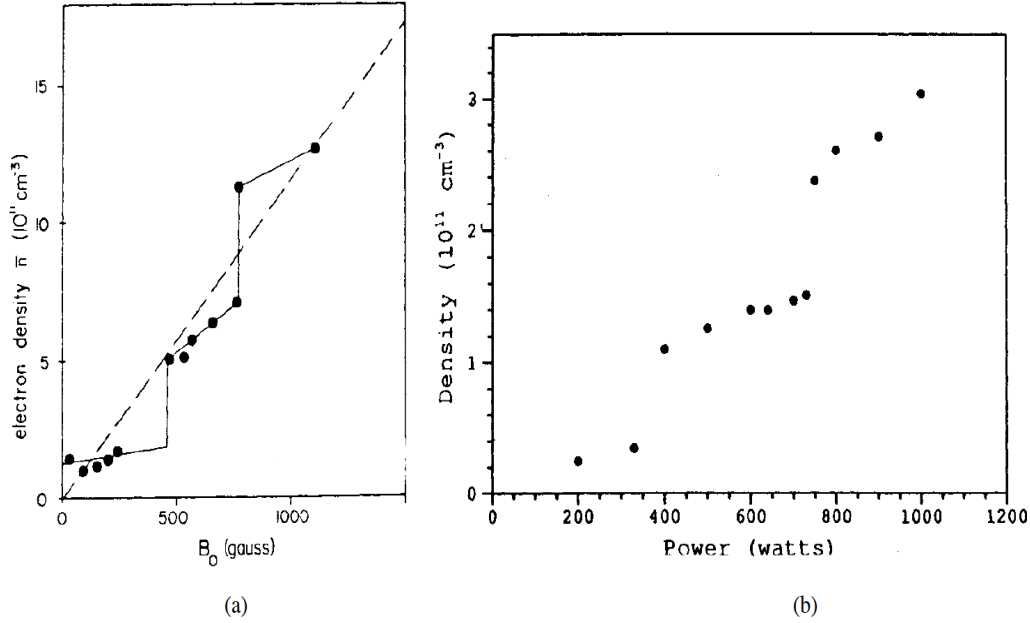
Figure 2.3: (a) Density jumps with increase in magnetic field [source: [6]] and (b) density jump with increase in RF power [source: [7]].

When the power is increased the sheath reduces to a thin layer at the boundary and there is a substantial $\partial\mathbf{B}/\partial t$ created in the plasma by the transformer action, where the plasma acts as the secondary coil of the transformer and the antenna behaves as the primary. The coupling at this stage is essentially inductive. This is identified with a jump in density and a sudden drop in plasma potential. A second jump in density might occur on further increasing the rf power marking the transition to the helicon mode. But in certain cases, the plasma goes directly from capacitively coupled to helicon wave heated plasma. Andrew Perry et al. [8] have explained that this behavior occurs for low axial magnetic fields. At low values of the axial magnetic field $\sim 30 - 60G$, the transition generally proceeds directly

36
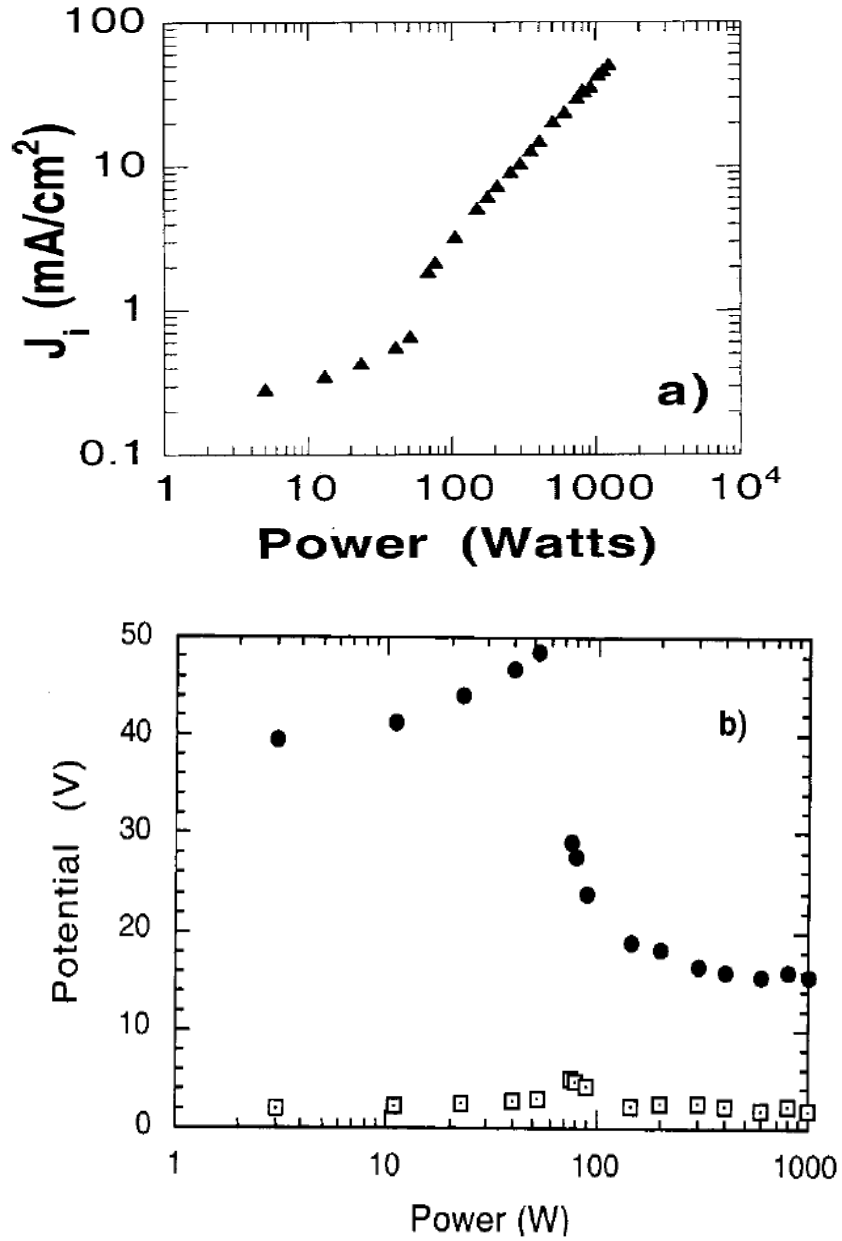
Figure 2.4: (a) Variation in the ion saturation current density and (b) the plasma potential V_p (solid circles) and floating potentials V_f (open squares) plotted as a function of source rf input power in argon gas at 2.5 mTorr. Source: [8].

from capacitive to wave sustained because a 1/2 wavelength Helicon wave can fit into the source axial dimension. This occurs because the Helicon wavelength is
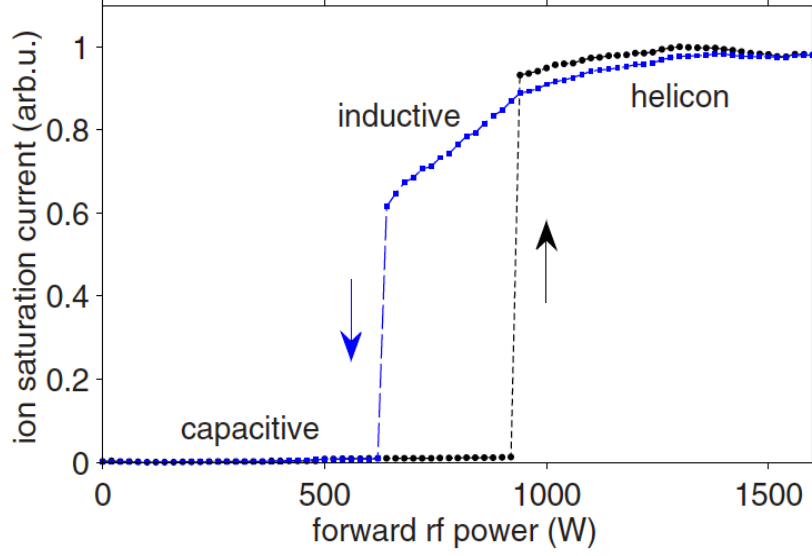
Figure 2.5: Capacitive, inductive, and helicon mode transitions are shown on increasing and decreasing the RF input power. Source: [9].

proportional to the square root of the axial magnetic field divided by the plasma density and hence, if the axial magnetic field is decreased the density required to sustain the helicon wave in the plasma can decrease for the same wavelength.

The density jump is also observed by increasing the externally applied axial magnetic field. The strength of the dc field can vary the dielectric tensor of the plasma and excite the electromagnetic modes such as the helicon wave. This happens because the magnetic field is greatly responsible for creating the charge separation in the plasma through $\mathbf{E} \times \mathbf{B}$ motions of the electrons and ions, where the electric field induced by the antenna and the axial magnetic field participate.

Figure 2.3 shows the experimental plots of two ways of inducing mode transition in magnetized RF plasmas i.e. either by increasing the magnetic field or by increasing the RF power. Initially, the discharge is low density capacitively coupled, which proceeds through an intermediate inductively coupled plasma to finally attain high densities and operate in the helicon plasma range as the RF power increased. This picture becomes slightly different when the RF power is in-

creased in a low magnetic field plasma. This type of plasma can make a transition directly from capacitive to helicon mode of operation as shown in figure 2.4. The reason for this is already discussed above. This mode transition is also seen in the plasma potential. The plasma potential (V_p) drops down in inductive/helicon mode from a higher V_p value of the CCP mode. Figure 2.5 shows a similar profile, where the capacitive mode directly goes into the helicon mode on increasing the RF power. But, if the power is reduced from thereon the intermediate inductive mode can be obtained.

3

Conceptual Design of experimental setup (HELEN-I)

This chapter describes the conceptual design of a permanent magnet based single driver helicon plasma source worked out with the help of two computer codes namely, HELIC and BFieldM. BFieldM is used for simulating the magnetic field topology for the ring magnet. The results from this code are used as input in optimizing the magnet location which is linked to the field value and uniformity inside the source chamber. An approximate calculation of the expected plasma density is also carried out to estimate the performance of the design. The results shown in this chapter have been published in a peer reviewed journal [93].

3.1 Introduction

The basic design of the plasma source consists of a helicon antenna wound around an insulating chamber, RF power source and a ring magnet placed above the source chamber. The source is designed with a focus on creating a high density plasma. For this purpose, we try to optimize the geometry, antenna configura-

tion and magnetic field inside the source. There are several tools available for this purpose namely, COMSOL, CST Microwave Studio and HELIC. The HELIC code is an open source code developed by Arnush et al. [16, 94] for helicon wave study in plasmas. The inputs are the RF antenna type, feed gas, geometry of the source, magnetic field, gas pressure, electron temperature, and plasma density. Magnetic field distribution due to permanent ring magnets is calculated by BfieldM code. The plasma source thus conceptualised comprises of a cylindrical glass vessel (source chamber) of diameter $\sim$ 50mm and height $\sim$ 50mm. The size of the ring magnet is fixed to match the dimension of the glass vessel (i.e. inner diameter $\sim$ 50 mm, thickness $\sim$ 10mm) so that the field lines inside the source are uniform. The magnet is placed above the source to get the required magnetic field in the glass source.

3.2   Magnetic Field Optimization

Excitation of the helicon wave in the plasma requires an axial magnetic field of sufficient strength. The first parameter to be optimized is how the magnetic field topology looks like inside the source chamber because of the permanent magnet. The magnetic field of a permanent magnet rapidly decays with the distance from the magnet and diverges out. The field lines are rapidly diverging in the region too close as well as too far from the magnet. Therefore, the source should be at a distance from the magnet where the field lines traverses the total length of the source chamber and are radially uniform at the same time. An NdFeB permanent ring magnet with a surface field of $\sim$4.5 kG is used for the purpose of providing the axial field. This field strength is sufficient for a permanent magnet to be used in the place of the generally used electromagnets. The use of a permanent magnet is beneficial in the sense that it makes the whole device much more simple and compact by getting rid of all the electrical and cooling water interfaces that

42

would otherwise be required for electromagnets. This in turn reduces the maintenance required for a long term steady operation. This topology is simulated using BFieldm. The input to the simulation is through an input file which includes the the number of magnets, the magnet dimensions given in terms of the spatial coordinates, number of grid points for the calculation of field lines, number of field lines required in the plot and the magnetization. Since neodymium magnets are one of the strongest permanent magnets available, they are usually small and compact. The magnet used for HELEN setup is a ring magnet with inner diameter $\sim 50mm$, outer diameter $\sim 100mm$ and thickness $\sim 25mm$. The axial variation of the magnetic field due to this magnet is shown in figure 3.1. The figure shows the axial profiles for different radial positions denoted by r. The abscissa is the distance from the centre of the magnet, which is at $z = 0$. The plots start from 3 cm away from the centre of the magnet and show that initially the field is radially not uniform. But for $z > 7cm$ the radial variation of B_z, is not significant. The region $z > 7cm$ is suitable for placing the source tube for plasma generation. The value of magnetic field inside the source can be varied by varying the separation between the source and the magnet. The magnitude of the field inside the source is crucial because of several factors. Some of these will be discussed in the next section. The magnetic field should be sufficient to magnetize the electrons, but low enough leave the ions unmagnetized.

The setup schematic showing the placement of the source tube is shown in figure 3.4. It can be seen from the figure that the source tube is placed in such a way that the magnetic field lines traverse the full length of the tube. On the right, is the calibration plot of the magnetic field of the permanent magnet, where the values of the axial field obtained from the BFieldM simulation is plotted alongside the magnitude of the axial field measured by a Gaussmeter. The magnetization value for the present case is found to be ~ 8300.
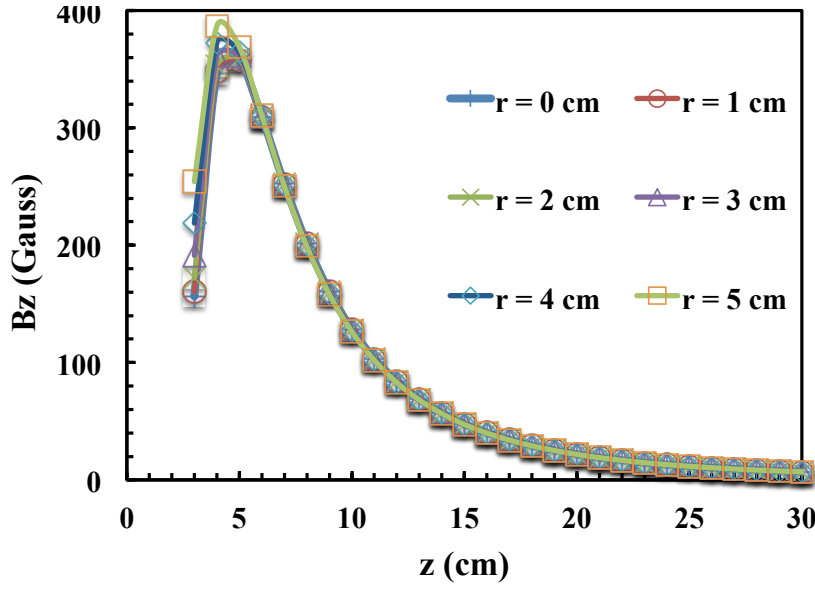
Figure 3.1: Axial variation of B_z at different radial positions. $z = 0$ is the magnet centre.
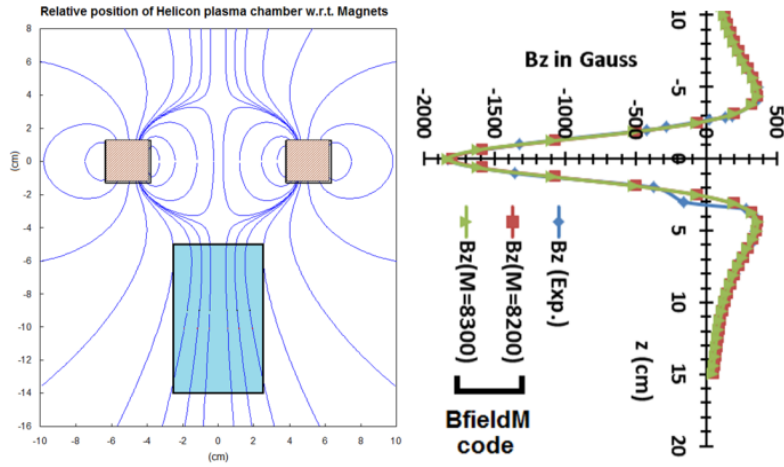
Figure 3.2: Magnet field lines from a ring magnet. A rectangular area depicts the probable zone where the discharge tube can be placed on the axis.

3.3 Results

To understand the results from HELIC we should define certain terms which are the output from HELIC and being used here as optimizaton parameters. To do that we consider a plasma chamber geometry as shown in figure 3.3. The plasma and the RF generator system can be represented by a simple electrical model as shown in figure 3.4. Here, R_P gives the plasma resistance which is a measure of the RF power coupled to the waves in the plasma. Higher value of R_P would indicate a higher efficiency of the antenna power coupling to the wave for a given mode of operation (CCP, ICP or Helicon, see section 2.6).
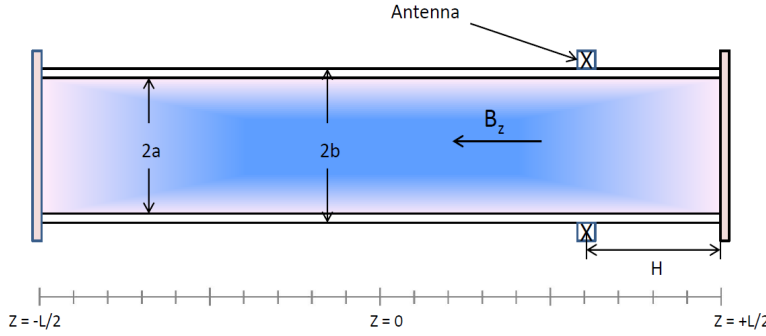
Figure 3.3: Geometry of plasma chamber considered. H indicates the distance of the antenna from the endplate.

The power dissipated through the resistor R_P in figure 3.4 is given by

$$P_{in} = P_{RF}\frac{R_P}{R_c + R_P} \tag{3.1}$$

where, P_{RF} is the input RF power and P_{in} is the power coupled to the wave. This P_{in} can also be computed from HELIC. The resistance R_c is the equivalent resistance including all the circuit losses including radiation loss, energy utilized in plasma production, losses due to heating of the antenna and eddy current losses. It should be noted that we have assumed that the impedance matching has already
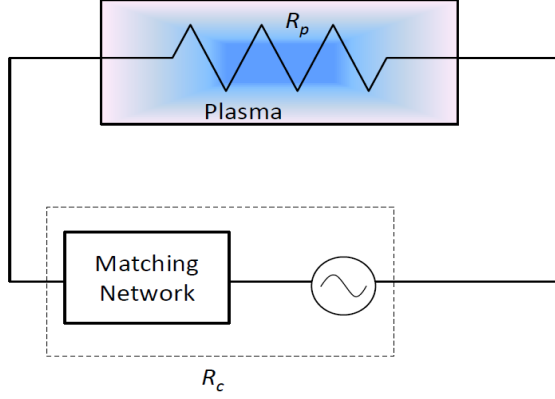
Figure 3.4: Schematic of the electrical system showing circuit resistance R_c and the plasma loading R_P.

been taken care of by the matching network and the maximum power is being transferred to the antenna. The next step after that is to couple this power to the helicon wave, which would eventually transfer it to the plasma through a damping mechanism, which we do not take into account at this point.

For the case of relatively smaller circuit losses, i.e. for $R_c << R_P$, $P_{in} \sim P_{RF}$. It is assumed that most of the power is coupled to the antenna-plasma system. Therefore, we focus on maximizing the value of R_P for a given set of input parameters in the helicon mode of operation. Through this methodology, we arrive at the optimized values of the plasma dimensions, magnetic field, antenna type and neutral pressure. For calculating these parameters for a given antenna type, cavity dimensions, plasma density and magnetic field HELIC is used. A uniform plasma in a uniform magnetic field is assumed. In the simulations the antenna centre is taken to be the same as the cavity centre, which is at $z = 0$. A bounded plasma cavity with an plasma radius a, antenna radius b and cavity length L is considered. The separation between the antenna and the endplate is H.

Other design parameters include the a) antenna type which is responsible for

the launching waves in the plasma and for power coupling to the plasma [95], b) discharge volume which determines the power requirements, c) type of end-plate which influences plasma profile and power coupling inside the discharge volume [96] and d) the driving frequency of the input power. A conceptual design is framed by iteratively running the HELIC code for each of these parameters keeping other parameters fixed.

Figure 3.5 shows the effect of cavity length on the plasma resistance, denoted by R_P for a hydrogen plasma created using a 13.56 RF power input, a loop antenna, axial field $B_0 = 110G$ and plasma radius $a = 2.5cm$. From the figure it can be seen that for lower cavity lengths the R_P value is higher for same plasma density. Thus, the total cavity length should be less than 40 cm to get maximum possible R_P. For further calculations, we fix the cavity length $L = 40cm$. Simulations also show that at higher fields we would certainly require a longer cavity but for the present case a field strength of $< 150G$ is most relevant.
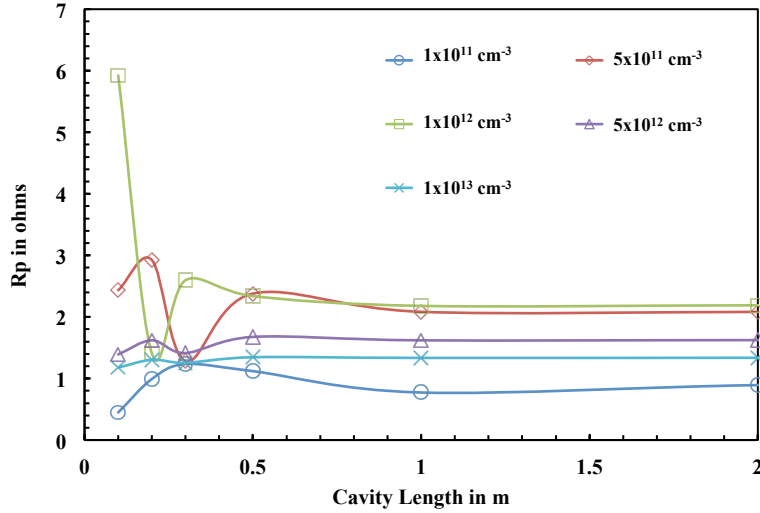
Figure 3.5: Variation of plasma resistance with cavity length for different plasma densities at 10 mTorr pressure, 3eV electron temperature, $B_0 = 110G$ using a 13.56 RF input and a single loop antenna.

Using the same input parameters as stated above with $L = 40cm$ a radial

profile of the power coupled to the wave inside the discharge volume is obtained for different axial magnetic fields as shown in fig. 3.5. For lower fields, the plasma discharge is inductive type since all the power is deposited at the plasma boundary and there is almost no power coupling at $r = 0$. Whereas, the power coupling in the centre starts to increase beyond $B_0 = 40G$ and is significant at higher value of B_0. The power coupling to the bulk of the plasma indicates plasma marks the helicon wave excitation which can penetrate inside the plasma volume. This plot gives an idea of the minimum value of the axial field that would be required for exciting the helicon wave in the plasma. From figure 3.1 and figure 3.5 the appropriate location for the magnet with respect to the source tube is chosen.
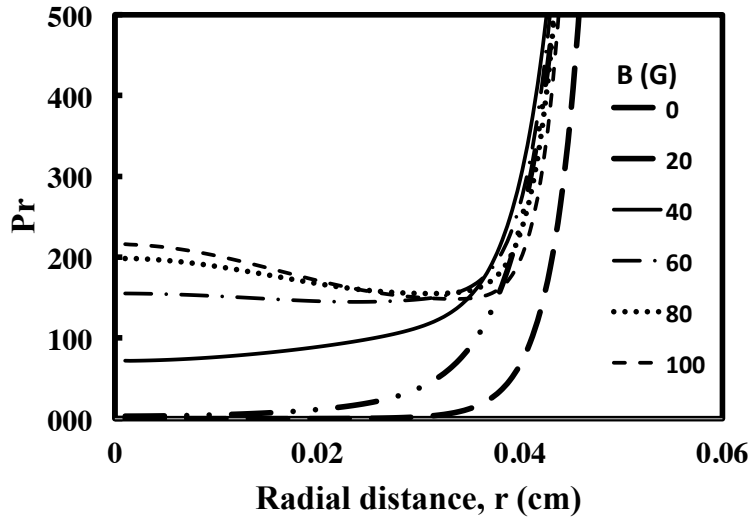
Figure 3.6: Excitation of the helicon modes and density increasing on the axis when the magnetic field B_z is increased. $B = 0$ G is the pure inductively coupled plasma configuration, and $B > 40G$ helicon mode starts dominating.

Figures 3.7 shows the variation of plasma resistance R_P with plasma density for different values of B_0. The peak of R_P curve moves toward higher density value as B_0 is increased from 40 G to 100 G. The peaks in the individual plots represent a mode transition. The region after the peak correspond to the higher density mode.

48
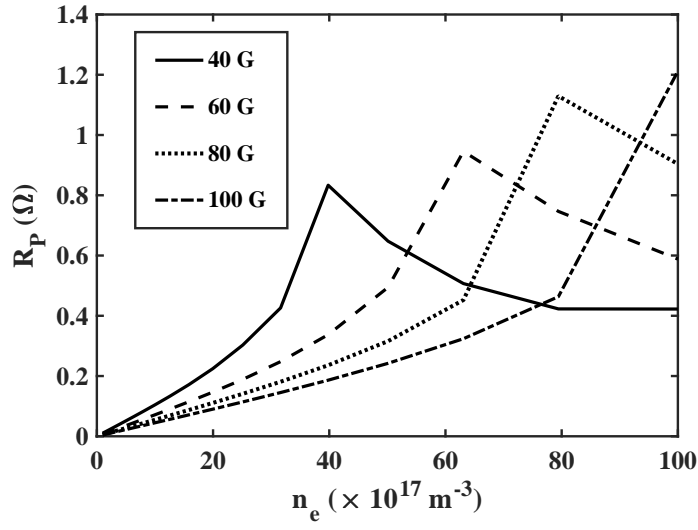
Figure 3.7: Variation of plasma resistance R_P for different plasma density conditions in presence of different axial magnetic field values. The driving frequency is 13.56 MHz.

In this mode, a higher density is obtained for same value of power coupled (R_P). These peaks occur at lower density values for lower magnetic fields as described by Shamrai [18].
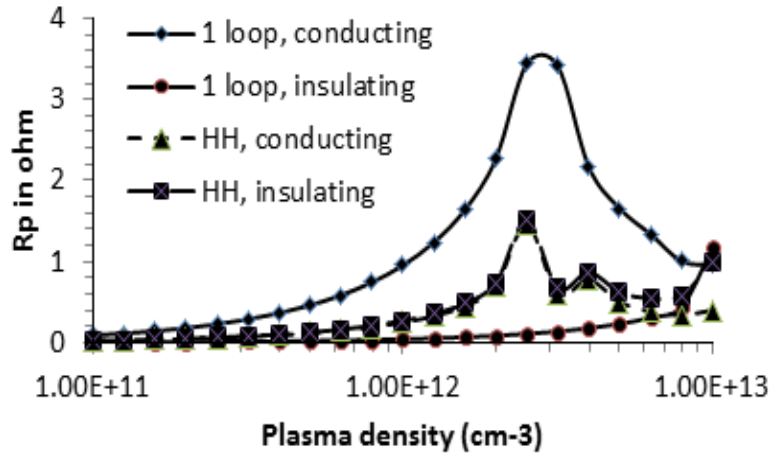
Figure 3.8: Helicon discharge comparison obtained with Half-Helix and Loop antenna with different endplate configurations.

F.F. Chen [97] had shown the importance of helicon wave reflection from the endplates and the interference of the waves to achieve higher plasma density. Therefore, it becomes important that we see the effect of the endplate material on R_P. This simulation result is shown in figure 3.8, which compares different endplate materials for two types of antennae. From the figure, we see that the maximum R_P is obtained for the case of a conducting endplate with the single loop antenna.
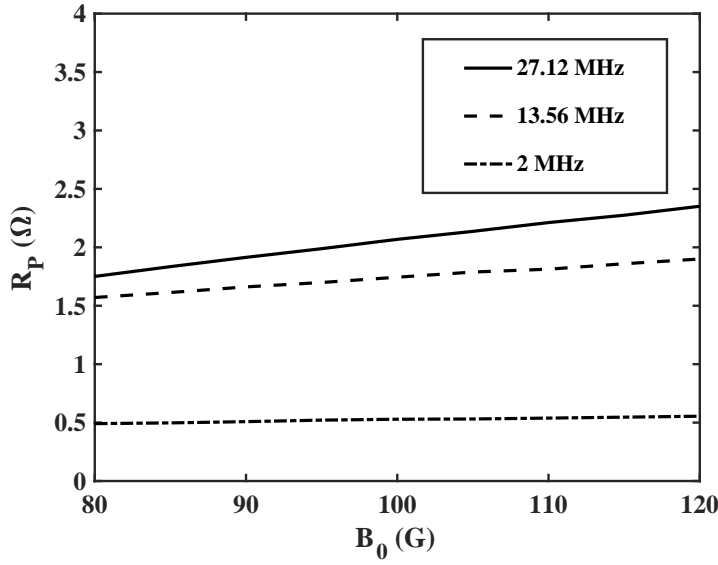
Figure 3.9: Variation of Plasma Resistance with magnetic field for different frequency values.

The frequency of excitation of the helicon wave lies between ion cyclotron frequency and electron cyclotron frequency. For a hydrogen plasma the frequency of excitation or the driving radio frequency of the input power should be more than ~ 1 MHz. Frequency dependence of the plasma resistance is shown in figure 3.9 for plasma density value relevant to ICP plasmas ($n_e = 10^{12} m^{-3}$). The figure shows that for 2 MHz the value of R_P is low whereas, for 13.56 MHz and 27.12 MHz cases we get significant increase in R_P. A 13.56 MHz RF generator is easily available commercially and is sufficient to excite helicon wave inside the discharge. Hence,

13.56 MHz is chosen as the driving frequency for the plasma setup.

Antenna type affects the plasma performance in the most crucial way. The antenna is a part of the total load of the circuit and hence responsible for power coupling from the generator to the plasma. Since, the excited wave properties would also depend on the type and dimensions of the antenna, it is essential to study the power transferred by different types of antenna. From fig. 3.10 it can be seen that single and double loop antennae couple most of the power under the antenna location. The magnitude of the power coupled is also greater for these two cases. These two results combined would lead to choice of a smaller source volume if we choose a loop antenna. This would make the source compact and reduce power consumption. In the figure 3.10, the centre of the antenna is placed at $z = 0$. It was demonstrated by Kamenski [98] and Melazzi and Lancellotti [99] and that a loop antenna gives better performance for smaller plasma cavities at relatively low densities.
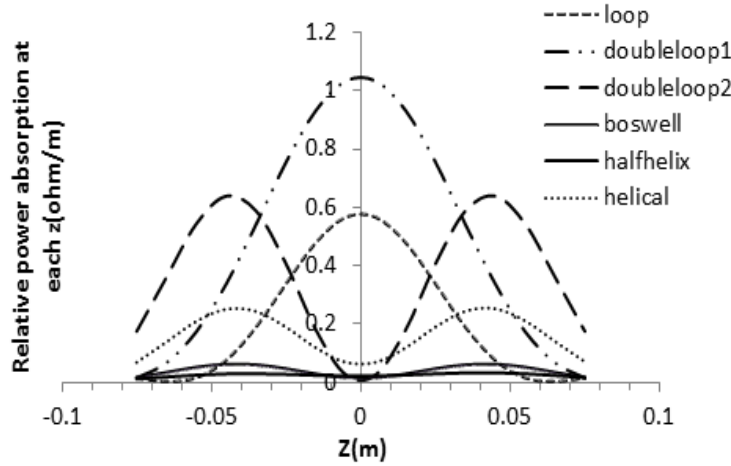
Figure 3.10: Comparison of antenna power coupling to the wave for different antenna types.

3.3.1 Plasma Loss Rate calculation

The equilibrium plasma density is obtained when input power (P_{in}) exactly balances the power required to sustain the discharge (P_w) and the losses due to joule heating and eddy currents (P_L). The latter two can be grouped into a single quantity $P_{out} = P_w + P_L$. The P_{out} is proportional to the plasma density n_e as shown by Shamrai [100]. But, the variation of P_{in} with plasma density is neither linear nor monotonic. If we plot these two plot alongside each other their intersection will give the stable operating point as shown in fig. 3.11. This intersection point corresponds to the equilibrium plasma density point.

For the above mentioned power balance calculation and density estimation, a simplified model is assumed. A uniform plasma is assumed with magnetized electrons and unmagnetized ions. Electrons collide with ions, neutrals to lose energy and ultimately lost at the sheaths near the vessel walls. Plasma losses are determined by the ion losses, the electrons following at the same rate in order to preserve quasi-neutrality. The ion neutral collisions are scarce and ions free-fall to the sheaths at the walls. The loss rate of ions is given by:

$$-\frac{dN}{dt} = \frac{1}{2}n_e C_s A \tag{3.2}$$

where, N is the ion density, $A \sim 45 \times 10^{-3} m^2$, is the total surface area of the plasma chamber with $a = 54mm$, $h = 50mm$ and C_s is the ion acoustic speed. At steady state, the total energy carried by an electron-ion pair to he walls is given by

$$W = W_i + W_e + E_c(T_e) \tag{3.3}$$

where, $E_c(T_e)$ is the sum of energies used up in the ionising and inelastic collisions. Using equations 3.2 and 3.3 we can arrive at an expression for P_{out}:

52

$$P_{out} = \frac{dN}{dt}W = \frac{1}{2}n_e c_s A W \qquad (3.4)$$

which is proportional to plasma density. For a hydrogen plasma, $E_c(T_e) \sim 36$ eV; $W_e = 2T_e$ and $W_i = (0.5T_e + 2.8T_e)$. Assuming $T_e = 3eV$, W ~ 51.9eV $\sim 83.4 \times 10^{-19}J$ and from equation 3.4 the value of $P_{out} \sim 8.3 \times 10^{-11}n_e(Watt)$.

P_{in} and P_{out} are plotted as functions of the plasma density for $B_0 = 100G$ in figure 3.11. The cross-over point between the two curves gives the equilibrium point. The plasma density corresponding to this equilibrium point sustainable density for the assumed configuration. Beyond the cross-over point the loss part dominates and overall plasma density goes down.
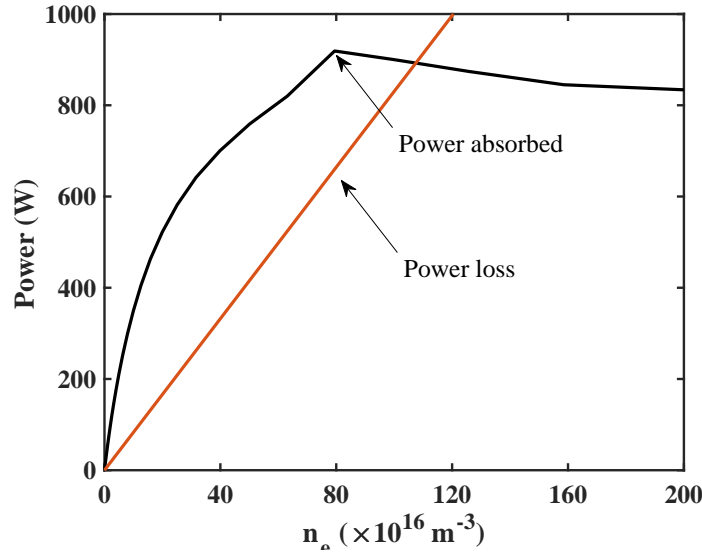
Figure 3.11: Typical power balance calculation for hydrogen plasma of temperature $T_e = 3eV$. Stability point indicates probable steady state plasma density (max) achievable in the configuration using 1kW RF generator of frequency 13.56 MHz, circuit resistance $R_c = 0.1\Omega$, Magnetic field = 100G. P_{in} (solid line) is calculated using HELIC code and P_{out} (dashed line) is calculated using equation 3.4. The cross-over point indicates the power balance and corresponding plasma density on horizontal-axis is the sustainable plasma density in that configuration.

Based on the above simulation study, a permanent ring magnet based helicon plasma source configuration with single driver using hydrogen gas and a RF gen-
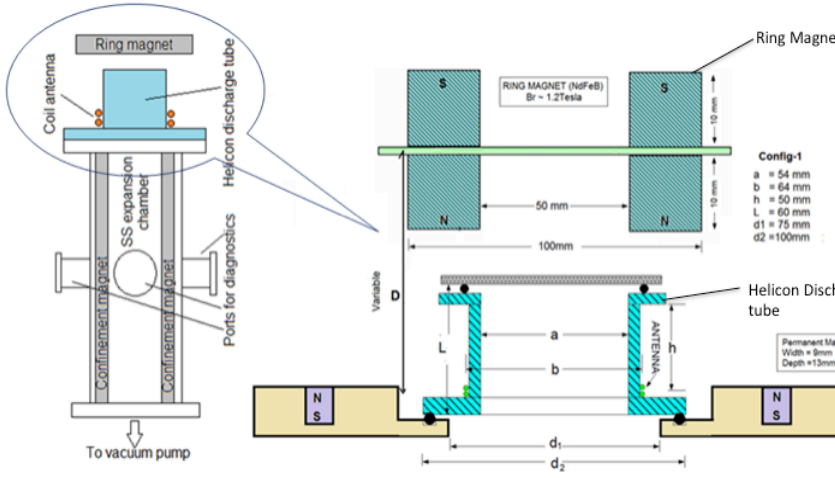
Figure 3.12: Schematic of the proposed helicon plasma source experimental setup and the configuration.

erator of frequency 13.56 MHz is finalized. This configuration is considered to initiate the experiment. In the subsequent chapters we show the characterization of the plasma first with Argon to understand the properties of the helicon plasmas and then move on to developing the helicon source for experiments with hydrogen plasma.

Experimental Set-up and diagnostics used

After the conceptual design is finalized, the fabrication of the helicon source is initiated based on the conceptual design. There are several other design considerations related to magnetic field configuration, geometrical constraints and antenna configurations based on the desired plasma parameters and profiles for fabrication. These considerations should be kept in mind along with the simulation results from previous chapter 3. In this chapter, we discuss these design considerations and fabrication of the experimental set-up along with all the diagnostics used in the HELEN-1 setup so far.

4.1 Design Considerations

After a detailed geometric and parametric optimization in chapter 3, we look at the basic design considerations for a compact helicon plasma experiment. A helicon plasma source is essentially a magnetized inductively coupled plasma source such that the RF power of frequncy ω, applied for the plasma production lies in the range:

$$\Omega_{ci} << \omega_{LH} << \omega << \omega_{ce} \tag{4.1}$$

where $\Omega_{ci}(\omega ce)$ is the ion (electron) cyclotron frequency and ω_{LH} is the lower hybrid frequency. Boswell (1984) [6] showed the efficient production of plasma with bounded whistler (helicon) waves near lower hybrid frequency, using a 8 MHz RF source, with the primary aim of coupling the RF energy into the centre of a magnetoplasma and have the energy transferred to the plasma particles.He demonstrated the use of helicon waves and since then a great deal of interest has been drawn towards producing a high density plasma with helicons and exploring their applications. Therefore, the frequency is chosen on the basis of the above mentioned criterion and its availability. A 13.56 MHz source is readily available and as shown in the previous chapter, its efficiency is close to the 27.12 MHz source.

An RF generator will transmit the power through an amplifier to a radiating antenna. Different types of antennae have been compared in the figure 3.10 for a given power. For a small cavity, the power deposition in the cavity is maximum for double and single loop antennae. The double and single loop antennae also have another advantage that they are shown to excite $m = 0$ helicon mode in the plasma. The $m = 0$ mode is the simplest to understand because of the azimuthal symmetry. A loop antenna is, thus, the preferred choice for a compact helicon plasma source. Sakawa [101] has demonstrated the use of a single loop antenna in exciting the helicon wave in the plasma and producing a high density plasma.

The cavity size would affect the power absorption and ionization. Since we are focussing on creating a compact source, a smaller cavity size is preferred. The simulations in chapter 3 have shown that an source tube of $\sim$ 50 mm length and $\sim$ 50 mm diameter can be used for efficient plasma creation. Chen and Torreblanca [21] have also shown the use of smaller plasma cavities for the efficient plasma production.

An axial magnetic field in the source chamber is one of the main ingredients for a helicon plasma source fabrication. The requirement of the axial field comes from the physics discussed in chapter 2. Conventionally, several electromagnets

are used to provide an axial magnetic field for the excitation and propagation of helicon waves in the plasma. An important change in HELEN is the use of permanent magnets. The permanent magnet serves multiple purposes. One of the most important advantages is that the interfaces involved with the electromagnets can be completed avoided. This makes the permanent magnet based helicon source more convenient and more preferred option in applications such as space plasma thrusters. Helicon plasma sources with permanent magnets have been developed by Virko et al. [20] with radially magnetized cylindrical magnet assembly and by Takahashi [22] using a double concentric array of permanent magnets to provide a constant field area inside the source and a diverging magnetic field at the outlet of the source. Chen and Torreblanca [21] have used a stack of annular permanent magnets to provide an axial DC field inside the source which diverges downstream in the expansion chamber. This setup is very similar to the field configuration for the HELicon Experiment for Negative ion source-I (HELEN-I). HELEN uses a ring magnet placed above the plasma source. A detailed description is given in section 4.2.2.

The applied field required for the excitation of the helicon plasma should be such that the condition 4.1 is satisfied. If the field is too large ω_{LH} may exceed ω in that case the criterion would not be satisfied. At the same time the field in the source region near the antenna should be high enough such that the field is radially uniform in the source and is large enough for producing charge separation through $\mathbf{E} \times \mathbf{B}$ drifts for the excitation of the helicon wave. The field is necessary for $\mathbf{E} \times \mathbf{B_0}$ drift, which would work in alliance with the polarization drift, arising from the time variation of $\mathbf{E}$, and lead to charge separation and setup radial and azimuthal electric field associated with the wave. The divergence of the field coincides with the geometrical divergence, such geometries have been studied in context of plasma thrusters where a double layer formation takes place due to the spatial gradients in axial magnetic field. Due to the configurational similarities,

research on thrusters based on helicon plasma source can also be carried out in HELEN. In addition to a ring magnet placed above the source, the expansion chamber has an array of permanent magnets to provide a cusp field configuration for plasma confinement. The arrangement of the confinement magnets along with its advantages is discussed in section 4.2.3.

4.2 HELEN-1 Setup
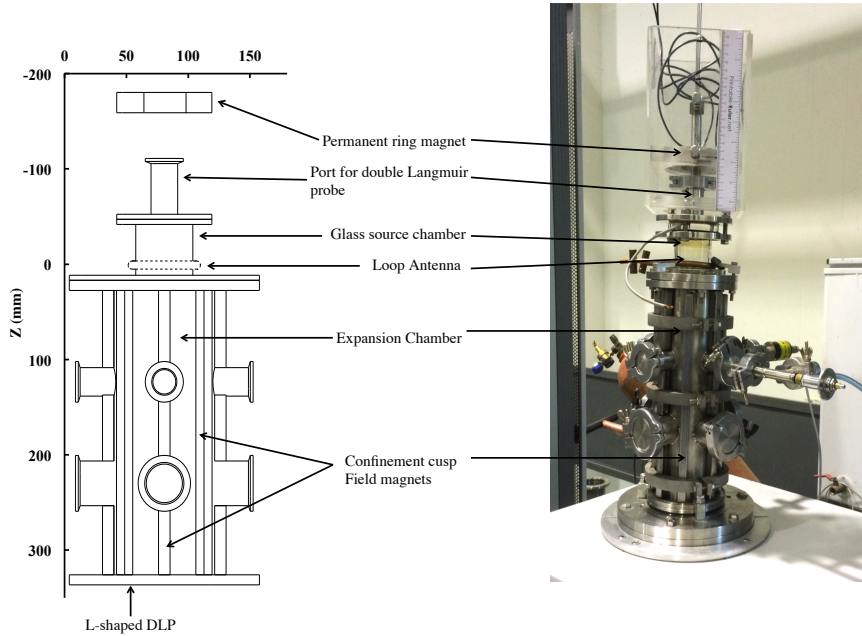
Figure 4.1: HELEN Experimental setup

The experimental setup, as shown in figure 4.1, consists of a source tube made of glass (length = 70 mm, inner diameter = 50 mm, outer diameter $\sim$ 70 mm), a permanent ring magnet (thickness = 25 mm, inner diameter = 50 mm, outer diameter $\sim$ 100 mm) of surface field $\sim$ 0.4T placed above the source to provide a dc axial magnetic field, a stainless steel expansion chamber (length $\sim$ 300 mm,

inner diameter = 100 mm, outer diameter = 115 mm), diffusion pump backed by a rotary pump, RF antenna, RF shield around the source, RF Generator (13.56 MHz, 1.2 kW), Matching unit (L-type network), the diagnostic setup and water cooling lines for vacuum pump and RF generator. The insulating source tube is required to allow the RF field to penetrate through it to reach the plasma, whereas the diagnoses are carried out mainly in the expansion chamber to avoid the RF noise. The helicon plasma experimental setup has been designed with a consideration that a high density plasma is created in the glass source by the antenna placed just outside the source tube. The plasma would then diffuse into the expansion chamber. The plasma sees a geometric and magnetic expansion as it moves downstream. To compensate for the geometric expansion and reduce the loss area a cusp magnetic field configuration is used in the expansion chamber, which has the field free diameter nearly same as the inner diameter of the glass source ~ 50 mm. This configuration of magnetic fields in the source and expansion chamber helps in the formation of high density plasma and reduce the losses to the walls.

4.2.1 Source Chamber

The source part primarily consists of an insulating chamber on which the antenna is mounted. The glass source tube chamber in HELEN has an inner diameter of 50 mm and is 70 mm long. On the top glass tube terminates in a stainless steel flange containing a port for axial profile scanning of the plasma. A magnet holder is placed on the top of the glass tube. This magnet holder is made from acrylic and it holds the magnet above the glass plasma source on an axially movable plate with a scale, such that the vertical separation between the magnet and glass tube can be varied by moving the plate.

For maintaining a compact size of the source, it is seen from figure 3.10 that a loop antenna deposits maximum power in its vicinity and it is the simplest
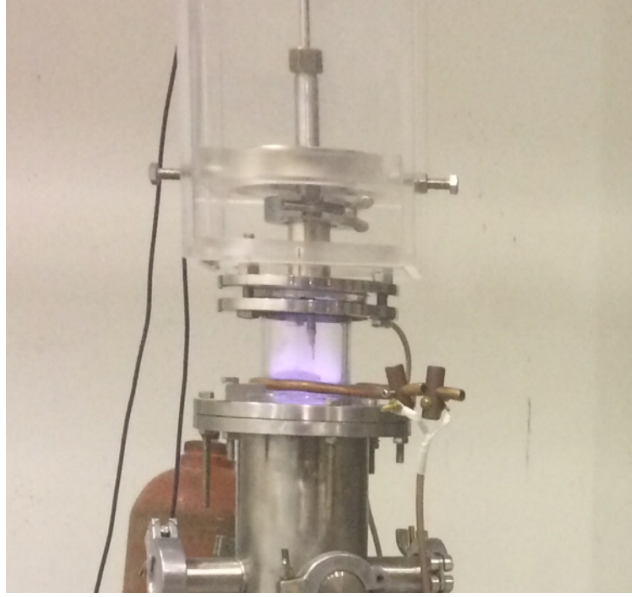
Figure 4.2: Glass source chamber with single loop antenna made of copper tube of 8mm OD and 4mm ID used in the experiments with Argon gas.
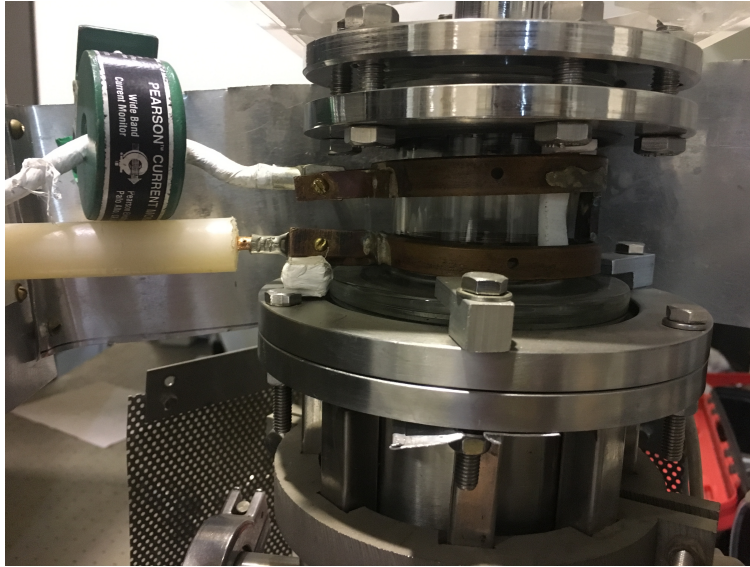
Figure 4.3: Image of the Nagoya III antenna used with hydrogen gas to produce m = 1 Helicon mode in the plasma.

antenna among the group of antennae simulated. Therefore, a single loop antenna is fabricated and mounted for exciting $m = 0$ helicon mode in an inductively coupled plasma. The loop antenna is made out of a cylindrical copper tube of 8
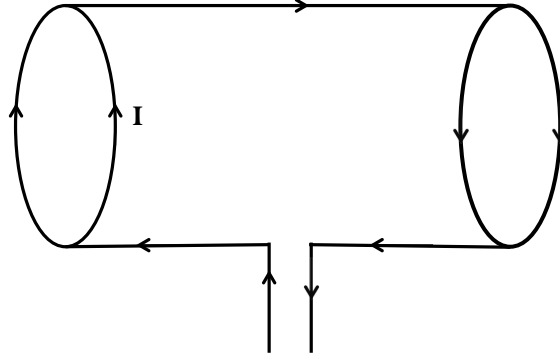
Figure 4.4: Schematic of the Nagoya III antenna and the relative direction of current (shown by arrows) producing m = 1 Helicon mode in the plasma.

mm outer diameter and 4 mm inner diameter. A hollow cylindrical copper tube has an advantage that it is easily mouldable to achieve the desired shape. Although, the main consideration is the prospect of active water cooling of the antenna, if it is required. A picture of the single loop antenna used with the experiments with Ar gas is shown in figure 4.2. A Nagoya III antenna is shown in figure 4.3. It is used in the experiments with Hydrogen gas. Details of the Nagoya antenna will be discussed in chapter 6.

4.2.2 Permanent Magnet for Axial Field

The axial field required for the helicon wave excitation in the plasma is provided by a ring magnet shown in figure 4.5. The NdFeB magnet used has a magnetization of ~ 0.83 T (8300 G) along the thickness of the magnet. The magnetic field profile is computed by plotting simulated curves alongside the experimental profile of the magnetic field intensity. The surface magnetic field is experimentally found to be $\sim 4.6 kG$. Figure 4.6 shows the comparison of the simulated and experimental data. The experimental values are obtained using a Gaussmeter (Laskeshore make) and the field of the permanent ring magnet is simulated using BFieldM code. The details of the calculation are already given in section 3.2.

Figure 4.5: Permanent Ring magnet for providing axial field inside the plasma source.
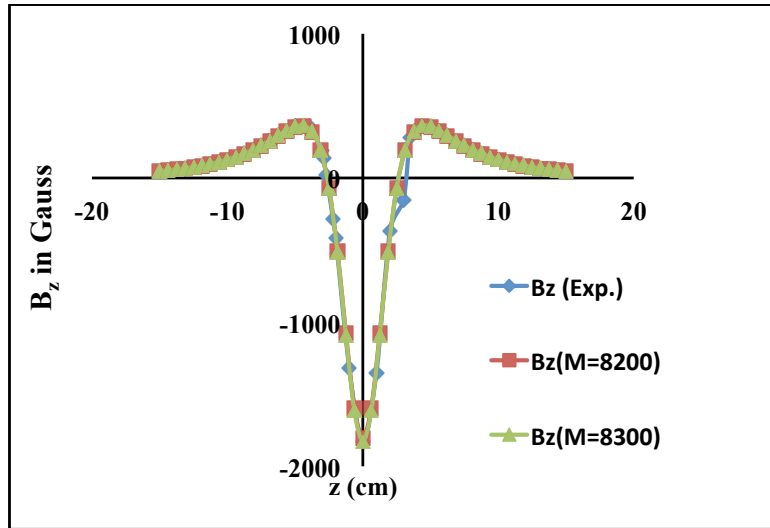
Figure 4.6: Characterization of the permanent magnet. Magnetization, M value given in the legend are in Gauss.

Figure 4.7 shows the field lines originating from the permanent ring magnet and diverging as they travel through the device. The dashed lines parallel to the abscissa intersecting the y-axis at 2.5 cm marks the location of the radial plasma boundary in the HELEN device, whereas, the dashed line parallel to y-axis marks the interface between the source and expansion chamber at z $\sim$ 3.5 cm. This is an

important figure because it shows that the magnetic field is more or less uniform in the source region but starts to diverge in the expansion chamber where plasma also faces a geometric divergence. To compensate for the geometric expansion the expansion chamber has been armed with an array of permanent magnets for confinement as discussed in the next section.
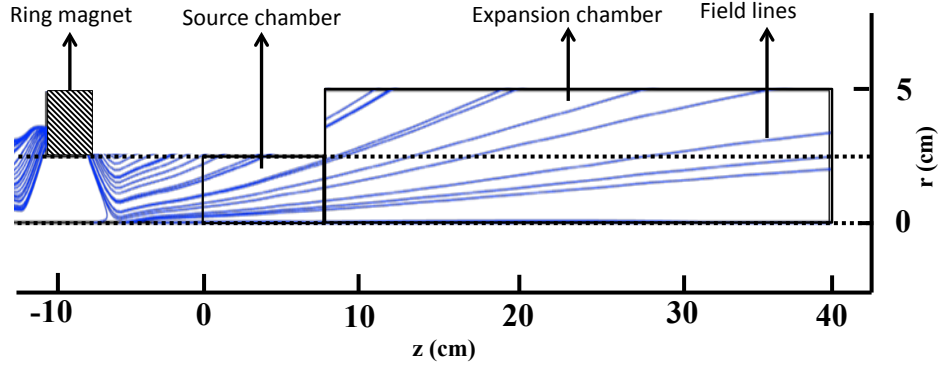
Figure 4.7: Typical profie of the diverging axial field lines in the HELEN-I device from the ring magnet.

4.2.3 Cusp Field Configuration

Since the plasma loss depends upon the loss area it is important for confinement that we reduce the loss area. This is done by introducing the cusp magnetic field configuration in the expansion chamber, which has an inner diameter of 100 mm. The cusp field configuration is created by small permanents stacked in an array cuboidal SS cases. Each magnet is 12 mm wide, 12 mm long with height = 2 mm and has a surface field strength = 0.40 T. Thus, a composite magnet is formed by sticking 6 such small magnets. Several of these composite magnets are inserted inside the SS case to form an elongated magnet. There are 16 cases in total.

The placement of these cases around the expansion chamber is given in table 4.1. The expansion chamber can be seen to be divided into three parts (4.1) by the diagnostic ports. The top part, the middle and the bottom.

Table 4.1: Placement of the magnet cases around the expansion chamber

Length of Magnet	Number of magnets and location
$\sim 90mm$	4 top
$\sim 60mm$	Total 8 (4 middle and 4 bottom)
$\sim 300mm$	4 along the length without ports

The cases are arranged along the length of the expansion chamber. The smaller cases (90 mm and 60 mm) are installed in between diagnostic ports, whereas the longer (300 mm) is installed at 4 locations without ports. These magnets are arranged around the circumference of the expansion chamber in a manner such that every alternate magnet has the same polarity. Thus, producing a line cusp field configuration inside the expansion chamber forming 8 cusps (where diagnostic ports are absent) and 4 cusps (where diagnostic ports are present).

The cusp configuration created in the chamber is simulated using COMSOL. The simulated profile is shown in figure 4.8. It can be seen from the figure that we get an almost field free region in the centre of the chamber with the field free radius ~ 2.5 mm. The field free radius is same as the radius of the source tube. This is the reason behind choosing 0.40 T composite permanent magnet arrangement described above. Thus, we try to keep the loss area minimum as the plasma diffuses into the expansion chamber.

4.2.4 RF Generator and Matching Unit

A T&C Power Conversion make 13.56 MHz RF generator with a capacity to provide up to 1.2kW RF power is chosen for the experiment. Figure 4.9 shows the RF Generator alongside the matching unit (T&C Power Conversion make). The RF
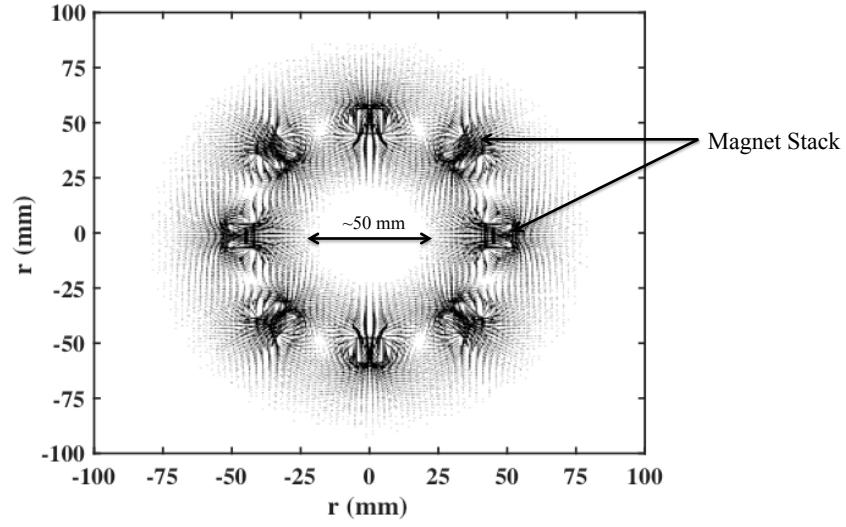
Figure 4.8: The cusp field configuration due to the confinement magnets around the expansion chamber.

generator is water cooled with water flowing into the generator from the back panel of the chassis The circuit of the matching unit is shown in figure 4.10. The antenna along with the plasma serve as the load in the electrical circuit. The circuit has a tune capacitor connected parallel to the load and a load capacitor connected in series with the load.

Figure 4.9: RF Generator and Matching unit for HELEN.
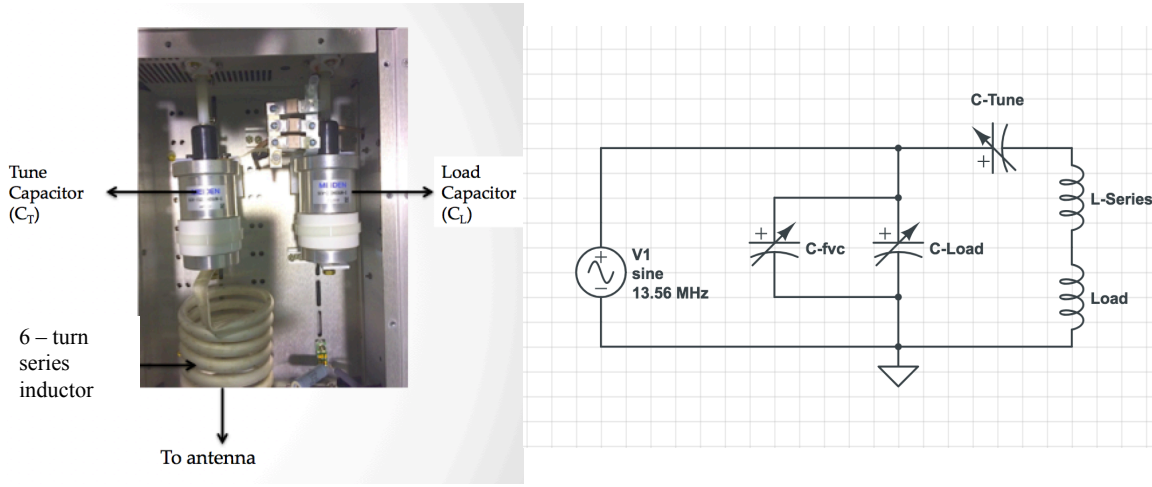
Figure 4.10: Image of the circuit of the matching unit along with the schematic of the circuit of the Matching unit.

The auto-tuning network makes sure that maximum power is transferred to the load at any time. For this purpose the matching network along with the load impedance should have an impedance value equal to the impedance of the RF Generator output which only has a real resistive part = 50 and no imaginary part. A variable tune capacitor (C_T) in the matching circuit is responsible for eliminating the imaginary part of the impedance whereas, a variable load capacitor (C_L) is responsible for keeping the total output impedance near 50.

The fixed value inductor L_{series} is $\sim 1\mu H$. The value of C-Tune (C_T) can be varied from 25 pF to 250 pF and that of C-Load (C_L) from 35 pF to 1000 pF. There are 3 other fixed value capacitors (FVC), C-fvc in parallel to C_T (one 240 pF and two 68 pF capacitors). This can be used to further adjust the value of (C_T) to modify the imaginary part of the impedance. For the HELEN experiment, perfect matching is established at $C_T = 16\%$ of its maximum value $= 40pF$, with the FVCs the total tune capacitance is $\sim$ 348 pF (40 pF + 240 pF + 68 pF) and $C_L = 79\%$ of its maximum value $= 790pF$ with the loop antenna and argon plasma 4.2.1. Whereas, for the Nagoya type antenna and hydrogen plasma, the values for

perfectly matched condition are $C_T = 18\%(45pF)$ with the FVCs the total tune capacitance is ~ 280 (40pF + 240 pF) pF and $C_L = 91\%(910pF)$. The inductance values of antenna as measured by a LCR meter are 239 nH for the loop antenna and 320.5 nH for the Nagoya antenna.

The shielding of the RF radiation from the antenna is required for a safe operation of the device from the point of view of the operators and to mitigate the effect of RF noise entering the data acquisition systems. An aluminium sheet of $\sim 0.45mm$ is used to shield the antenna and serves as the primary shielding. Whereas, a secondary shielding of SS mesh of thickness $\sim 0.3mm$ covers the whole device except for the diagnostic port locations. This helps to maintain the radiation level low near the operator location ($\sim 2m$ from the antenna). The radiated electric field at a location $1m$ away from the antenna (for Nagoya antenna) is shown in figure 4.11. The safety limit of operation for a 13.56 MHz RF source is 60 V/m and the shielding keeps the radiated field below the limit. The radiation from loop antenna is lower than the Nagoya antenna as we will see in chapter 6.
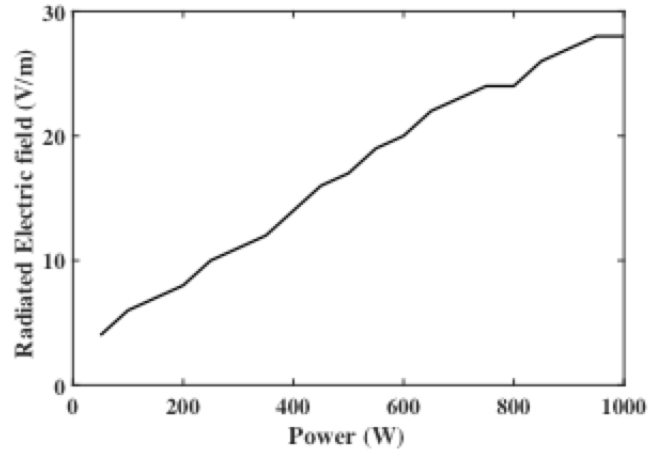
Figure 4.11: Radiated field from Nagoya antenna measured at $1m$ distance from the antenna.

4.3 Plasma Diagnostics

A schematic of the diagnostics used in the HELEN-I setup is given in the figure below 4.12.
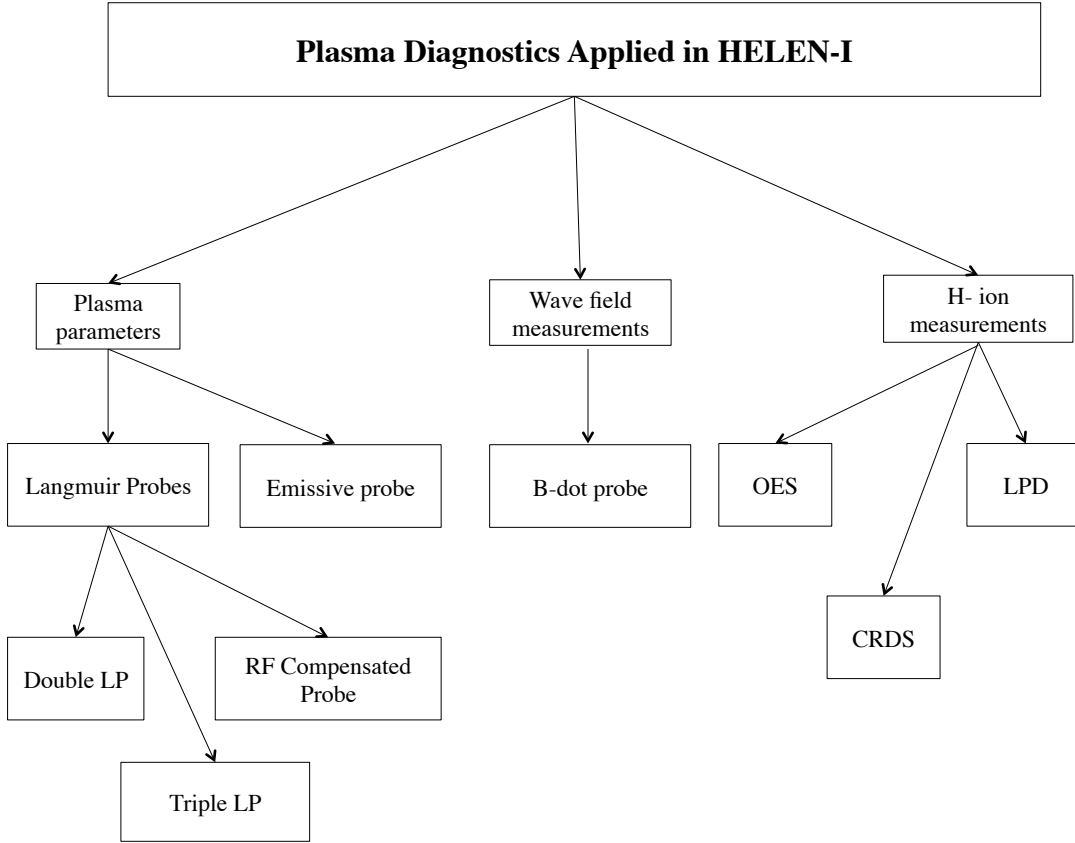
Figure 4.12: Schematic flow chart of the diagnostics categorised on the basis of their purpose.

4.3.1 Double Langmuir Probe

In single Langmuir probes with one pin as the probe tip, there is a requirement of a well defined voltage reference. In some cases, such a requirement poses a hindrance

in correct data acquisition, such as cosmic plasmas where a fixed reference is not present, plasmas with high electric potentials and plasmas where with rapidly oscillating potential. RF plasmas fall in the last category and a single Langmuir probe is not preferable for diagnosing RF plasmas due to associated uncertainties arising from the RF environment. A DLP signal is relatively less prone to RF noise pickup.
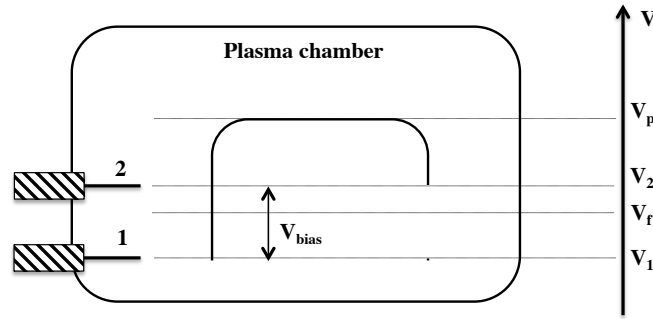
Figure 4.13: Cartoon of double Langmuir probe showing the voltage distribution schematic. V_p represents the plasma potential and V_f is the floating potential.

A double Langmuir probe is simply two single probes biased with respect to one another. Figure 4.13 shows a cartoon of a double Langmuir probe where two probe tips are shown to be connected through a power supply and a resistor. Since, the probes are biased with respect to one another, the whole probe system (including the circuit) is floating, which means that the net current drawn by the probe tips is zero. This happens because the two probe tips are oppositely biased at any time and the electron current drawn by the positively biased probe tip is equal to the ion current drawn by the other tip. This also means that the double probe measurement circuit should be isolated from the ground otherwise a finite current would start to flow through the circuit and the principle of the double probe measurement would not be valid. The voltage arrangement of the DLP is
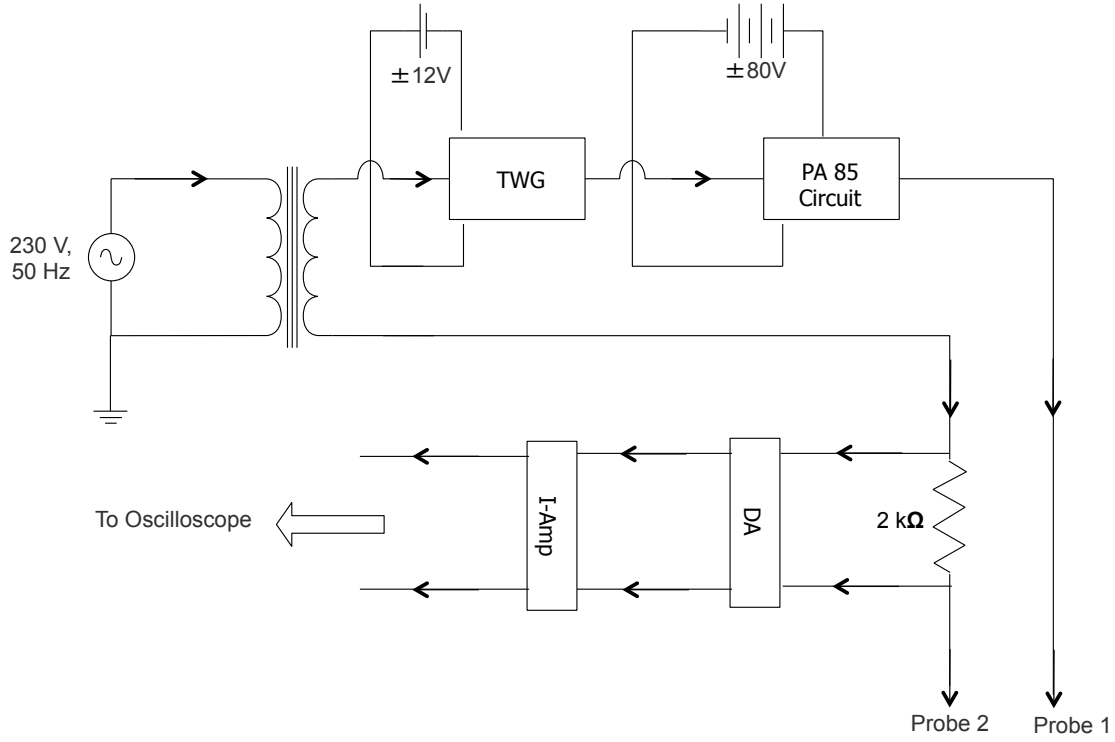
Figure 4.14: Circuit used for obtaining the double Langmuir probe data.

shown in figure 4.13 and the circuit used for the measurement is given in figure 4.14. The triangular wave generator (TWG) generates the $100Hz$ sweep voltage signal of $\pm 1V$ that goes into the power amplifier circuit for amplification. This is done through a PA 85 amplifier installed in a non-inverting configuration with a gain of $\sim$ 51. The circuit for the TWG is given in figure 4.15, whereas the circuit used for amplification is shown in figure 4.16. Components labeled as DA and I-Amp are differential amplifier and isolation amplifier respectively. A Knick module amplifier of VariTrans make is used as the isolation amplifier, the circuit diagram of the amplifier is shown in figure 4.17.

The current density through the electric circuit is the sum of electron current j_e and ion current j_i:

$$j = j_i + j_e \tag{4.2}$$

70
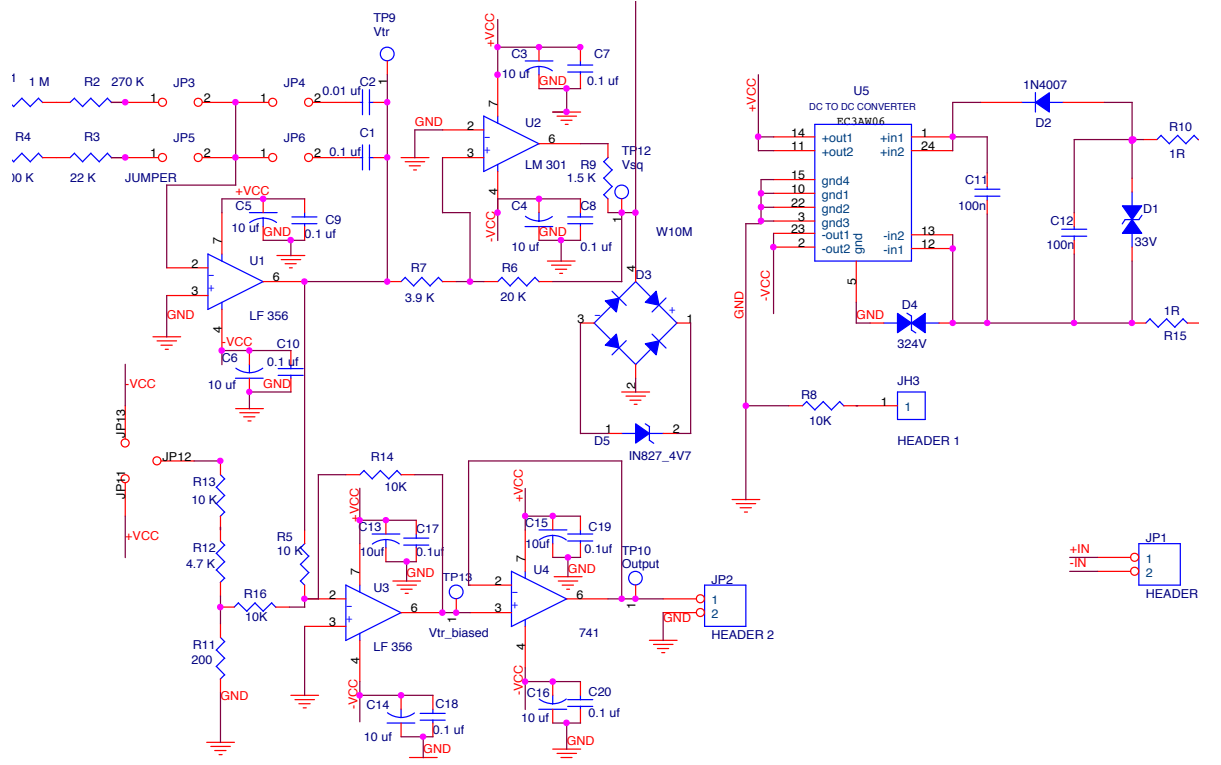
Figure 4.15: Triangular wave generator circuit. Bias voltage $= \pm 12V$ and output voltage $= \pm 1V$.

The current collected by probe 1 is given by:

$$j_1 = j_{0i1} - j_{oe1} exp \left(\frac{e(V_1 + V_f - V_s)}{k_B T_e} \right) \tag{4.3}$$

By the definition of floating potential:

$$j_{oe} exp \left(\frac{e(V_f - V_s)}{k_B T_e} \right) = j_{0i} \tag{4.4}$$

equation 4.3 becomes

$$j_1 = j_{0i1} \left(1 - exp \left(\frac{eV_1}{k_B T_e} \right) \right) \tag{4.5}$$
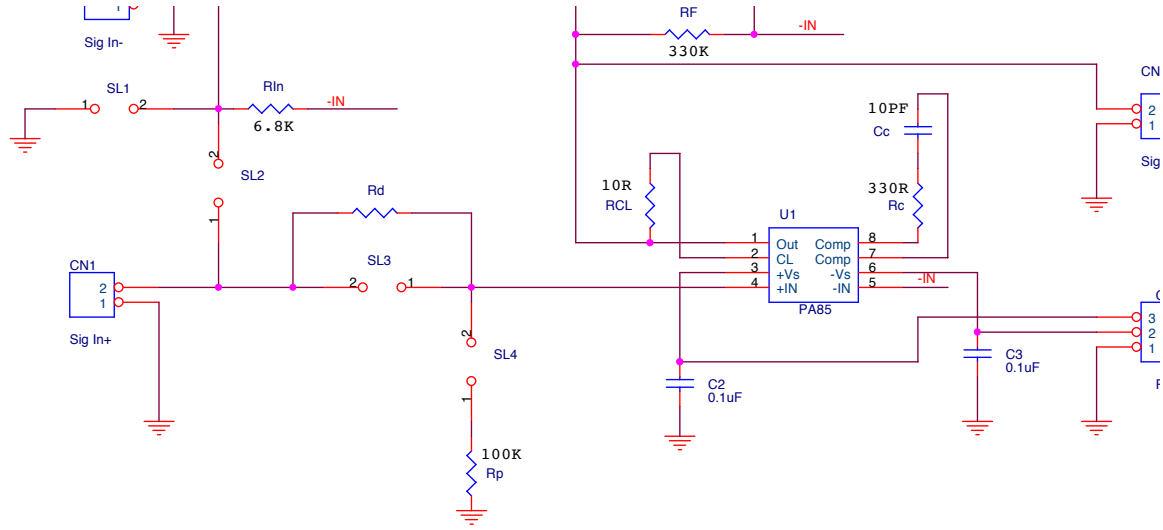
Figure 4.16: Circuit used for the amplification of the sweep voltage signal. Gain of the non-inverting amplifier ~ 51.

Similarly, we have for probe 2,

$$j_2 = j_{0i2}\left(1 - exp\left(\frac{eV_2}{k_B T_e}\right)\right) \tag{4.6}$$

If the two probe tips are identical, $j_{0i1} = j_{0i2} = j_{0i}$; and since the net current drawn by the probe is zero, we have:

$$j = j_1 = -j_2 \tag{4.7}$$

Using the equations 4.5, 4.6 and 4.7, we get

$$\frac{j - j_{0i}}{-j - j_{0i}} = exp\left(\frac{eV_b}{k_B T_e}\right) \tag{4.8}$$
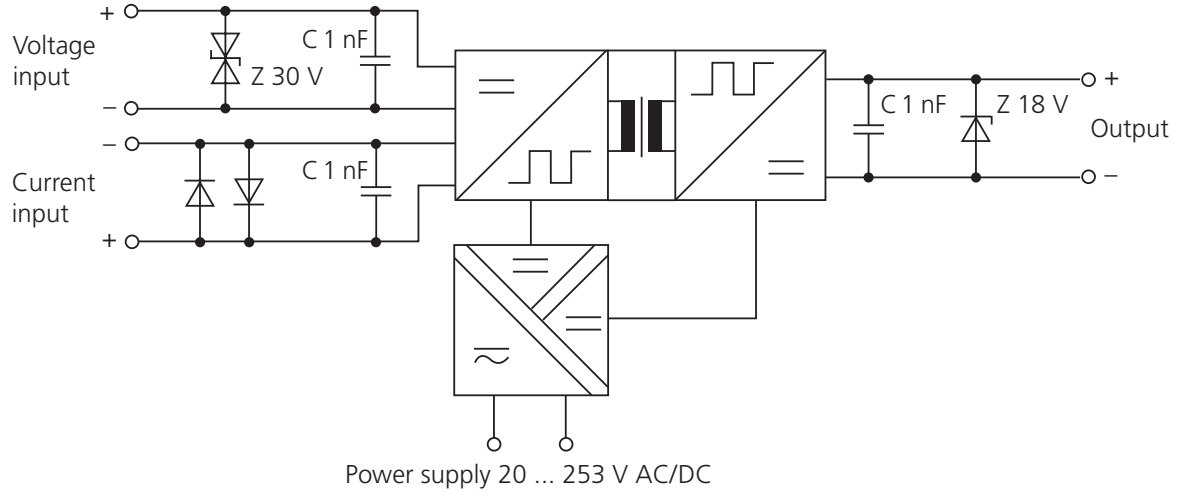
Figure 4.17: Circuit used for the amplification of the sweep voltage signal. Gain of the non-inverting amplifier ~ 51.

where, $V_b = V_1 - V_2$ is the double probe potential. Solving for j

$$j = -j_{0i} tanh \left(\frac{eV_b}{2k_B T_e} \right) \tag{4.9}$$

On differentiating equation 4.9 with respect to V_b at $V_b = 0$

$$\frac{dj}{dV_b}|_{V_b=0} = -j_{0i} sech^2 \left(\frac{eV_b}{2k_B T_e} \right) |_{V_b=0} \left(\frac{e}{2k_B T_e} \right) \tag{4.10}$$

electron temperature is given by:

$$T_e = \frac{j_{0i}}{2 \frac{\delta j}{\delta V_b}|_{V_b=0}} \tag{4.11}$$

The maximum current in the double probe circuit is limited by the ion saturation current. The I-V characteristic obtained by varying the bias voltage (V_B) is thus symmetric about the origin as shown in figure 4.19. The electron cur-

73
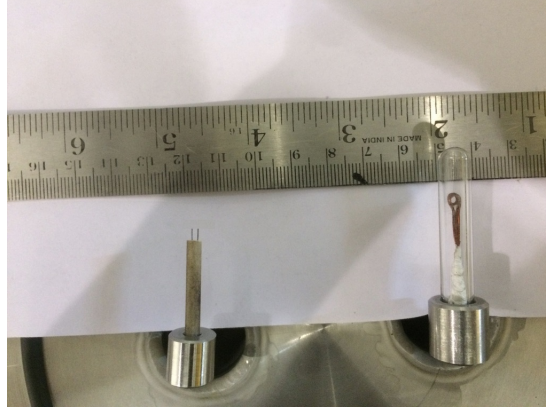
Figure 4.18: Picture of double Langmuir probe and B-dot probe.
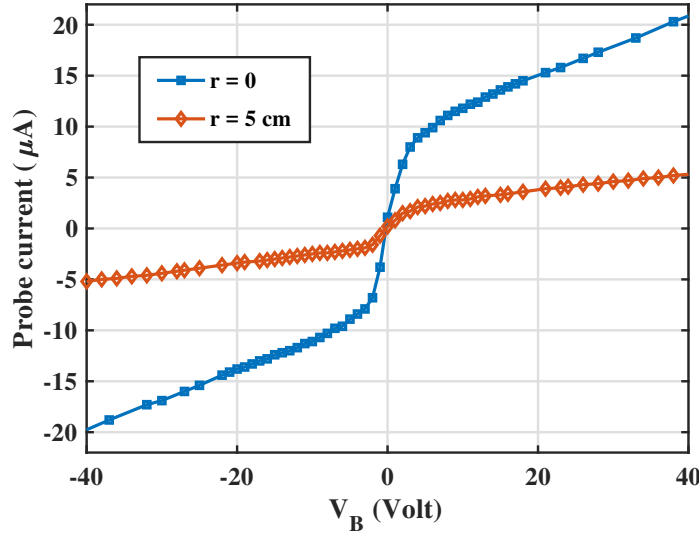
Figure 4.19: Sample data obtained from a double Langmuir probe. The two scans are taken at two different radial locations.

rent comes from the most energetic electrons in the Maxwellian distribution and is a small fraction of total electrons moving toward the probe. The temperature is estimated from the I-V characteristic by computing the slope of the curve at $V_B = 0$.

Figure 4.14 shows the circuit used for obtaining the double probe signal. The circuit is isolated from the ground by using a isolation transformer to power the

circuit and the DC power supplies from mains. A triangular wave generator is used to generate a wave of $\pm 1V$ peak to peak. This is amplified 50 times through a PA-85 power amplifier to $\pm 50V$ peak to peak. This signal is fed into the two probe pins through a 2 kΩ resistance connected to one of the pins. The voltage drop across this resistor is used to obtain the I-V characteristics.

4.3.2 Emissive Probe

The emissive probe is a specialized probe for the measurement of plasma potential. Sheehan [102] has also shown the use of emissive probe in the estimation of electron temperature. But, plasma density cannot be obtained through an emissive probe. The principle behind the use of an emissive probe is to balance out the emission current from the emitting probe with the total current coming to the probe from the plasma. As we know that the ion current is lower than the electron current in a Langmuir probe due to the mass difference, the currents are balanced by making the probe emit electrons which appears as an increase in the ion current in the measured data. In the region where the currents are perfectly balanced the floating potential becomes equal to the plasma potential. This is the principle behind the **floating point technique** of plasma potential estimation through an emissive probe. Langmuir came up with the idea of using a Langmuir probe in the emission region. He concluded that the plasma potential can be found out by balancing the collected current for emitting and non-emitting zones. The biased voltage at which this happens was taken to be the plasma potential. The schematic and emissive probe picture is given in figure 4.20. A tungsten filament of 0.125 mm diameter and 40 mm length is used to construct the probe tip. The exposed part of the filament is $\sim$ 12 mm long. The resistance of the probe is $\sim 1\Omega$.

There are several techniques to obtain the plasma potential using an emissive probe described below.
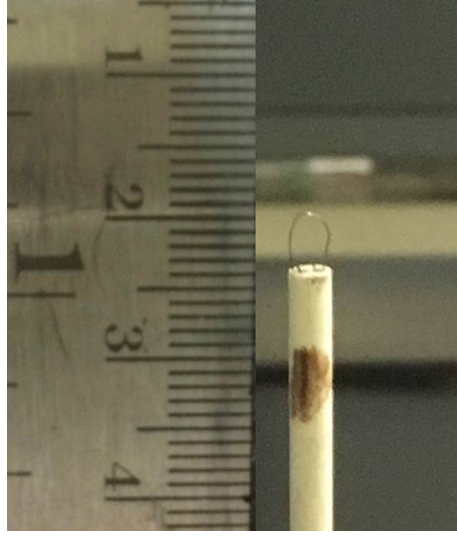
Figure 4.20: Image of the emissive probe.

4.3.2.1 Floating point method

From the assumption that the emission of electrons from the emissive probe balances the net ion and electron current flowing through the probe and hence the brings the probe to a floating state, we can calculate the plasma potential. This type of measurement was shown in detail by Kemp and Sellen [103]. The floating potential of the emissive probe linearly increases with the applied emission current to heat the probe and ultimately saturates. At saturation the floating potential can be taken as the plasma potential with an error of T_e/e in the meaurement [102]. This uncertainty in measurement arises because of the formation of a virtual cathode by the emitted electrons, since not all electrons go into the plasma, creating a region of localized space charge leading to a decrease in the sheath potential and in turn affecting the floating potential value.

The floating point is the simplest technique and widely used where the RF noise is high for the inflection point method 4.3.2.2 to work. We have used the floating point method as well as inflection point method to calculate the plasma potential. The inflection point method is used in the case of Argon plasma where

the saturation of the floating potential with heating current could not obtained.
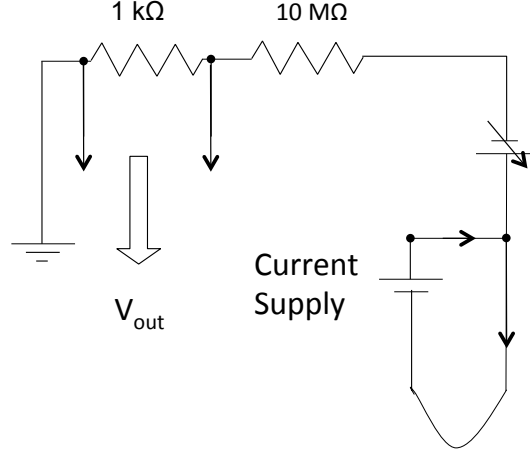
Figure 4.21: Circuit used for obtaining the emissive probe data from the floating point method.

4.3.2.2 Inflection point method

Smith et al. in 1979 [104] demonstrated the inflection point method of interpreting the emissive probe characteristics as an improvement over the floating point method in unmagnetized and weakly magnetized multidipole plasmas. Major limitation of the floating point method is the creation of a space charge region because the probe is operating in the high emission region. To overcome this, the inflection point method was suggested where the emissive probe is operated in the low emission region.

Godyak [105], Sobolewski [106] and Vender [107] have used the value of the plasma potential as the value at the inflection point of the I-V characteristic curve of a cold collecting probe. To calculate the inflection point the first derivative of the probe current with respect to the bias voltage is plotted as a function of V_B and inflection point is identified clearly from the dI/dV_B curve. Sheehan [102] in his review paper on emissive probes stated that the inflection point in the limit of zero emission can be used as the real inflection point and linearly fitting multiple points
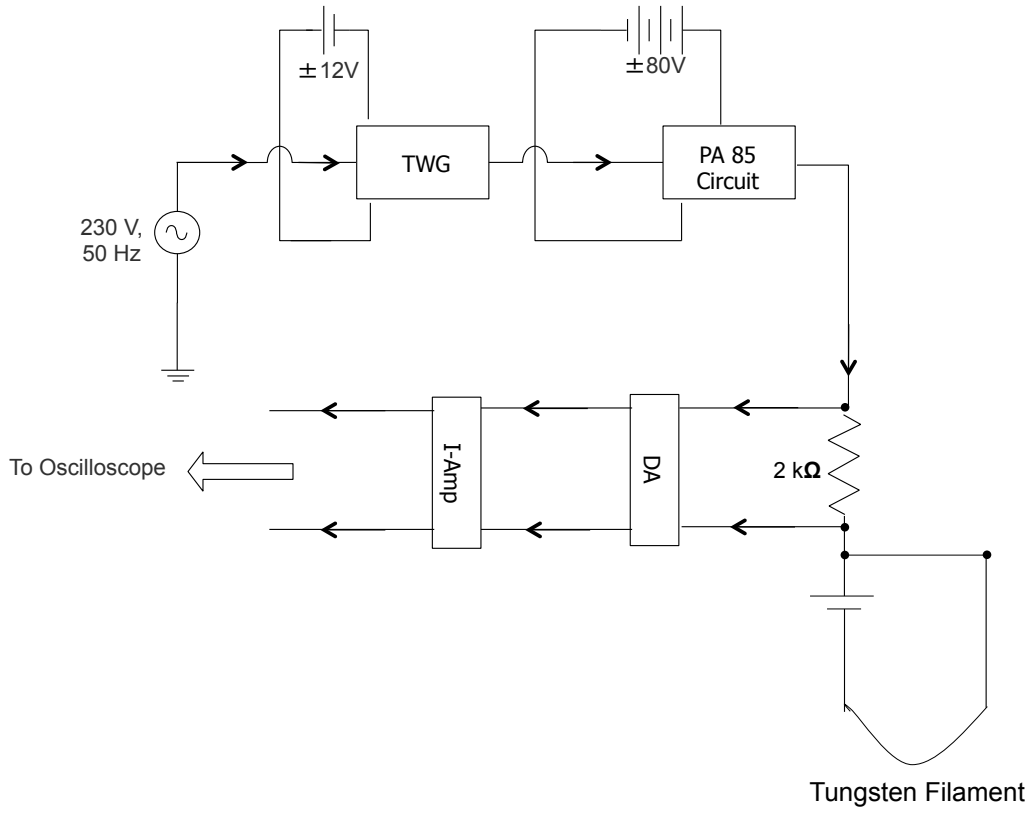
Figure 4.22: Circuit used for obtaining the emissive probe data from the inflexion point method.

reduces the overall uncertainty of the measurement. M. Y. Ye and Takamura [108] theorized a description of the emissive probe I-V characteristic, and concluded that this technique might underestimate the plasma potential by a factor of $T_e/10e$. In the case of an unstable plasma discharge, it becomes difficult to calculate the plasma potential through the inflection point method and many measurements are required for the extrapolation.

In this thesis work, however, the inflection point method is used to measure the plasma potential in Argon Helicon plasma. A typical I-V trace is shown in figure 4.23 along with the dI/dV_B curve to identify the inflection point. The construction of an emissive probe is very similar to a Langmuir probe. In addition
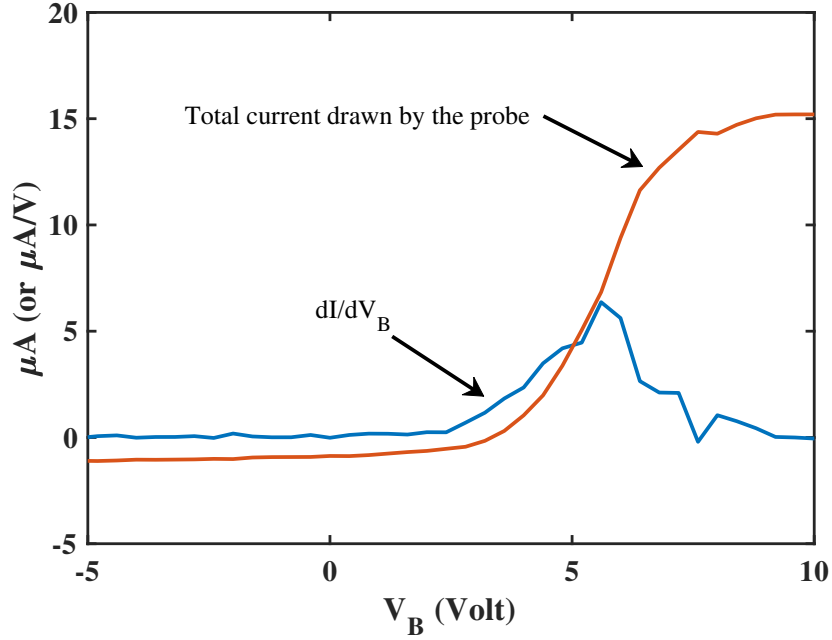
Figure 4.23: Sample trace of the data obtained from the emissive probe showing the plasma potential calculation from the inflexion point method using.

to a Langmuir probe set up we need a separate system to heat the probe to the region of thermionic emission.

There is one more method to estimate the plasma potential by using emissive probes described below. Although, this method has not been used in the present experiment in HELEN.

4.3.2.3   Separation point method

In this method the I-V traces for emitting and non-emitting cases are taken and superimposed on one another. As the bias becomes more negative the two signals would tend to separate. The point of separation is taken to be the plasma potential [102]. The uncertainty in determining precisely where the curves separate is much larger than T_e/e [102], where T_e is the electron temperature. We have not used the separation point method to calculate the plasma potential owing to large

uncertainties associated with the measurements.

4.3.3 Triple Langmuir Probe

Chen and Sekiguchi [109] in 1965, demonstrated the use of a Triple probe for instantaneous measurement of plasma parameters. The ion saturation current and electron temperature can be obtained instantly from the biasing scheme shown in figure 4.24. This figure shows three probe tips P_1, P_2 and P_3 having potential V_1,
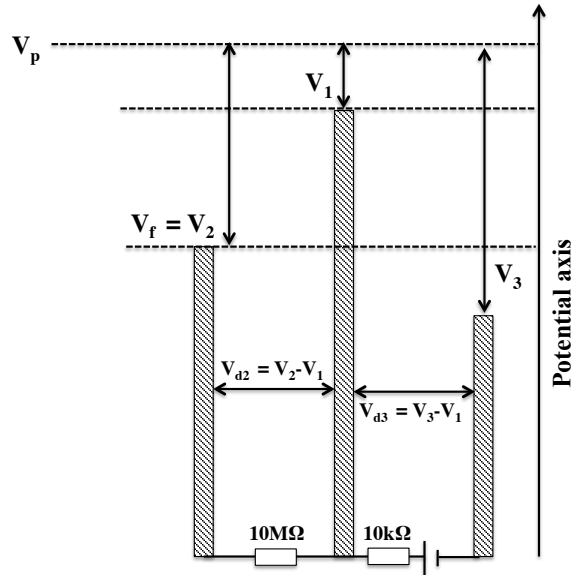
Figure 4.24: Schematic of the triple Langmuir probe pin potential arrangement.

V_2 and V_3. The pins are assumed to be identical. The separation between the probe tips should be large enough such that the sheaths do not interact with each other but at the same time the separation should not exceed the length where the probe pins see different floating potentials in the plasma. For this reason, the separation between the pins was kept ~ 2 mm. Pin 2 is connected to pin 1 through a 10 MΩ resistance to minimize the current drawn by pin 1. Therefore, pin 2 is considered floating. Pin 2 is kept at a lower bias as compared to pin 1, forming a

80

double probe like arrangement. The triple probe system, like the double probe, is floating and no net current is drawn by the probe. Let the current drawn by the three pins be I_1, I_2 and I_3, then:

$$I_1 = I_2 + I_3, \tag{4.12}$$

$$V_2 - V_1 = V_{d2} \tag{4.13a}$$

$$V_3 - V_1 = V_{d3} \tag{4.13b}$$

Assuming the energy distribution of electrons to be Maxwellian, we can write:

$$I_1 = -I_{1e}exp(-V_1/T_e) - I_{1i} \tag{4.14a}$$

$$I_2 = I_{2e}exp(-V_2/T_e) + I_{2i} \tag{4.14b}$$

$$I_3 = I_{3e}exp(-V_3/T_e) + I_{3i} \tag{4.14c}$$

The negative (positive) sign is used for the electron (ion) current. The current through pin 1 and pin 3 should be equal since they are in a double probe arrangement. Taking the ratio of the sum of currents and using this argument along with equation 4.14 we get:

$$\frac{I_1 + I_2}{I_3 + I_1} = \frac{-\left(I_{1e}exp\left(-\frac{V_1}{T_e}\right) + I_{1i}\right) + \left(I_{2e}exp\left(-\frac{V_2}{T_e}\right) + I_{2i}\right)}{\left(I_{3e}exp\left(-\frac{V_3}{T_e}\right) + I_{3i}\right) - \left(I_{1e}exp\left(-\frac{V_1}{T_e}\right) + I_{1i}\right)} \tag{4.15}$$

Since the probes are identical, we can take the saturation currents drawn by them I_{1e}, I_{2e} and I_{2e} to be equal and also $I_{1i} = I_{1i} = I_{1i}$.

Using these and putting $I_2 = 0$ in equation 4.15 we get:

$$\frac{1 - exp\left(-\frac{V_{d2}}{T_e}\right)}{1 - exp\left(-\frac{V_{d3}}{T_e}\right)} = \frac{1}{2} \tag{4.16}$$

From the definitions of V_{d2} and V_{d3} we can reduce equation 4.16 to find an expression for the electron temperature:

$$T_e = \frac{-V_{d2}}{ln(1/2)} \tag{4.17}$$

Here, we have used the assumption that V_{d3} is large compared to V_{d2}. Therefore, we can measure the ion saturation current and electron temperature simultaneously using this method.

The picture of the triple probe is shown in figure 4.25. The pins are made of 0.4 mm diameter tungsten wire and the exposed part of the pin is 5 mm in length.

Figure 4.25: Picture of triple langmuir probe head.
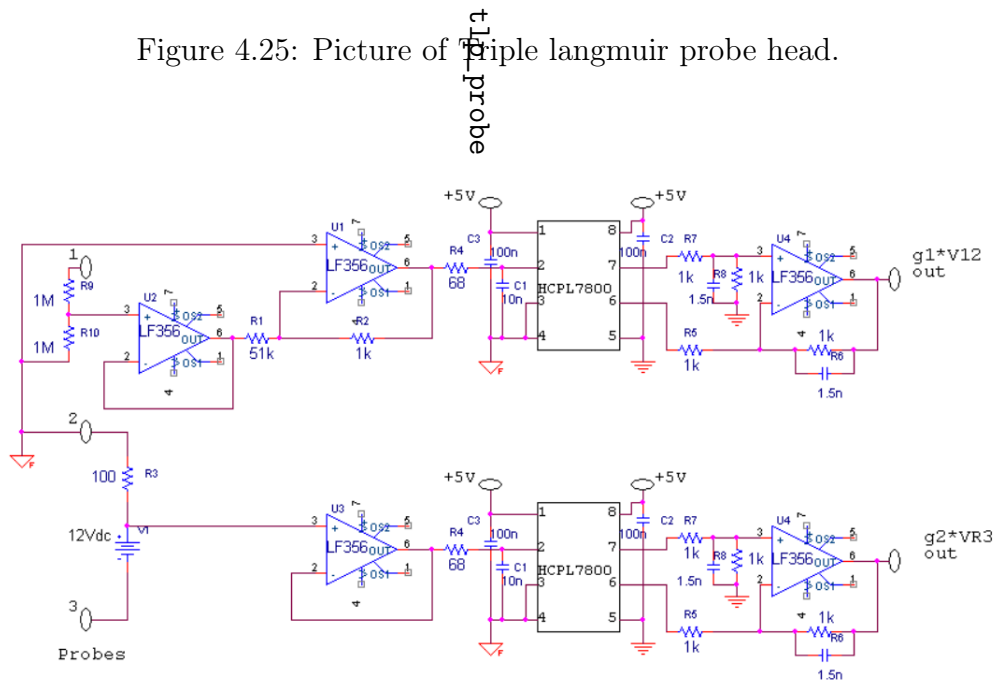
Figure 4.26: Circuit used for the triple Langmuir measurements.

Figure 4.26 shows the triple probe circuit used for obtaining the triple probe signal. The ion saturation current is measured across a 100 Ω resistor and the output is multiplied with gain $g2 = 1$. Whereas, the temperature is measured by the voltage drop across a 1 MΩ resistance and the circuit has a gain , $g1 = 53$.

4.3.4   B-dot Probe

It is essential to carry out the wave field measurements of the helicon wave to validate the excitation of the helicon waves inside the plasma as well as to study wave propagation and damping. The radial profile of the axial wave component, B_z is used to find the azimuthal modes excited in the plasma and to find the perpendicular wave vector, $k_\perp$. Whereas, the axial profile can give the parallel wave propagation vector, $k_\parallel$ as well as the damping length of the helicon wave in the plasma. For all these measurements we need a magnetic probe to detect and measure exclusively the electromagnetic signal of the wave. A B-dot probe, described in detail by Everson et al. (2009) everson is developed for this purpose which works on Faraday's law. Everson et al. had shown a design for 3-D profiling of an electromegnetic wave in the plasma by measuring the r, θ and z components of the wave simultaneously through 3 coils arranged orthogonal to each another. Here, we have used one coil to measure wave signal in a single direction at a time. We focus mainly on the B_z component because the axial and radial profiles of B_z can give a lot of information about the wave such as the perpendicular and parallel wavelengths, damping length and nature of wave in the cavity (standing or propagating). A L-shaped magnetic probe is fabricated to measure the wave fields. The picture of the probe is shown in figure 4.27 alongside an L-shaped double probe mounted on the bottom flange of the HELEN-1 set-up. The axis of rotation is 34 mm away from the centre to enable the radial scanning of the plasma by rotating the probe. The probe is place such the the centre of the loop is at $r = 0$ position. The probe is made of an enamelled copper wire of 0.5 mm

diameter. The probe head consists of 2 turns formed by a twisted pair of copper wire. This essentially creates a total of 4 turns or a differential pair of 2 turn loops 2 mm in diameter. Small loop diameter is desirable for a good resolution. But, smaller loop size decreases the sensitivity of the probe which is dictated by the cross-sectional area of the loop. The voltages induced by the electromagnetic wave in the two loops are equal and opposite.

The induced electrostatic signal in the two probes will be cancelled out due to having the same polarity, while the electromagnetic signal is doubled. The probe head is cased in a glass tube sealed at one end with its open end fixed in an SS socket at the point of the bend in the L-shaped probe. After the loop, the part of twisted pair of copper wires which is covered by an insulator (glass), is prone to stray electromagnetic pick-up. Therefore, the loops are covered with an aluminium foil to avoid any kind of stray electrostatic or electromagnetic pick up.
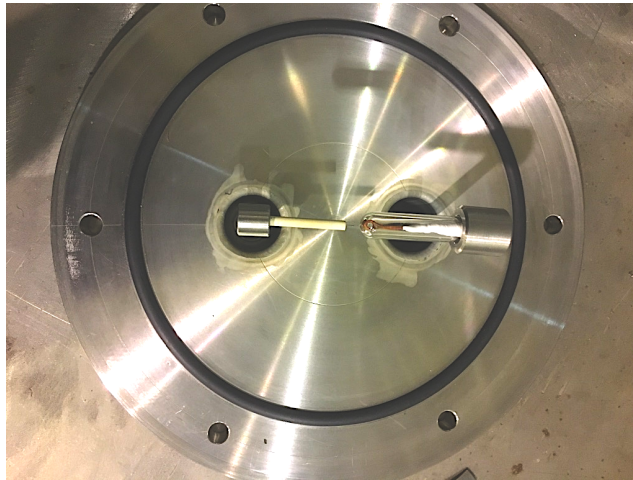
Figure 4.27: Image of the B-dot probe constructed with enamelled copper wire of diameter 0.5 mm.

Figure 4.29 shows the calibration set-up for the B-dot probe. The probe had to be calibrated with a 13.56 MHz signal. It is difficult to give a current of sufficient amplitude at 13.56 MHz using a function generator into a Helmholtz coil, which was initially constructed but later discarded, for the calibration. Instead, a 19-turn
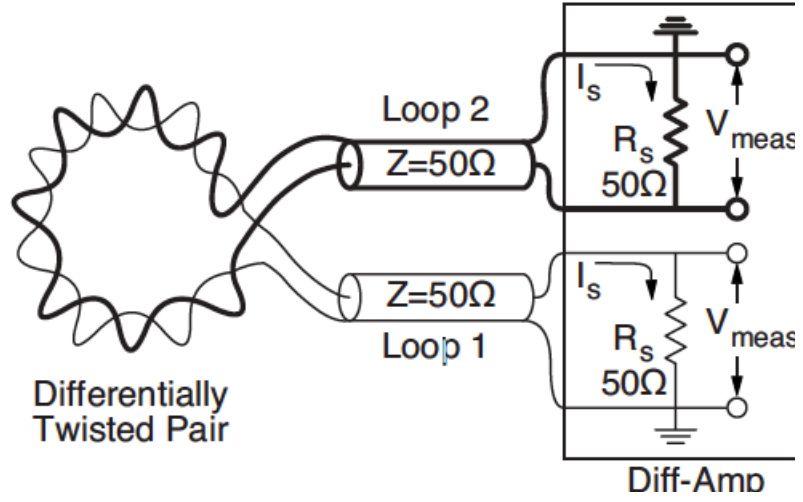
Figure 4.28: Circuit used to obtain the B-dot probe signal. Source: [10]
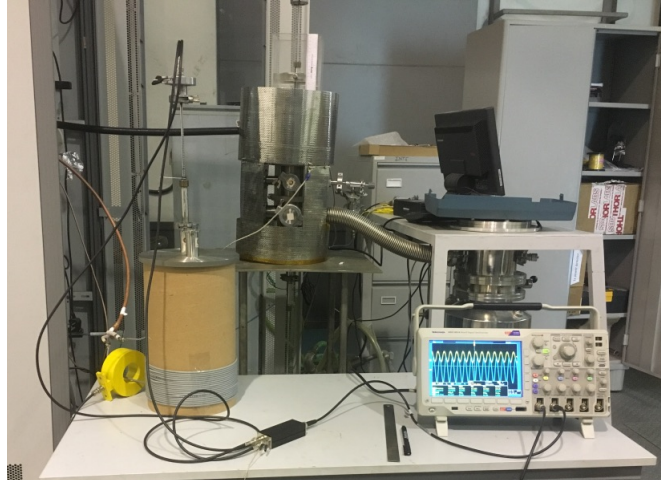
Figure 4.29: Calibration set-up of the B-dot probe at 13.56 MHz.

solenoid wound on a hollow insulator of inner diameter 200 mm is used as shown in the figure. A small power is supplied to the solenoid by the RF Generator of 13.56 MHz and is kept fixed for one axial scan. The current through the solenoid is monitored by a Pearson current transformer. The probe is introduced from the top and moved axially to obtain axial scans at different current values (power values). These signals are used to calibrate the probe by the description given in [10]. The calibration theory given by Everson et al. [10] is used to calibrate
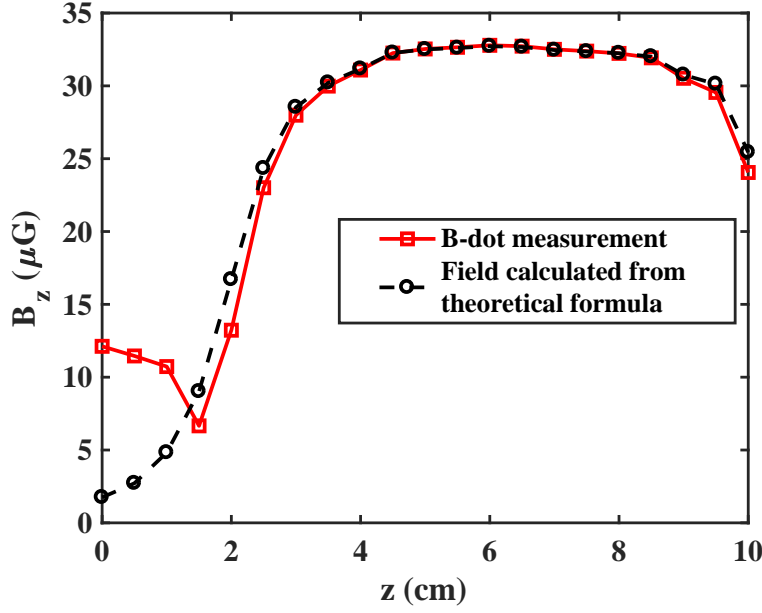
Figure 4.30: Calibration of the B-dot probe at 13.56 MHz.

the B-dot probe using the solenoid set-up. The equivalent circuit is given in figure 4.28. The current through both the loops is assumed to be equal. We can write:

$$
NA\frac{dB(t)}{dt} = \left(1 + \frac{r}{R_l}\right) V_o(t) + \left(\frac{L_s + M}{R_l} + rC_l\right)\frac{dV_o(t)}{dt} \\
+ (L_l + M)\, C_l \frac{d^2V_0(t)}{dt^2}
\tag{4.18}
$$

where, $B(t)$ is the source electromagnetic signal responsible for generating a voltage output through the circuit, V_o, N is the number of turns, A is the loop area, r is the internal resistance of the loop, R_l is the load resistance, L_l is the self inductance of the loop, M is the mutual inductance between two loops and C_l is the internal capacitance of the loop. By taking the Fourier transform of equation 4.18 we get;

$$
\frac{V_o(\omega)}{B(\omega)} = NA\frac{\omega^2\left(\tau_l + rC_l\right) + i\omega\left[(1 + \frac{r}{R_l}) - R_l\tau_l C_l\omega^2\right]}{\left[(1 + \frac{r}{R_l}) - R_l\tau_l C_l\omega^2\right]^2 + \omega^2(\tau_l + rC_l)^2}
\tag{4.19}
$$

86

where, $\tau_l = (L_l + M)/R_l$. It can be seen from equation 4.19 that V_o goes to zero at very large values of ω. Under the assumption that the internal resistance of the loop is very small as compared with the load resistance on the loop and $\omega C_l R_l << 1$, equation 4.19 becomes:

$$\frac{V_o(\omega)}{B(\omega)} = NA\frac{\omega(\omega\tau_l + i)}{1 + (\omega\tau_l)^2} \tag{4.20}$$

Thus we have to find out the value of the calibration factor, which is the term in the right hand side of equation 4.19. The solenoid calibration setup is used for that purpose. The approximate value of the field at the axis of a finite solenoid is given by the relation:

$$B_s(x,t) = \frac{\mu N I_s(t)}{2}\left[\frac{x - L_1}{[(x - L_1)^2 + R^2)]^{1/2}} - \frac{(x - L_2)}{[(x - L_2)^2 + R^2)]^{1/2}}\right] \tag{4.21}$$

We can obtain the value of the field along the axis of the solenoid, $B_s(x,t)$ by equation 4.21 if we know the current flowing through the solenoid. This is experimentally determined using a Pearson current transformer as shown in the figure. Using the solenoid setup for calibration and equation the value of the calibration factor for the present case comes out to be 5.5×10^{-3}. The calibration is shown in figure 4.30, we see a very good agreement between the solenoid field calculated from the relation 4.21 and the probe signal using the value of the calibration factor $= 5.5 \times 10^{-3}$. Once we have calculated the value of the calibration factor using a known $B(t)$ equation 4.19 is used to get the value of $B(\omega)$ using the probe. We obtain V_o as the output from the B-dot probe. It is to be noted that the original voltage induced in one loop is half of V_o.

5

Experiments with Argon plasma

In this chapter, we present the experimental results from the characterization of the helicon wave heated Argon plasma along with the wave field measurements in the HELEN-I device. It is necessary to study a single driver helicon plasma source thoroughly so that eventually a large size negative hydrogen source using multiple helicon drivers could be developed. Here, a parametric study of the Argon plasma is presented as an initial step towards source characterization. The effect of cusp field confinement is demonstrated. Particle balance calculations considering a non-uniform plasma is carried out to estimate the electron temperature theoretically and a power balance model taking into account the particle transport in a magnetised plasma is developed to estimate the equilibrium particle density. The results shown in this chapter have been published in a peer reviewed journal [110].

5.1   Introduction

The negative hydrogen ion source is an essential requirement for building an effective high energy Neutral Beam Injection (NBI) system, which is one of the most efficient system for plasma heating and current drive in tokamaks [11, 42, 111–114].

The advantages of a negative hydrogen ion source over a positive hydrogen ion sources and the production of negative hydrogen ions in a helicon plasma source would be discussed in chapter 7.

The experimental setup and the operational parameters have already been discussed in 4. The experiments are carried out in two stages. In the first stage, the experiments are performed with argon gas. This is essential in order to understand the power coupling to the plasma and benchmarking the helicon wave characteristics considering the relatively more abundant literature available on argon helicon plasmas. The work with hydrogen is carried out in the next stage. The motivation behind this is to demonstrate the utility of the helicon plasma source as an ion source and study the formation of negative hydrogen ions for application in a negative ion source. This chapter contains the results from the first stage. The experiments with hydrogen plasma are discussed in the next two chapters.

5.2   Plasma Characterization

One of the characteristics of helicon plasmas is the dramatic transition from a lower plasma density to a higher density regime when the RF power or the magnetic field is increased beyond a threshold value [6]. The discharge may show single or multiple transitions. Typically, the first density jump corresponds to a transition from capacitively coupled plasma (CCP) to inductively coupled plasma (ICP) and subsequent jump in density is from ICP to wave heated discharge [115]. During the transition, there is a sudden increase in plasma density and a sharp fall in plasma potential. The position of the transition depends on the ratio of the applied magnetic field to the plasma density and therefore, the transition is speculated to be a wavelength related phenomenon form the dispersion relation 5.1 [8]. This jump in density may also directly proceed from the CCP to helicon mode of operation at low magnetic fields. This is due to the dependence of the helicon

wavelength directly on the square root of the axial magnetic field and inversely on the plasma density. This means that for lower applied field, the transition to a helicon wave discharge may occur for lower value of plasma density [8]. The density jumps observed in HELEN-I are shown in Figure 5.1. The case $B = 0G$ corresponds to CCP mode to ICP mode transition and density jump seen in this case is from $10^{17}m^{-3}$ to $10^{18}m^{-3}$. In the presence of magnetic field, the mode transition proceeds directly from CCP to helicon mode and there is $2 - 3$ times enhancement in plasma density as compared to the $B = 0$ (ICP) case, i.e. from $\sim 10^{17}m^{-3}$ to $10^{19}m^{-3}$.
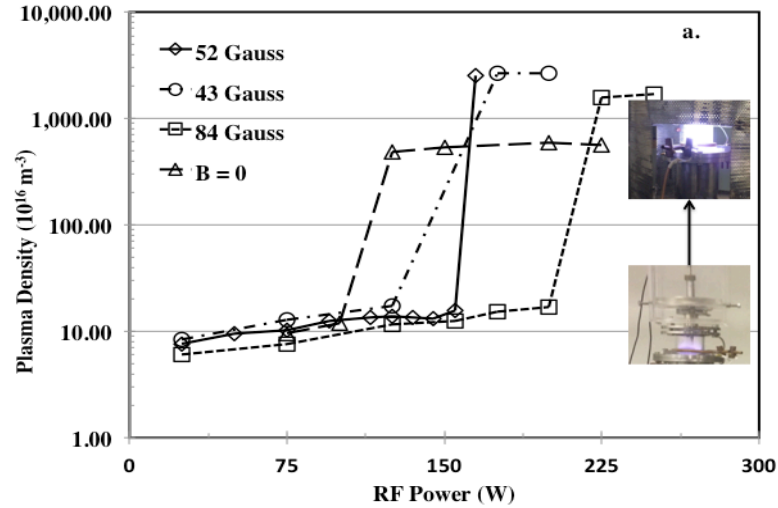
Figure 5.1: Density jump at different axial magnetic field values. The I-V characteristics for the density jump were taken with the probe at $z = 0$ (antenna location) and $P_{Ar} = 30$ mTorr.

The variation of plasma potential with the input RF power is shown in Figure 5.2 for $B = 60G$. With increase in the RF power, the plasma makes a transition to a high density helicon mode. In the helicon mode, the plasma potential drops suddenly and and remains almost constant when the power is increased further. The density jump observed here is similar to the observations reported by Saikat et al. [9] and Franck et al. [116] where the transition is from capacitive to wave
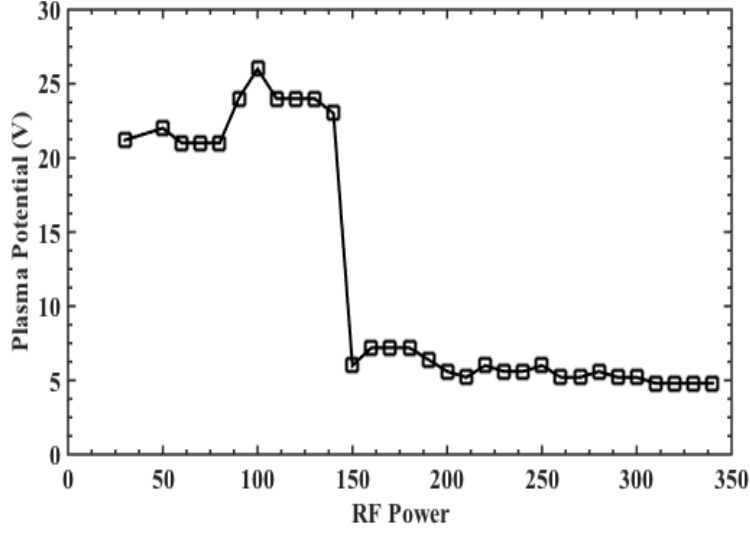
Figure 5.2: Plasma potential variation with RF power shows a sudden drop in potential at $P_{RF} = 150$W indicating a mode transition.

sustained mode. As already stated, this happens at low values of the axial magnetic field [8, 9, 116]. The dispersion relation for a helicon wave with the total wave number α ($\alpha^2 = k_\parallel^2 + k_\perp^2$), [83] is written as

$$\alpha = \frac{\omega}{k_\parallel} \frac{\mu_0 n_0 e}{B_0} \tag{5.1}$$

where, $k_\parallel$ is the axial wave number, $k_\perp$ is the perpendicular wave number, a is the plasma radius, ω is the frequency of the helicon wave, n_0 is the plasma density and B_0 is the applied axial dc magnetic field. Using equation 5.1, $\lambda_\parallel$ as a function of applied field is plotted in figure 5.3. The figure shows that for a lower value of the axial magnetic field the helicon wave would be excited at a lower value of the plasma density for the same $\lambda_\parallel$. Figure 5.4 shows the radial profile of the axial component of the wave field B_z at $z \sim 30$ mm location. The loop antenna excites a $m = 0$ helicon mode as discussed in section 2.4. B_z varies with r as $B_z(r) \propto J_0(k_\perp r)$, where J_0 is the zeroth order Bessel function.

The wave field measurements are done using a B-dot probe. The principle, construction, design and working of a B-dot probe are already discussed in section
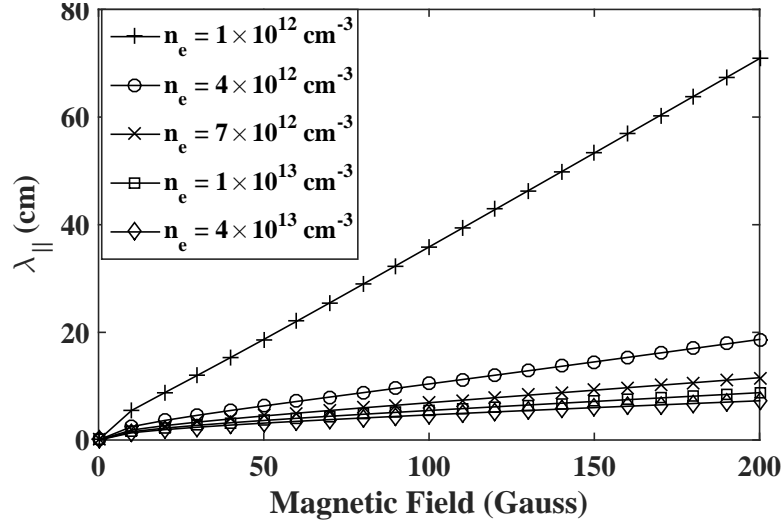
Figure 5.3: $\lambda_\parallel$ obtained from the dispersion relation of the helicon wave is plotted against the axial wavelength for different plasma densities.
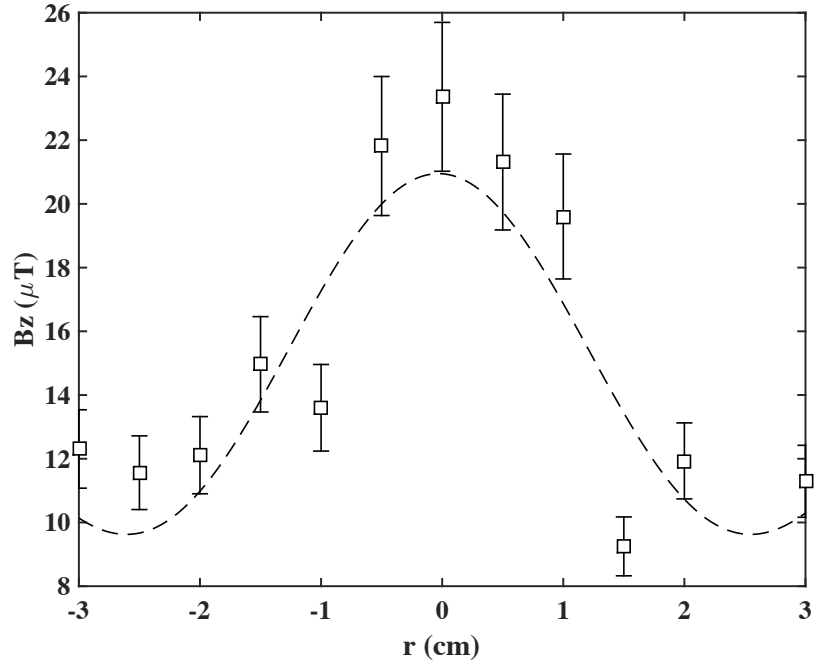
Figure 5.4: B_z radial profile at $z = 30$ mm from the antenna location is shown with the open squares ($\square$) while the dashed curve (–) is the Bessel function fitted on the experimental data at $P_{RF} = 200$ W.

4.3.4. The radial profile of B_z is obtained and plotted in figure 5.4. A Bessel function is fitted on the points to get the value of $k_\perp$. This is repeated at different z locations to get the axial variation of $k_\perp$. The values of $k_\perp$ thus obtained, are given in the table below. The theoretically expected value of $k_\perp$ for a $m = 0$ mode and plasma radius $a = 25mm$ is $1.53m^{-1}$. It is observed that the values of the perpendicular wave vector ($k_\perp$), obtained from fitting the experimental data with a Bessel function, matches with the theoretically expected value for the fundamental mode in the vicinity of the source ($z < 50mm$). But, it deviates from the theoretically expected value as one moves farther away from the source, where the axial dc magnetic field starts diverging and the role of cusp magnetic field geometry becomes important.

Table 5.1: $k_\perp$ variation with z.

z (cm)	$k_\perp (cm^{-1})$
3	1.4865
4	1.5773
5	1.4549
6	3.1309
11	2.2159

Figure 5.5 shows the axial profiles of the plasma density for two different pressure cases, 6 mTorr ($8 \times 10^{-3} mbar$) and 30 mTorr ($4 \times 10^{-2} mbar$). The axial profile of the applied field is also plotted in the same figure. The density peaks just below the antenna and falls steeply below the source chamber. The loop antenna is placed at $z = 0$, which is 40 mm below the metallic top flange. The separation between the mid plane of the permanent magnet and top end plate is kept fixed at ~ 90 mm unless specified. The axial field due to the ring magnet provides a uniform field in the source, but the field lines begin to expand below the source. In the expansion chamber, this diverging field lines (5.5) combined with the cusp magnetic field configuration (4.2.3) together results in a complicated magnetic field

94

boundary close to the periphery of the expansion chamber. The type of boundary affects the wave propagation in the downstream region [18]. This is also evident from the table showing the variation of $k_\perp$ with z, see 5.1.

The radial profiles of the plasma density and applied dc magnetic field inside expansion chamber is shown in figure 5.6 just below the source at $z = 30$ mm with and without the plasma confinement by the linear cusp magnetic field. The double Langmuir probe was kept perpendicular to the axis and was moved radially to scan the plasma. The radial density profile is almost flat at the centre in the case of no cusp confinement. But, with the cusp field the profile is peaked at the centre. While the radial profile of the electron temperature remains almost the same with and without the cusp field as shown in figure 5.7. It is also observed that the plasma density increases considerably with the cusp confinement as shown in the figure 5.6. The enhancement in plasma density can be attributed to the reduction in the loss area in the presence of cusps field. The loss area is calculated in terms of the leak width from the cusps. In the present case, the leak width, w is given by [117]:

$$w = \frac{2d}{\pi} \left[\frac{r_{ce} r_{ci}}{\lambda_{me} \lambda_{mi}} \right]^{1/2} \tag{5.2}$$

here r_{ce} is the the mean electron Larmor radius and r_{ci} the mean ion Larmor radius at the point where the magnetic field lines of the cusp field are entering the wall. A simple calculation can predict the reduction in loss area. For the experimental conditions of figure 5.6 (pressure = 30 mTorr, magnetic field at the point where the field lines are entering the wall = 500 G), the parameters r_{ce} and r_{ci} are $9.5 \times 10^{-5} m$ and $5.8 \times 10^{-3} m$ respectively. The mean free paths for electron, $\lambda_{me} = 0.27 m$ and ion $\lambda_{mi} = 0.05 m$. Using these values, the leak width, w comes out to be $2.1 \times 10^{-4} m$, which corresponds to a loss area of $5.04 \times 10^{-4} m^2$ for a 0.3 m long expansion chamber. The ratio of loss area without and with the confinement

is ~ 187. This clearly shows that we can expect an enhancement of two orders in density with the cusp confinement. Figure 4.8 shows the cusp field configuration in the expansion chamber. The field free region has a radius of ~ 26 mm.
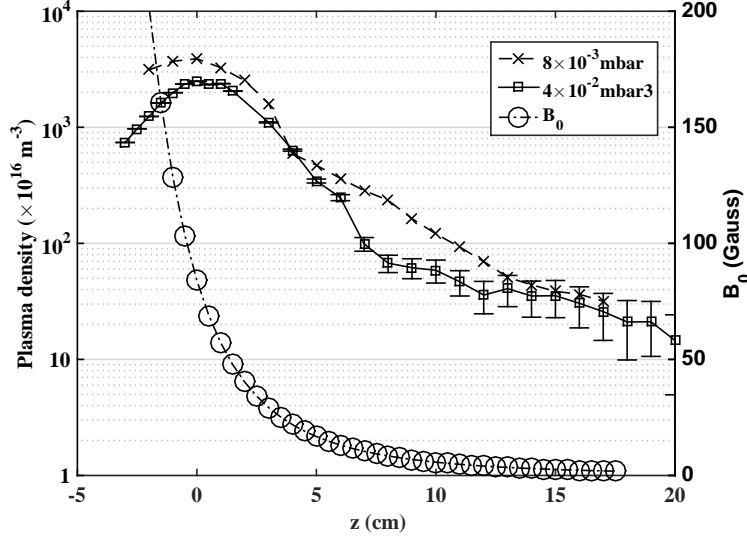
Figure 5.5: Axial profile of the plasma density in the vessel along with the magnetic field at the corresponding axial locations due to the ring magnet. The open circles (o) represent the dc magnetic field values shown on the right hand side scale. The centre of loop antenna is at $z = 0$.

Figure 5.8 shows the axial profile of the electron temperature T_e. Maximum T_e inside the source chamber reaches 4 eV just below the antenna and falls to nearly 2 eV as we move away from antenna on both sides. The diagnostic ports in the expansion chamber are located at $z \sim 120$ mm to $z \sim 150$ and the cusp confinement field is absent at that location. It is seen that the temperature increases at $z \sim 150$ mm (figure 5.8), which is due to loss of confinement to maintain the pressure balance. The dependence of T_e measurement on pressure could not be assessed accurately because of the high RF noise in the source chamber. A dog-legged double Langmuir probe is used to make the measurements in the expansion chamber, where the RF noise is relatively smaller. Since the $m = 0$ helicon mode
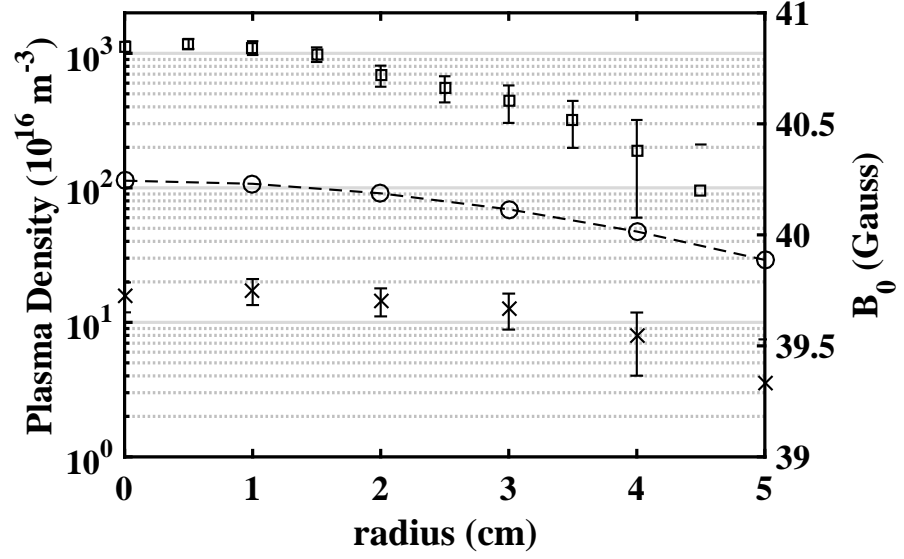
Figure 5.6: Radial profile of the plasma density and the magnetic field of the ring magnet inside expansion chamber, at $z = 30$ mm with ($\square$) and without ($\times$) the confinement cusp field at 30 mTorr and $P_{RF} = 200W$. The open circles (o) correspond to the dc magnetic field values shown on the right hand side scale.
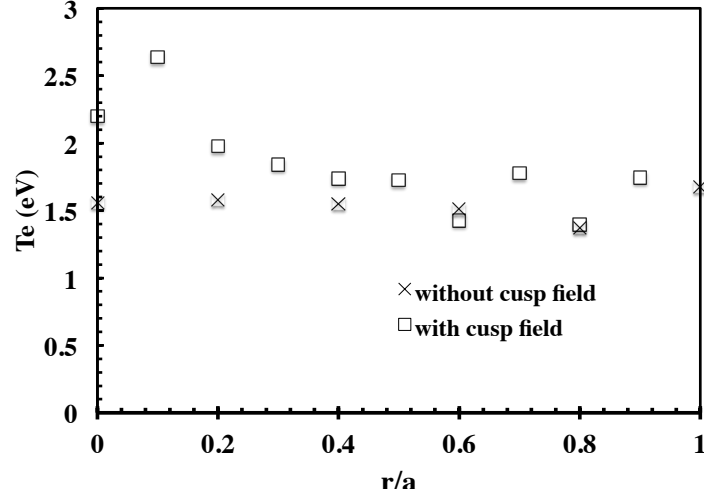
Figure 5.7: Radial profile of the electron temperature with and without the confinement cusp field at $z = 120$ mm and $P_{RF} = 200W$.

is azimuthally symmetric, the L-shape of the probe is used to take the radial scan by the rotating the probe shaft.

To understand the measurements by the double probes for Argon plasma in RF
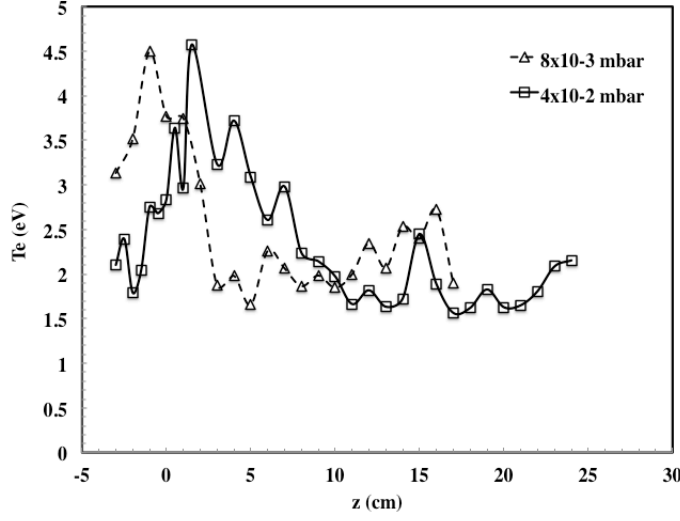
Figure 5.8: Axial profile of the electron temperature for different fill pressures at $r = 0$. Centre of the loop antenna is at $z = 0$, $P_{RF} = 200W$.

environment, measurement results are evaluated through theoretical understanding based on power and particle balance.

5.3 Particle balance and comparison with the experimental result

The particle balance in plasma can be used to estimate the electron temperature and compare the results with the experiments. Universal density profile model given by Curreli and Chen [96] is used for particle balance inside the source chamber. A comparison between the uniform density model given in reference [117] and the universal density model of Curreli [96] is also presented. In the case of universal model, the plasma density peaks at the centre and falls near the sheath edges. Furthermore, for an axial magnetic field equal to 100 G (similar to our experimental conditions) the ion Larmor radius of a 0.1 eV (assumed) Argon ion is around 2.9 cm. So, ions are considered to be unmagnetized and the effect of the

magnetic field on the ion motion is neglected.

5.3.1 Basic Equations

For formulating the particle balance model we consider a cylindrical plasma with the temperature and density varying with r. It is assumed that the plasma is submerged in a uniform axial magnetic field B_0, such that the Argon ions can be considered as unmagnetized. This assumption is justified for an axial magnetic field equal to 100 G (similar to the experimental condition), the ion Larmor radius of a 0.1 eV (assumed) argon ion is $\sim 2.9cm$, which is greater than the source radius. The effect of the magnetic field on the ions is thus neglected.

To get the equilibrium condition for the plasma, we begin with the equation of motion for the ions of mass M, plasma density n, neutral density n_n and $T_i << T_e$:

$$M\mathbf{v}\nabla \cdot n\mathbf{v} + Mn\mathbf{v} \cdot \nabla\mathbf{v} - en\mathbf{E} + Mn\nu_{io}\mathbf{v} = en(\mathbf{v} \times \mathbf{B}) - KT_i\nabla n = 0; \qquad (5.3)$$

here, $\nu_{io} = $ charge exchange collision frequency, the $\mathbf{v} \times \mathbf{B}$ term is neglected in the case of ions.

For convenience we define the following terms, which are assumed to be radially varying:

$$Ionization Probability : P_i(r) = \langle\sigma v\rangle_{ion}(r), \qquad (5.4)$$

$$Charge Exchange Probability : P_c(r) = \langle\sigma v\rangle_{cx}(r) = \nu_{io}/n_n \qquad (5.5)$$

The continuity equation can be written as:

$$\nabla \cdot (n\mathbf{v}) = nn_n P_i(r) \qquad (5.6)$$

Putting the values from equations 5.4 and 5.6 in 5.3 we get,

$$M\mathbf{v} \cdot \nabla\mathbf{v} - e\mathbf{E} + Mn_n(P_i + P_c)\mathbf{v} = 0 \qquad (5.7)$$

Taking only the variation in r (as stated in the problem statement above) we can write the radial component of equation 5.7 as

$$v\frac{dv}{dr} = c_s^2\frac{d\eta}{dr} - n_n(P_c + P_i)v. \tag{5.8}$$

where, $E = -\nabla\phi$, $\eta = -e\phi/KT_e$, and $c_s = (KT_e/M)^{(1/2)}$,

and equation 5.6 becomes

$$\frac{dv}{dr} + v\frac{d(lnn)}{dr} + \frac{v}{r} = n_nP_i(r) \tag{5.9}$$

This equation combined with the quasineutrality condition would provide us with a differential equation for particle balance. We therefore, write the equation of motion for the electrons of mass m following Boltzmann's relation and making collisions with neutrals and ions with collision frequencies ν_{eo} and ν_{ei} respectively,

$$mn\mathbf{v}\cdot\nabla\mathbf{v} = -en(\mathbf{E} + \mathbf{v}\times\mathbf{B}) - KT_e\nabla n - mn\mathbf{v}(\nu_{eo} + \nu ei) \tag{5.10}$$

For electrons we can write:

$$n = n_0e^{e\phi/KT_e} = n_0e^{-\eta} \tag{5.11}$$

The justification of this assumption is described in [96]. Next, we take the derivative of equation 5.9

$$\frac{d(lnn)}{dr} = -\frac{d\eta}{dr} \tag{5.12}$$

and use this in equation 5.9 to get

$$\frac{dv}{dr} - v\frac{d\eta}{dr} + \frac{v}{r} = n_nP_i(r) \tag{5.13}$$

and from equation 5.8 we have

$$\frac{d\eta}{dr} = \frac{1}{c_s^2}\left[v\frac{dv}{dr} + n_n(P_i + P_c)v\right]. \tag{5.14}$$

using this in equation 5.13

$$\frac{dv}{dr} + \frac{v}{r} - \frac{v^2}{c_s^2}\left[\frac{dv}{dr} + n_n(P_i + P_c)\right] = n_n P_i(r) \tag{5.15}$$

Let $u = v/c_s$ and rearranging equation 5.15 we finally arrive at our desired differential equation:

$$\frac{du}{dr} = \frac{1}{1 - u^2}\left[-\frac{u}{r} + \frac{n_n}{c_s}P_i(r)\left(1 + u^2(1 + P_c + P_i)\right)\right] \tag{5.16}$$

here, u is the velocity of the particle normalized with respect to the ion acoustic speed c_s. Equation 5.16 diverges when $v \to c_s$. This is the Bohm's criterion and should be satisfied at the sheath ($r \to a$). So, equation 5.16 is solved for different T_e values and results are compared for different r values to check where does the solution for u diverge. The value of T_e for which the solution diverges at $r \to a$ is the actual plasma temperature. Figure 5.9 shows the plot of u varying with radial distance r. The calculation data corresponding to $T_e \sim 2eV$ at 30 mTorr pressure, diverges at $r = 2.5$ cm, which is the value of a for our experiment. The exact value of the plasma temperature comes out to be 1.98 eV. The experimental results shown in figure 5.8, has values ranging from 2eV to 4eV.

The value of T_e obtained through the uniform density model comes out to be $\sim$ 2.6eV, as shown in figure 5.11. Through the ionization and particle loss balance the ionization rate constant K_{iz} is calculated (equation 5.17). To satisfy particle balance condition, plasma loss and plasma formation need to be equal, which means:

$$n_0 c_s A_{eff} = K_{iz} n_g n_0 \pi R^2 l, \tag{5.17}$$
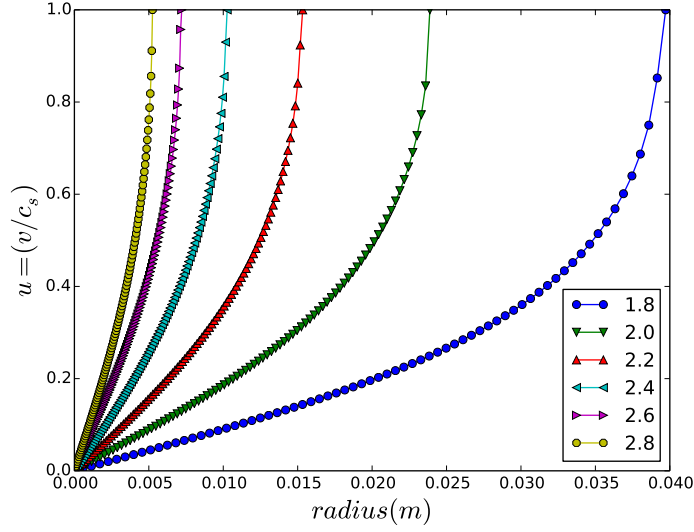
Figure 5.9: Solution of equation 5.16 is plotted against plasma radius for different electron temperatures given in the inset. The ratio v/c_s is 1 at the plasma boundary.

where,

$$A_{eff} = 2\pi R^2 h_l + 2\pi Rl h_R \tag{5.18}$$

is the effective area for particle loss. The term h_l is the ratio of the axial sheath edge density to the bulk plasma density and h_R is the ratio of the radial sheath edge density to the bulk plasma density. In the Helicon mode, the axial power deposition profile is modified as shown in figure 5.10, obtained from the code HELIC [94].

By computing the ionization rate constants for Argon through particle balance and using the equation given by Philip 5.19 [118], plasma temperature T_e is estimated from the intersection point of the two curves.

Philip's equation [118] is valid in the range $1eV << T_e << 7eV$ and is written as,

$$K_{iz} = 2.34 \times 10^{-14} T_e^{0.59} exp(-17.44/T_e) \tag{5.19}$$

The presence of an axial magnetic field in the chamber modifies the power absorption profile. The power absorption does not remain localized near the antenna

102
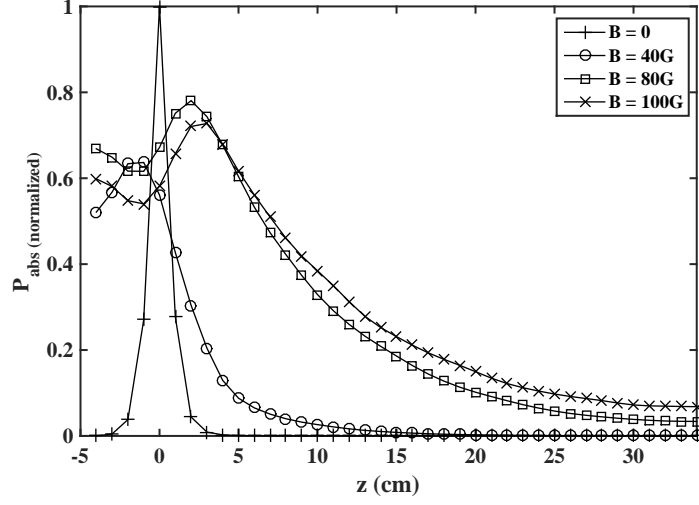
Figure 5.10: Axial variation of power deposition in the plasma obtained from HELIC. Antenna is at $z = 0$.

and is spread across the volume when an axial field is present as shown in figure 5.10. Therefore, to calculate the plasma resistance (R_p) the whole plasma volume should be taken into account. This is done through HELIC, which computes the average R_p for the whole plasma volume. This value of R_p is used in the power balance calculation shown in the next section. It should be noted that the simulation gives the profile (in fig. 5.10) for an axially uniform field, without considering the influence of radial cusp field geometry.

For the present experiment we take $l = 380$ mm, and h_l and h_R come out to be 0.124 and 0.236 respectively. The 1st term in equation 5.18 corresponds to the effective axial loss area on the surfaces of both the endplates and 2nd term is the effective radial loss area on cylindrical surface.

$$h_R = \frac{n_{sR}}{n_0} \sim 0.80 \left(4 + \frac{R}{\lambda_i} \right)^{-\frac{1}{2}} \tag{5.20}$$

From equations 5.17, 5.19 and 5.20, we obtain the K_{iz} as,

$$K_{iz} = \frac{c_s A_{eff}}{n_g \pi R^2 l} \tag{5.21}$$

The cross-over point in figure 5.11 between the two curves gives the plasma temperature. We get nearly same values of T_e with ($T_e = 2.65eV$) and without ($T_e = 2.65eV$) taking into account the axial particle loss. This suggests that the axial losses are not significant in present case from the uniform density model.
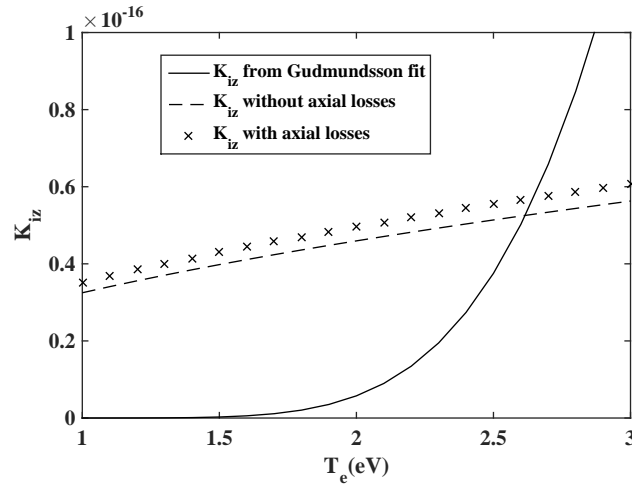
Figure 5.11: Variation of Ionization rate constant, K_{iz} with electron temperature T_e. The intersection of numerically computed K_{iz} and K_{iz} calculated from the particle balance gives the electron temperature.

5.4 Power balance and comparison with the experimental result

The plasma density n_e can be estimated through a power balance calculation using the experimental conditions for HELEN-I. The magnetic field in the device is sufficient to magnetize electrons but the ions remain unmagnetized. The electrons

thus have lower mobility transverse to the field direction. An ambipolar diffusion of particles in the plasma would set up leading to a equilibrium density profile. The ambipolar diffusion coefficient is decided by the ion diffusion across the field, however electrons may be lost axially and short circuit the ambipolar field through the conducting endplate, as suggested by Simon [119]. In the present case, it can be considered that ion temperature T_i is much smaller than that of electron temperature ($T_i << T_e$) and ambipolar diffusion coefficient in perpendicular and parallel directions have to be considered separately,

$$D_{\perp a} = \frac{\mu_i D_{\perp e} + \mu_e D_{\perp i}}{\mu_i + \mu_e} \tag{5.22}$$

$$D_{\parallel a} = \frac{\mu_i D_e + \mu_e D_i}{\mu_i + \mu_e} \tag{5.23}$$

$$D_{\perp i} = \frac{D_i}{1 + \left(\frac{\omega_{ci}}{\nu}\right)^2} \tag{5.24}$$

$$D_{\perp e} = \frac{D_e}{1 + \left(\frac{\omega_{ce}}{\nu}\right)^2} \tag{5.25}$$

where, ω_{ci} and ω_{ce} are the ion and electron cyclotron frequencies respectively. $D_{\perp i}$ and $D_{\perp e}$ are the modified perpendicular diffusion coefficients for ions and electrons respectively in the presence of magnetic field. The electron temperature is taken to be $2eV$ from figure 5.9. The parameter, ν is the total collision frequency which includes the charge exchange (σ_{cx}), electron ion (σ_{ei}) and ionization collisions ($\langle\sigma v\rangle_{ion}$). The corresponding cross sections for the calculation of these frequencies are taken from Curreli [96] and Lieberman [117],

$$\sigma_{cx}(cm^2) = 6.3 \times 10^{-14}(A/T_i(eV))^{0.14}\phi_{ion}^{-1.07} \tag{5.26}$$

A is the atomic mass ($A = 40$ for Argon) and the parameter, $\phi_{ion} = 15.76eV$, is the 1st ionization potential.

$$\langle \sigma v \rangle_{ion} = exp\left(-15.8 - \left(\frac{17.7}{T_e^{0.91}}\right)\right) cm^3/s \qquad (5.27)$$

and an average value of electron-ion collision cross-section is considered for the experimentally obtained densities:

$$\sigma_{ei} = 4 \times 10^{-16} cm^2 \qquad (5.28)$$

The ion flux loss to the walls is changed in the presence of an axial magnetic field. The power loss gets modified because of this. The power lost to the walls is given by,

$$P_{loss} = A_{loss}\Gamma_W W_T \qquad (5.29)$$

where, A_{loss} is the effective area for energy loss, Γ_W is the particle flux to the walls and W_T is the total energy carried away by the particles to the walls [117].

$$W_T = E_c + W_e + W_i \qquad (5.30)$$

$W_e = 2T_e$ and $W_i = 5.9T_e$ for Argon is considered in the calculation [117], which correspond to energy carried away by electrons and ions respectively. The parameter, E_c is the energy required for the creation of an electron ion pair of Argon, it includes all the losses involved in the ionization process and is given by Vahedi [120],

$$E_c = 23 \times exp\left[3.68/T^{1.61}(eV)\right] \qquad (5.31)$$

To estimate the ion flux towards wall, Fick's law gives:

$$\Gamma_W = -D\nabla n \qquad (5.32)$$

To get the expression for the power loss, equation 5.32 is used in equation 5.29. Ions carry most of the momentum and thus the momentum loss is attributed to the loss of ions to the walls. Moreover, the magnetic field is such that the ions remain unmagnetized and are able to move across the field. For this reason the radial power loss is more significant than the axial loss which can therefore be neglected [121]. A parabolic radial density profile is considered, like the one shown in figure 5.6 for the present case and can be written as:

$$n(r) = n_0 \left(1 - \left(\frac{r}{a} \right)^2 \right) + n_s; \tag{5.33}$$

where, $n_0 = 4 \times 10^{19} m^{-3}$ and the density close to the sheath $n_s = 4 \times 10^{18} m^{-3}$. P_{Loss} is the sum of the power lost to the walls and the power utilised in plasma creation. This is calculated using the relations given above and is subsequently used to calculate plasma resistance and plasma density.
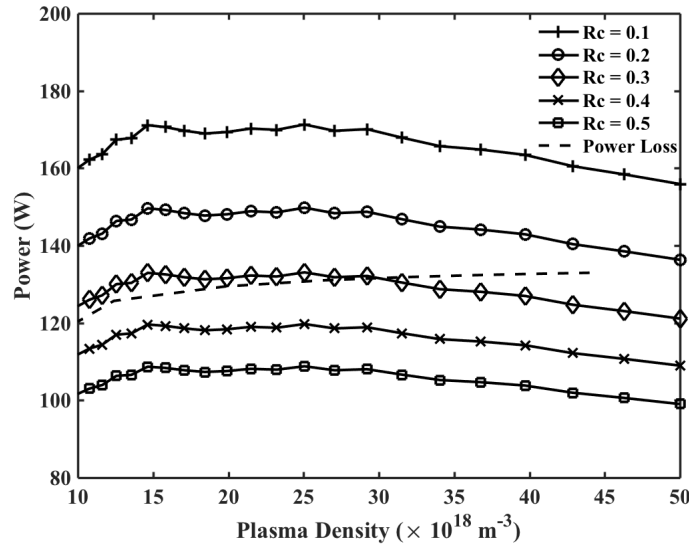
Figure 5.12: Power absorption for different R_c values and Power loss is plotted against plasma density for $P_{RF} = 200$W. The intersection point of power absorbed and power lost will give the equilibrium plasma density of the discharge.

The amount of power absorbed is calculated using HELIC [94] code, based on

equivalent electrical circuit containing two resistances in series as already discussed in section 3.3 [13]. The resistances represent the plasma resistance (R_P) and total loss resistance (R_c). The power absorbed plasma the plasma is given by:

$$P_{abs} = P_{RF} \frac{R_P}{R_P + R_c} \tag{5.34}$$

where R_c is same circuit loss resistance as used in section 3.3 and is an indicator of the efficiency of the device. High R_c would mean low efficiency. Figure 5.12 shows P_{abs} curves plotted for different values of R_c at 80 G axial magnetic field alongside the P_{Loss} curve. The point where these curves meet is the equilibrium point where the net input power is balanced by the net power used. The curve containing the intersection point matching with the experimental density value is taken to be curve representing the R_c for the experiment. Once, we have the value of R_c, the value of the plasma resistance can be computed.
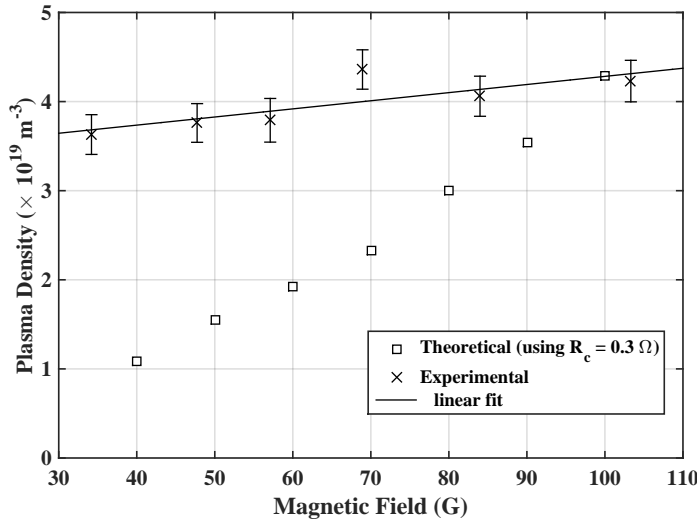
Figure 5.13: Comparison of plasma density (Theory vs. Experiment) for different local axial magnetic field values.

Using the plasma density in the central part of the source chamber (figure 5.6), the R_c value for the present case lies near 0.3Ω from figure 5.12. Using this R_c, the

P_{Loss} for different magnetic field values are calculated. This is used to calculate the equilibrium densities shown in figure 5.13.

5.5   Summary and conclusion

The experimental results using the Argon gas show that a $m = 0$ azimuthal mode is excited in the Argon plasma using a 13.56 MHz RF power source and a loop antenna. The Bessel function dependence of the radial profile of wave B_z along with the clear transition in plasma density from a low density to a high density mode and sudden drop in V_P are typical signatures of the helicon plasma and they verify the presence of $m = 0$ helicon mode in the present experiment. High plasma densities reaching $10^{13} cm^{-3}$ values are obtained in the Argon plasma at 30 mTorr (0.04 mbar) pressure. The effect of cusp confinement of the plasma is also observed in the expansion chamber. The density increases by two orders in the presence of the cusp field, which is consistent with the theoretical estimation of reduction in loss area due to confinement by cusp field and also with the observations of Leung et al [24]. Electron temperature in the source chamber varies from 2 eV to 4 eV and goes down to $\sim$ 1.5 eV in the expansion chamber. Theoretical estimation through the particle balance predict the temperature between 2-3 eV. The power balance calculation gives the plasma resistance to be nearly 1.2 .

6

Experiments with Hydrogen plasma

In this chapter, we focus on the characterization of hydrogen plasma. The development of the negative ion diagnostics in the helicon plasma source to measure H^- ion density is done based on the results of characterization. The negative ion measurements are shown in the next chapter. This chapter discusses the details of the HELEN-I experiment with hydrogen and the results from the measurements. It is shown that in Helicon wave heated plasmas very high plasma densities can be attained with electron temperatures as low as ~ 1 eV in the downstream region. These conditions favour the production of negative hydrogen ions. We have observed that the single loop antenna used in the case of Argon helicon plasma is unable to excite the helicon wave in the hydrogen plasma so a Nagoya III antenna is used in the case of hydrogen. A density rise away from the plasma source in the downstream region is observed which is being investigated. Results from this chapter have been compiled to be published in a peer reviewed journal [122].

6.1 Introduction

Last chapter dealt with the excitation of the helicon wave in the Argon plasma and its characterization using a single loop antenna. We had seen that the helicon mode of operation was achieved by increasing the power, which was verified by the wave field measurements using a B-dot probe. The plasma density and temperature decreases in the expansion region, which is critical for a negative ion source. We had also formulated particle and power balance schemes and had shown that the radial losses are more prominent than the axial losses and gave an approximate value of the plasma resistance in Ar plasma as well. These experiments were crucial to understand the dynamics of the device and to quantify the confinement of electrons by the cusp magnetic field. To obtain a high density of H^- in the device, high density of low temperature electrons are required in the expansion chamber for the dissociative attachment of electrons.

The next step for moving forward in the direction of negative hydrogen ion source development, we excite the helicon wave in a hydrogen plasma and examine the plasma and wave characteristics. There are numerous factors at play when it comes to a generating a stable hydrogen helicon plasma. Hydrogen ions being lighter than the Argon ions are transported to the walls quickly and get lost. This contributes to the power dissipation to the walls. Using higher magnetic field can easily magnetize the ions and prevent their loss to the walls. But, at higher fields two things happen. First, we do not observe the low field peak of the helicon plasma which was also discussed in the last chapter. Second, the input frequency ω is of the order of the Lower hybrid frequency and the short wave, electrostatic component of the dispersion relation is dominant. For helicon wave excitation in a hydrogen plasma the axial field is set to lie between 40 G to 150 G at the antenna location. It is shown that a helicon hydrogen plasma can be created with input RF power, $P_{RF} < 1$kW. After the formation of the helicon plasma the detailed

characterization is carried out.

In this chapter, the characterization of the plasma and wave field measurements are presented. It will be shown that lower pressure operation are favourable and energy efficient. For low axial field present in the expansion region ω approaches ω_{ce} and might lead to electron cyclotron resonance when $\omega = \omega_{ce}$. It is also shown that wave propagation along the surface of a resonance cone is possible for certain magnetic field configurations. This leads to a strong resonant absorption of wave fields at that location resulting in a density rise away from the antenna in the downstream region.

From the point of view of the production of H^- ions, the configuration of the helicon plasma source including the extraction region is important for good negative hydrogen ion (H^-) yield. We will discuss in detail the processes responsible for the negative hydrogen ion production and destruction in the next chapter. Considering all the reactions responsible for H^- ion production and destruction given below, low pressure, high density but low temperature hydrogen plasmas are suitable for an efficient negative hydrogen ion source [41, 76]. The production of negative hydrogen ions is through two processes: (a) Surface process and (b) Volume process. In surface process, energetic H atoms or H^+ ions are converted to H^- ions after hitting the low work function surface.

$$H_0^*/H_n^+ \xrightarrow{Low\,work-function\,surface} H^-.$$
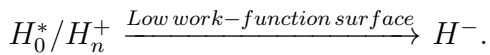
In the volume process, H^- ions are created in the two-step collisional reactions:

1st step: $e_{fast} + H_2 \to H_2^*(\nu"),$ (vibrationally excitation of ground state by energetic electrons).

2nd step: $H_2^*(\nu") + e_{slow} \to H^-,$ (vibrationally excited state form H^- ions through dissociative attachment (DA) process with a low energy electrons).
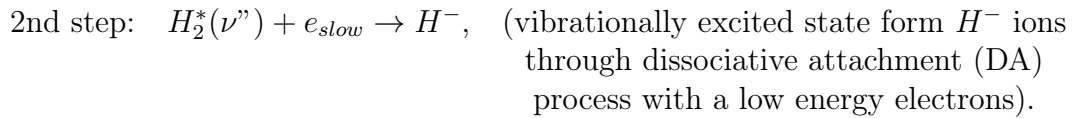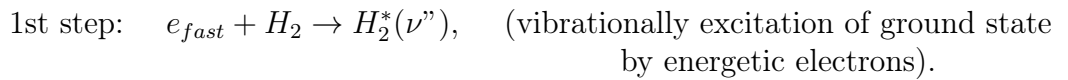
The above discussion indicates that a plasma source having high plasma density and both high as well as low electron temperatures is a suitable candidate for a volume H^- ion source. However, this requires the separation of the plasma into two parts virtually, to sustain different electron temperatures in the same plasma volume. Present permanent ring magnet based helicon source lies in this category. A detailed description of the experimental apparatus is given in chapter 4. The expansion chamber in the HELEN setup has an array of magnets arranged to form a multi cusp field in the chamber. Figure 4.7 shows the diverging magnetic field in the source and expansion chamber, which depends on the distance of the permanent magnet from the plasma source. Figure 4.8 shows the cusp field geometry in the expansion chamber forming a field free region of $\sim 50mm$ diameter. Hydrogen plasma is produced by applying RF power to the Nagoya III antenna, of 36 mm length, at 13.56 MHz to excite $m = \pm 1$ azimuthal helicon mode in the plasma.

6.2   Antenna configuration and mode transition

The typical signature of helicon mode operation is identified as a sudden increase in optical light emission and in ion saturation current drawn by the Langmuir probe. But with hydrogen gas, the characteristic density jump marking the transition to the helicon mode was not observed when a hydrogen plasma was created using a single loop antenna. This is because the single loop antenna is unable to create sufficient induction field inside the plasma [123]. Therefore, some other type of antenna has to be used in place of the loop antenna for helicon wave excitation. Melazzi and Lancelotti. [99] have compared different antennae for helicon wave excitation in the plasma namely, single-loop, Nagoya type-III and the fractional helix antennae. They showed that the antenna current density is not spatially uniform, and that a correlation exists between the plasma parameters and the spatial distribution of the current density. Through this performance characterization

of different antennae they concluded that the single loop works better than the other two type of antenna for low plasma densities, but for higher plasma densities Nagoya type-III is the most efficient. Considering this, field generated by the Nagoya antenna and loop antenna are compared. HELIC code is used to simulate the electric field generated by the loop antenna and the Nagoya antenna for the present geometry and the experimental conditions. Figure 6.2 shows the ion saturation current jumps in hydrogen plasma with a Nagoya antenna and RF power greater than 400W.
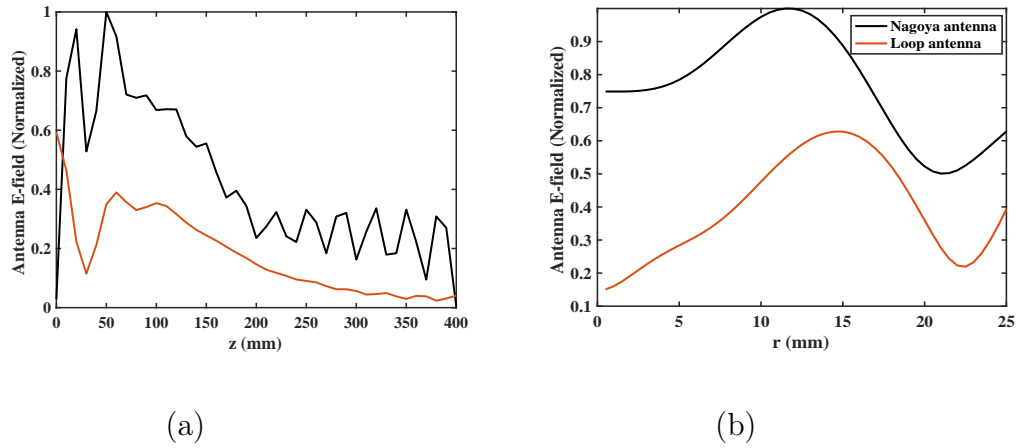
Figure 6.1: Axial (a) and radial (b) component of the total electric field induced in the plasma cavity by loop and Nagoya as simulated by HELIC.

From the simulation results by HELIC, it can be seen that the field induced by the Nagoya antenna is significantly higher than the loop antenna as also stated by Hideki et al. [123] . A Nagoya antenna is chosen for plasma generation based on the HELIC simulations. Figure 6.2 shows the ion saturation current variation with RF power obtained in the two cases. It is observed that in the case of Nagoya antenna there is a jump in ion saturation current at around 400 W whereas, there is no such jump in the case of the loop antenna. At RF power > 400W the antenna is coupled inductively with the plasma.
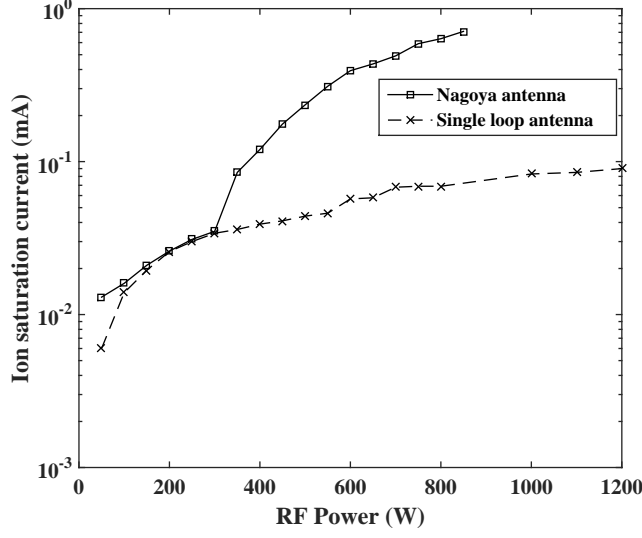
Figure 6.2: Variation of the ion saturation current with power in hydrogen plasma for comparison between the loop antenna and the nagoya antenna.

Once this density jump is established with the Nagoya antenna, a more detailed parametric analysis is carried out at RF power$> 400W$. The results are shown in figure 6.3. There are further jumps in ion saturation current at $P_{RF} > 600W$. These jumps corresponds to the transition from the inductive to the helicon mode of plasma coupling. The figure shows the variation of ion saturation current for different pressures and different magnetic field values at $z = 0$ location. It is seen that at lower pressure (6 mTorr) the percentage ionization achieved is the maximum. Whereas, it is minimum for the case of 30 mTorr. Furthermore, the density jump is clearly seen at low pressures for all the field values. For low pressure discharges, the wave penetration into the plasma is much more than at higher pressures. This is shown by Shamrai et al. in 1997 [124], where they have studied the penetration depth of the helicon wave as a function of the collision frequency (ν). For lower values ν/ω ratio, the wave penetrates deeper into the plasma. For these reasons, further characterization is done at 6 mTorr hydrogen gas pressure in the chamber at or above 800 W input power to ensure the discharge
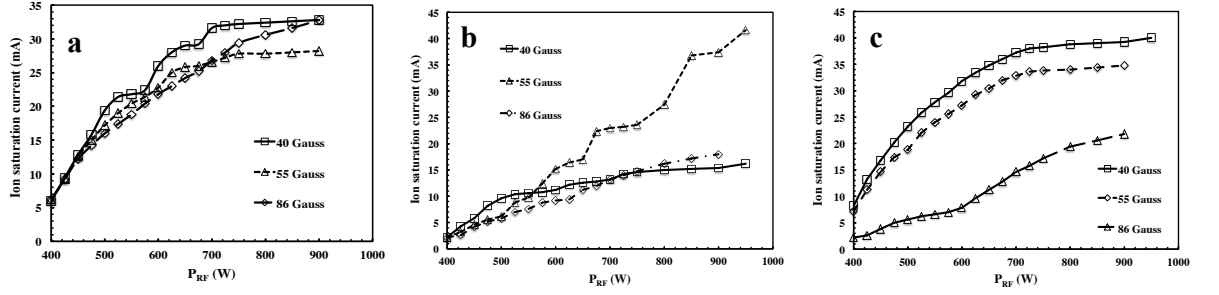
Figure 6.3: Variation of the ion saturation current with power showing mode transition through sudden jump in the current value for three pressures (a) 6 mTorr ($8 \times 10^{-3} mbar$), (b) 7.5 mTorr (0.01 mbar) and (c) 30 mTorr (0.04 mbar).

is operated in the helicon regime.

The Nagoya antenna excites a $m = 1$ azimuthal helicon mode in the plasma. As shown in the section 2.4 (equation 2.33) the axial component of the helicon wave field is given by the equation

$$B_z = iAk_\perp J_1(k_\perp r) \qquad (6.1)$$

From 6.1 it can be seen that the B_z component of the wave field would follow a first order Bessel function having a minima at the centre. The B-bot probe described in section 4.3.4, is used to measure the wave fields. The field profile is another signature of the helicon wave and the helicon modes excited in the system. Kyeong-Koo Chi et al. (1999) [115] showed the presence of different azimuthal modes with the help of the radial profiles of B_z. In figure 6.4, the radial profile B_z component of the wave is shown. This profile is obtained by a rotatable, L-shaped B-dot probe at $P_{RF} = 800W$, $z = 7cm$, 6 mTorr H_2 pressure keeping the separation between the top flange and the permanent magnet $= 12cm$. The B_z is minimum at the centre and the maximum value is attained at $r = 1.5cm$. This is a typical first order Bessel function variation which shows that an $m = 1$

mode has been excited in the plasma. The experimental data is fitted with the Bessel function from equation 6.1. From the fitting parameters we can find the value of the perpendicular wave number of the helicon wave. From figure 6.4, $k_\perp$ comes out to be $\sim 1.8\ cm^{-1}$. If $a =$ plasma radius, using the boundary condition $B_r(r = a) = 0$, described in section 2.4 we see that an expression for the $k_\perp$ can be derived, which is given in equation 2.41 and re-written here:

$$k_\perp = 3.83/a; \tag{6.2}$$

For the present experimental conditions, $a = 2.5\ cm$ for which $k_\perp$ comes out to be $1.53\ cm^{-1}$ which is close to the experimentally observed value.
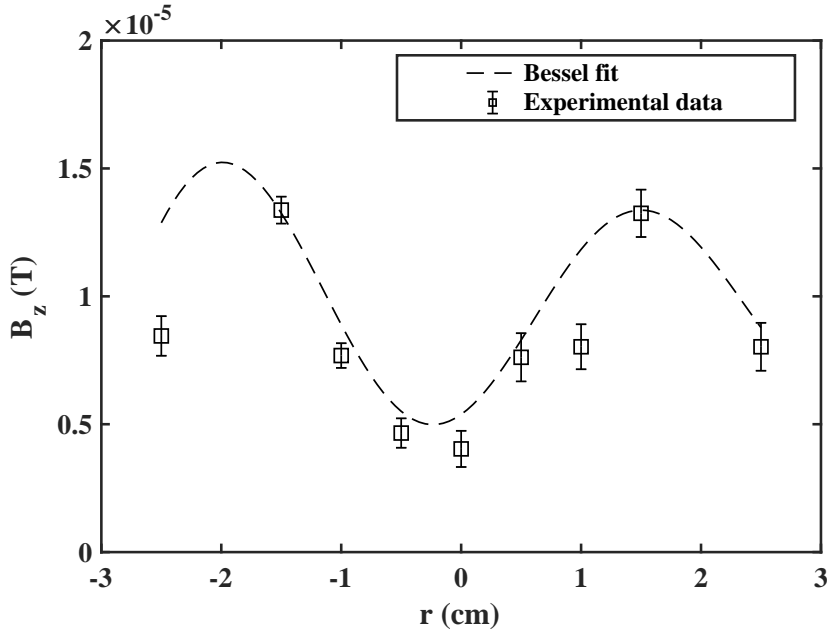
Figure 6.4: Radial profile of the axial component of the wave field, B_z showing the excitation of $m = 1$ helicon mode in the plasma taken at $z = 7cm$.

6.3 Plasma Characterization

Figures 6.5, 6.6 and 6.7 show the axial density profiles for three axial magnetic field configurations corresponding to $d = 10cm, 12cm$ and $14cm$, where d is the separation between the top flange and the centre of the ring magnet. The source region has a density of $\sim 3.5 \times 10^{18} m^{-3}$ for all three cases. The maximum density is observed below the antenna, which almost covers the glass source chamber. The density decreases rapidly as z increases and as we move away from the antenna and into the expansion chamber. However, the density rises again at roughly around the same location for the three cases. This rise in density away from the antenna is discussed in the next section. From the point of view of the production of negative hydrogen ions, we need high electron density in the device and a negative axial temperature gradient.

(a)   (b)
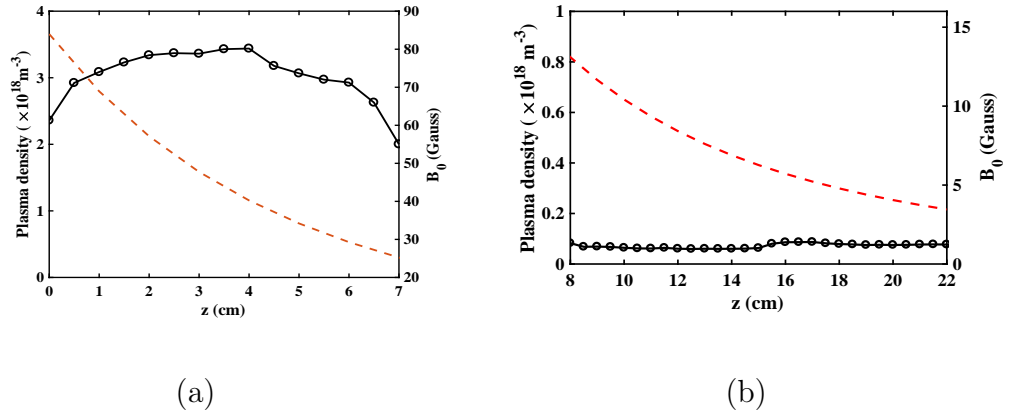
Figure 6.5: Axial density profile (solid line) for $d = 10$ cm, at $P_{RF} = 800$ W and 6 mTorr pressure in (a) source tube and (b) expansion chamber plotted alongside the axial magnetic field values (dashed line).

The axial temperature profile in the source tube is shown in the figure 6.8. The temperature profile is not affected much by the distance of the permanent magnet from the source. This is because the magnetic field configuration in the source does
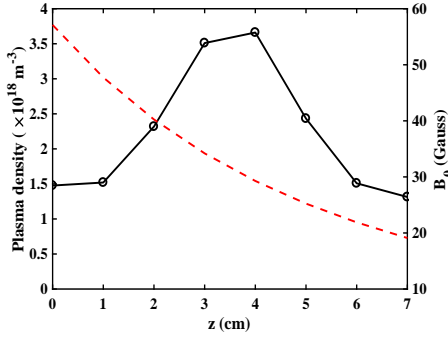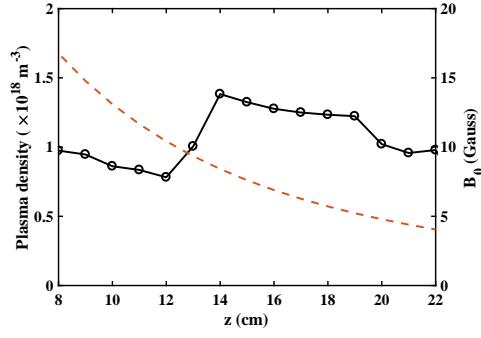
(a)   (b)

Figure 6.6: Axial density profile (solid line) for $d = 12$ cm, at $P_{RF} = 800$ W and
6 mTorr pressure in (a) source tube and (b) expansion chamber plotted alongside
the axial magnetic field values (dashed line).

not change much, the field remains more or less radially uniform and the electrons

remain magnetized for all of the cases.
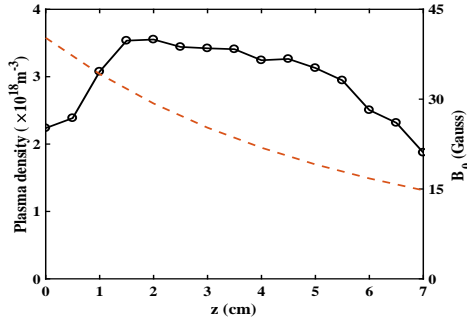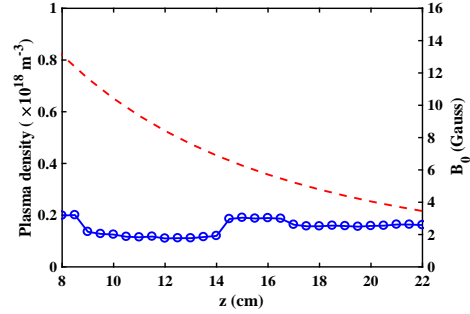
(a)   (b)

Figure 6.7: Axial density profile (solid line) for $d = 14$ cm, at $P_{RF} = 800$ W and
6 mTorr pressure in (a) source tube and (b) expansion chamber plotted alongside
the axial magnetic field values (dashed line).
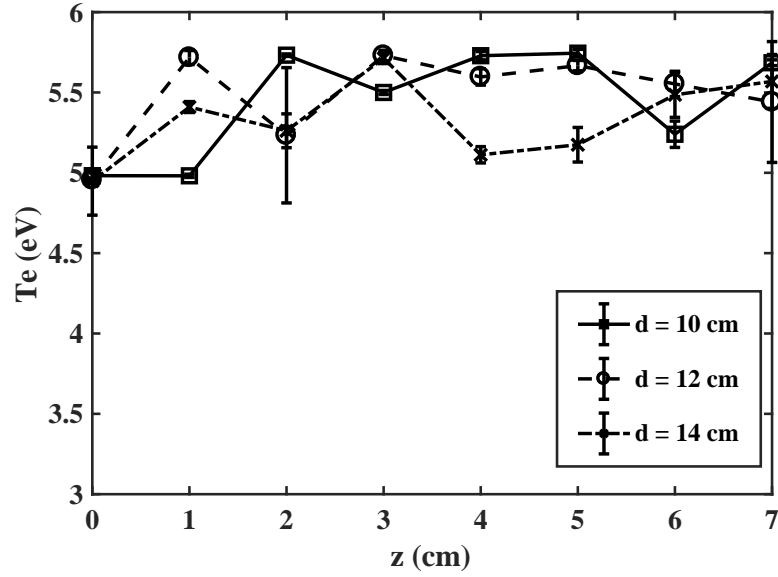
Figure 6.8: The axial temperature profile in the source chamber at 6 mTorr pressure and 800 W input RF power.

Figure 6.9 shows the radial density and temperature profiles at $z = 19cm$. This is also the location where all the negative hydrogen ion density measurements are done (chapter 7). The radial profile of the density shows a centrally peaked profile for $d = 12cm$ and almost flat profiles for the other two cases. This shows that the wave propagation is strongly affected by the magnetic field configuration.

This will be more comprehensible when we will discuss the wave propagation in the next section. The radial temperature profiles in the expansion chamber are also affected by the magnetic field configuration as shown in figure 6.9. Although, temperature profile remains almost flat for all the cases but for $d = 12cm$ the temperature is lower than for the other two values of d. Thus, it is safe to conclude that the wave propagation at $d = 12cm$ is different from wave propagation at $d = 10cm$ or $d = 14cm$. We investigate this phenomenon in the next section.
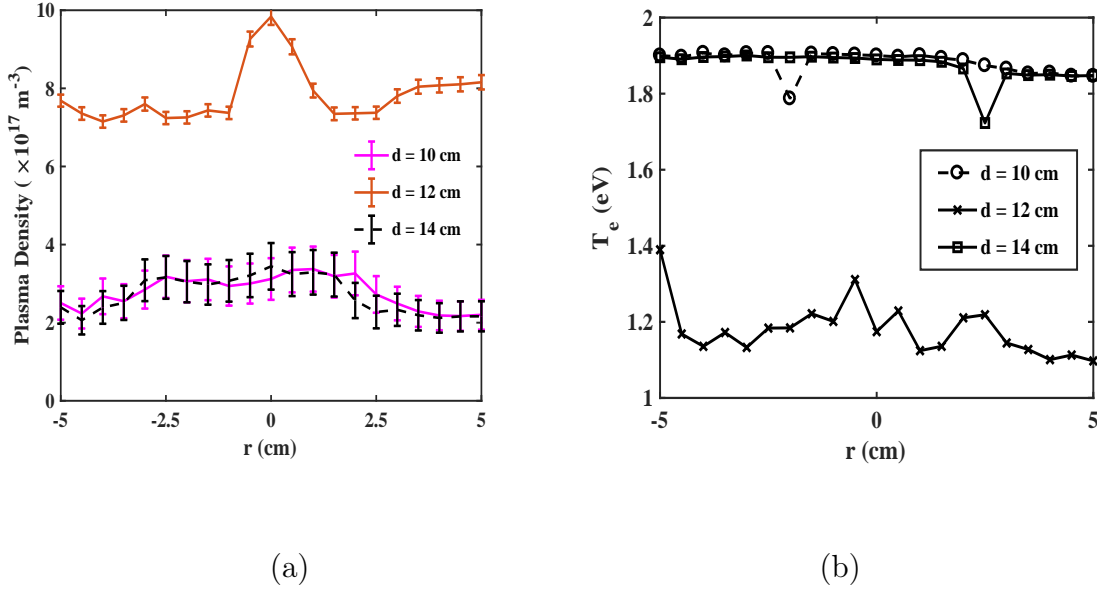
Figure 6.9: The radial profiles of the (a) plasma density and (b) electron temperature are shown, obtained at $z = 19$ cm location at $P_{RF} = 800$ W and 6 mTorr pressure for three d values.

6.4 Density rise away from antenna

The HELEN-I setup is unique in terms of the magnetic field configuration in the expansion chamber. There is an azimuthal cusp field configuration present in the expansion chamber as well as a longitudinal cusp configuration due to the permanent ring magnet and the cusp magnets. Seiji Takechi et al., [125] (1999), showed the effect of the cusp position on the propagation angle of the wave. We also see a similar effect in our experiment. This is discussed in some detail later in this chapter. The variation of the separation between the top flange at $z = 0$ and the permanent ring magnet leads to different magnetic field configurations inside the expansion chamber. The effect of this can be seen in figures 6.5 to 6.7. These figures show the axial density profiles for three different d values and hence

different magnetic field configurations. The maximum density in the source region is achieved under the antenna and decreases downstream before rising again in the expansion region away from the antenna. Such a density rise away from the antenna in the downstream region has been reported earlier by Sudit and Chen [121]. Prabal et al. [92] have attributed this phenomenon to the resonant absorption of the wave field energy through the wave propagation along the resonance cone. The concept of the resonant absorption along the resonance cone surface has been discussed in detail by Fisher and Gould (1971) [90] in magnetoplasmas and Degeling et al. [89] and Nazarov et al. [91] in helicon plasmas. Degeling showed that near the helicon frequency range in a plasma immersed in an axial magnetic field, due to the anisotropy in the refractive index the propagation of the wave is directly affected. The wave undergoes strong absorption at certain angles of the wave propagation. The angle at which this occurs is called the resonance angle. It is the angle which the phase velocity makes with the external field. The resonance occurs at a certain angle because at that particular angle lies the surface of a cone, with its axis parallel to the external magnetic field. At the surface of the cone the field magnitude becomes very large [90].

Figure 6.9 shows the radial density and temperature profiles for different values of d at $z = 19$ cm, where d is the separation between the top flange and the ring magnet center. The different values of d basically correspond to different magnetic field configurations in the expansion chamber. It is observed that for $d = 12$ cm the profile is peaked at the centre, whereas for the other two values the density profile remains almost flat at the centre. The ring magnet separation, $d = 12cm$ from the driver back plate, is found to be optimum for the negative hydrogen ion formation, as will be discussed in chapter 7, since the plasma density is significantly higher and plasma temperature is lower for this configuration. Figure 6.10shows the axial wave magnetic field profiles at two different values of d with $d = 10$ cm and $d = 12cm$ respectively. In the second case, it is seen that the wave is suddenly

damped after $z = 11$ cm whereas, in the first case we do not see any such sudden damping. The sudden damping could imply a resonance absorption at that axial location. The phase (ϕ) variation with z for the two cases is given in figure 6.11. The phase data is obtained by moving the B-dot probe axially and comparing the phase of the signal, thus obtained, with a fixed reference signal of 13,56 MHz taken as the antenna current signal from a current transformer. The first case ($d = 10$ cm) shows that the phase increases monotonically until $z = 12 \pm 1$ cm and approximately remains constant for $z > 13$ cm. The axial wavelength ($\lambda_\parallel$) for this case is found by linear fitting of the phase plot until the monotonic increase [126]. The slope of the linear fit on the experimental data gives $d\phi/dz$. $\lambda_\parallel$ can be obtained from the relation $\lambda_\parallel = 360/(d\phi/dz)$. Axial wavelength, $\lambda_\parallel$ comes out to be $\sim$ 11.2 cm. The monotonic increase in the phase correspond to a propagating wave and the constant phase value represents a standing wave formation. This kind of behavior has been reported by Soumen et al. where the standing wave behavior is responsible for localized electron heating and subsequent localized density increase. This is also observed in HELEN-I, as shown in figure 6.12 where the downstream density profiles for different d cases have been compared. The $d = 12$ cm case has the maximum rise in the density. To understand this, we go back to figure 6.11. Here, the phase variation is shown for $d = 12$ cm case. We do not see any standing wave like behavior here. Rather, the phase monotonically decreases along z until $z \sim 13$ cm and increases after that.

From figures 6.4 and 6.11 $\lambda_\parallel = 6.9 cm$, $k_\parallel = 0.91 cm^{-1}$ and $k_\perp = 1.8 cm^{-1}$. The angle of propagation ($\theta = tan^{-1}(\frac{k_\perp}{k_\parallel})$) from these values comes out to be $\sim 63°$. The density rise for this case occurs at $z = 13$ cm. At this location we find that for $d = 12$ cm separation, $\omega \sim \omega_{ce}/2$. The dispersion relation for an electromagnetic wave propagating obliquely to the magnetic field with frequency lying between ion
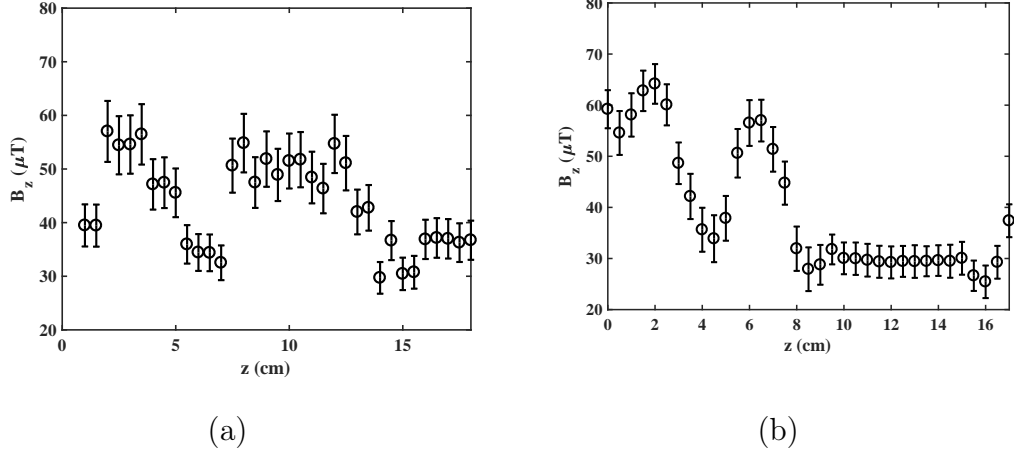
Figure 6.10: The axial profiles of the B_z is shown for the two cases a) $d = 10$ cm and b) $d = 12$ cm.

plasma and electron cyclotron frequency as derived in chapter 3 is given by:

$$\frac{k^2 c^2}{\omega^2} = \frac{\omega_{ce}^2}{\omega(\omega_{ce} cos\theta - \omega)} \tag{6.3}$$

At resonance $k \to \infty$, implying that the denominator in the equation 6.3 should vanish.

$$\omega(\omega_{ce} cos\theta - \omega) = 0; \tag{6.4}$$

which means that at resonance, $cos\theta = \omega/\omega_{ce}$, where θ is the angle of propagation or the angle between the phase velocity of the wave and the magnetic field. At $\omega = \omega_{ce}/2$, $\theta = 60°$ which closely matches with the experimentally found value of the propagation angle ($63°$). This case correspond to the propagation along the surface of the resonance cone where the field is maximum [90], [89]. Now we are in a position to explain the figure 6.11. For $d =10$ cm, we have a simple standing wave formation and as reported by Soumen [126] and Sudit [121] we have a local electron heating source there. But, the condition is more interesting for the magnetic field configuration when $d = 12$ cm. Here, the phase first starts to decrease with z and reaches a minima at $z = 13$ cm. Since the phase is measured with respect to a fixed
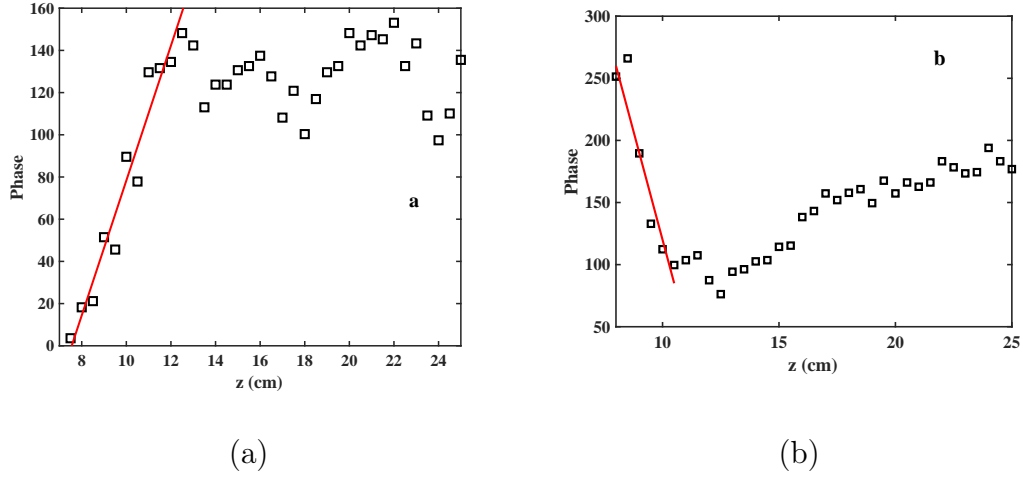
Figure 6.11: The phase profile of the B_z is shown for the two cases a) $d = 10$ cm and b) $d = 12$ cm. The linear fit is shown by the red line.
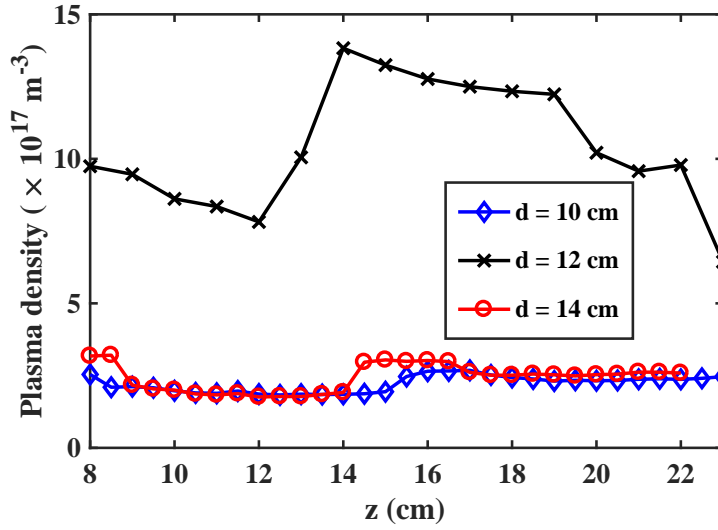
Figure 6.12: Downstream density profiles for the three different values of d at $P_{RF} = 800$ W and 6 mTorr pressure.

reference, the phase profile implies that with z the phase velocity increases as the phase difference between the wave and the reference decreases. This behavior can be understood from the dispersion relation curve of the whistler waves where the phase velocity increases as ω approaches $\omega_{ce}/2$ [127]. In the present experiment the

ratio ω/ω_{ce} increases as we go downstream and reaches the value 2 at $z \sim 13cm$. At $\omega_{ce}/2$ the phase as we have shown above the resonance condition is satisfied which means that the wave propagation is along the resonance cone leading to strong wave absorption at that location and density rise away from the antenna.

7

Negative Ion Production and Density Measurement

In the Helicon wave heated plasmas, the presence of very high plasma densities and electron temperatures as low as $\sim 1 - 2eV$ favour the production of negative hydrogen ions (H^-) and lower their destruction due to reduced cross-section of negative ion destruction processes (electron-detachment). In this chapter, we discuss these negative hydrogen ion production and destruction mechanisms. Various non-intrusive diagnostic techniques that are used to experimentally determine the (H^-) density are discussed in detail. A simple particle balance model to calculate the expected (H^-) density in the HELEN set up is also described. Results from this chapter have been compiled to be published in a peer reviewed journal [122].

7.1 Introduction

Negative hydrogen ion (H^-) sources have found applications in a variety of research areas like particle accelerators and neutral beam injection for fusion plasma heating. Plasma heating by very high energy neutral beams is one of the most

efficient heating mechanisms in tokamaks. At high energies the neutralization efficiency of positive hydrogen ion is very small, while H^- ion beams are shown to have a neutralization efficiency of $\sim 60\%$ at energies as high as 1 MeV for conventional gas based neutralizer [128]. For the production of negative hydrogen ions low pressure, low temperature hydrogen plasmas are desirable [41, 76, 129]. The low pressure is needed to avoid stripping losses, while low temperature electrons are required to form H^- ions by dissociative attachment (discussed later in this chapter). Usually, the requirement for the low energy electron is fulfilled by a low work function electron emitter (Caesium) in the plasma. H^- ions are produced on a low work-function surface due to surface conversion of energetic H atoms H_0^* or hydrogen ions (H_n^+) in the plasma [76]; This is called the surface process of H^- formation.

$$H_0^*/H_n^+ \xrightarrow{Low\,work-function\,surface} H^-.$$
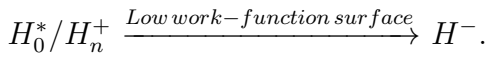
Surface process is more efficient than that of the volume process in terms of H^- yield. Recently, Kakati et al. [130] have reported a proof of the principle negative hydrogen ion source based on a novel concept of surface assisted volume process using Caesium coated tungsten dust dispersed in the volume. But, the handling of Caesium and its deposition on exposed surfaces is a major problem in such ion sources.

In the volume process, H^- ion is formed in two steps

1)$e_{fast} + H_2(\nu') \rightarrow e + H_2(\nu'') + h\nu$

2)$H_2^*(\nu'') + e_{slow} \rightarrow H^-$ (Dissociative attachment)

It can be seen from these processes that both the fast as well as slow electrons have a role to play in the formation of H^- ions. In the first reaction the vibrational ground state of hydrogen molecule is represented by $H_{(\nu')}$ and vibrationally excited state by $H_{(\nu'')}$. It is crucial to have a source design that permits the existence of different electron temperatures in the device. Usually, this is done by dividing the system into two parts by a transverse magnetic filter field. The driver region

contains the fast electrons and extraction region accommodates slow electrons [76]. The low energy electrons diffuse through the filter field via collisions with neutrals. The magnetic filter helps to maintain low electron temperature in one part of the system. This increases the chances of electron attachment and reduces H^- destruction. The downside to using a filter field arrangement is the electron density reduction near extraction region. The plasma flow to the extraction region is restricted due to the filter field leading to a low density of H atoms and H^+ in the extraction zone. The filter field would also produce plasma drifts and eventually lead to non-uniformities in the ion source and result in deflection of the ion beam trajectories. Therefore, a technique which could maintain the contrasting electron temperatures in the source region and extraction region keeping the plasma density high at the same time is highly desirable for H^- ion sources. A helicon plasma source in an expanding magnetic field have been shown to exhibit a temperature gradient like the one needed for the production of H^- without using the transverse filter field. [15, 47, 131, 132].

7.2   Mechanism of H^- production

As stated previously, the negative hydrogen ion formation in plasmas happens through volume and surface processes. In the volume process, there are several sub-processes involved in the production and destruction of negative hydrogen ions. This section mainly describes the production processes and briefly discusses the main destruction processes. Dissociative electron attachment to the ro-vibrationally excited hydrogen molecules is the primary mechanism of the production of H^- ions through the volume process. Whereas, in the surface process the electron from a low work function metal surface is directly transferred to the hydrogen atoms as shown in figure 7.1.

Nicolopoulou (1977) [133] and Bacal (1979) [134] showed that the Dissociative
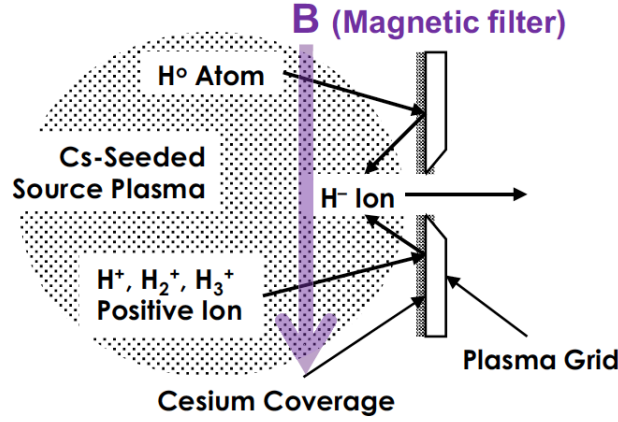
Figure 7.1: H^- ion formation by Cs covered plasma grid surface. Source: [11]

Attachment (DA) to the ground electronic and vibrational state of H_2, Polar dissociation of H_2 and Dissociative recombination of H_2^+ are important mechanisms of the production of the H^- ions. But, the calculations following this gave H^- density which was 100 time smaller than the experimentally found H^- density. Bottcher and Buckley [135] (1979) showed that the cross section for dissociative attachment (DA) to low vibrational levels of the ground electronic state of the hydrogen molecules is substantially smaller than the DA cross section to higher vibrational levels ($\nu'' \geq 4$). Wadehra and Bardsley [136] (1978) calculated the cross sections for DA (σ_{DA}) to different vibrational (ν) and rotational (j) excitation states of H_2 molecule and found out that σ_{DA} increases by 4 orders of magnitude to $\sim 10^{-21} m^2$ in going from $\nu = 0$ to $\nu = 4$ at $j = 0$ at low electron temperature ($Te < 4eV$). Whereas, for DA to higher rotational levels the DA cross section increases by two orders to $\sim 10^{-24} m^2$ from $j = 0$ to $j = 10$. Thus, the DA to higher vibrational levels play the major role in the production of H^- ions. This shows that the vibrational excitation of H_2 molecule and their destruction are important processes in determining the H^- yield. The main processes responsible for the vibrational excitation of ground state hydrogen molecule $H_2(\nu')$ to vibrationally excited molecule $H_2(\nu'')$ are listen in table 7.1 and the major processes responsible

132

for $H_2(\nu'')$ destruction are given in table 7.2. Therefore, for higher yield of H^- ions larger density of higher vibrational states of H_2 is desirable. J. R. Hiskes (1991) [137] has calculated the cross-section for the vibrational excitation of H_2 molecule to higher levels. The vibrational excitation is significant only when the

Table 7.1: Processes contributing to the formation of $H_2^*(\nu'')$.

Processes	Reactions
e-V	$e + H_2(\nu') \rightarrow e + H_2(\nu''); (\nu'' > \nu')$
E-V	$e + H_2(\nu') \rightarrow e + H_2(\nu'') + h\nu$
s-V	$Wall + H_n^+ \rightarrow H_2(\nu''); n = 1, 2, 3.$

Table 7.2: Processes contributing to the destruction of $H_2^*(\nu'')$.

Processes	Reactions
Dis	$e + H_2(\nu'') \rightarrow e + 2H$
Ion	$e + H_2(\nu') \rightarrow 2e + H_2^+$
DA	$H_2^*(\nu'') + e_{slow} \rightarrow H^-$

Table 7.3: Processes contributing to the destruction of H^-.

Processes	Reactions
Electron Detachment	$H^- + e \rightarrow H + 2e$
Mutual neutralization	$H^- + H^+ \rightarrow H(p) + H$
Associative Detachment	$H^- + H \rightarrow 2H + e$

electron temperature is greater than 20 eV. Thus, in the volume production mode, high energy electrons are required for the production of H^- ions but they also contribute to their destruction through electron detachment (ED) process. The ED cross section increases with electron energy and is significant for $T_e > 4$ eV. Other H^- destruction processes include Mutual Neutralization (MN) with H^+ ions and Associative Detachment (AD) of electron by H atom. The major processes involved in the destructon of H^- are listed in table 7.3.

Thus, the production rate should be significantly higher than the destruction at equilibrium in order for the H^- source to produce a good H^- yield. The net H^- density is obtained after subtracting the destructive processes from the H^- producing processes.

7.3 Diagnostic Techniques for H^- ion density measurement

7.3.1 Optical Emission Spectroscopy (OES)

An Optical Emission Spectroscopy (OES) based non-intrusive technique has been used to measure the negative ion density in HELEN-I. OES is widely used plasma diagnostic technique for the measurement of plasma parameters such as electron density, electron temperature [15] etc. The Balmer lines in the hydrogen spectrum corresponding to 656nm (H_α) , 486nm (H_β) and 334 nm (H_γ) are used to measure the H^- ion density averaged over the line of sight (LOS) [128]. Light from the plasma is collected using a collimating lens of aperture $\sim 12mm$ and is transmitted to the spectrometer through an optical fibre. As listed in table 7.4, the processes contributing to the population of excited state of atomic hydrogen lead to optical emissions which are then recorded by the spectrometer. Using a Collisional Radiative (CR) model, the population coefficients for these processes can be calculated. These coefficients are functions of plasma density or plasma temperature or both. The individual contribution from the five processes in table 7.4 to the Balmer line emission for different plasma parameters have been discussed in [128]. The contribution of the H^- to H_α emission, dominates for the electron density range $10^{16} - 10^{21} m^{-3}$. The effective rate coefficient for mutual neutralization, $\chi_{H_{\alpha,\beta}}^{eff,H^-}$ is independent of the electron temperature as the process involves interaction of ions only [128]. The contribution of all the processes shows reduced dependence

on electron temperature for the line ratio H_α/H_β except for mutual neutralization which has strong dependence on electron density. Due to this dependency of Balmer lines on H^- density, the value of the line ratio H_α/H_β can be used for the measurement of negative ions. However, this analysis becomes error prone at high pressures and the assumptions are valid only for pressures of 1 Pa (7.5 mTorr) or lower. This is because at higher pressures other channels of radiative processes (self-absorption of Lyman lines and dissociative recombination of H^{3+}) would also affect the photon emissions. The dominant processes for transitions from quantum numbers $p = 3$ and $p = 4$ are effective excitation and mutual neutralization. Hence, only these two processes have to be taken into account while calculating the line ratio H_α/H_β. Thus, the line ratio is given by:

$$\frac{H_\alpha}{H_\beta} = \frac{n_H \chi_{H_\alpha}^{eff,H} + n_{H^-} \chi_{H_\alpha}^{eff,H^-}}{n_H \chi_{H_\beta}^{eff,H} + n_{H^-} \chi_{H_\beta}^{eff,H^-}} \tag{7.1}$$

The contribution of mutual neutralization on the population of quantum numbers $p > 4$ and thus H_γ, H_δ, etc, are negligible [128]. In order to get the H^- density from equation 7.1 we need the atomic hydrogen population. To determine the density of atomic hydrogen, absolute measure of H_γ line emission can be used,

$$H_\gamma = n_H n_e \chi_{H_\gamma}^{eff,H}(T_e, n_e) \tag{7.2}$$

Using equations 7.1 and 7.2, a formula can be derived for given T_e and n_e,

$$n_{H^-} = \frac{H_\gamma}{n_e} C_1 \left(1 - \frac{H_\alpha}{H_\beta}\frac{1}{C_2}\right)\left(1 - \frac{H_\alpha}{H_\beta}\frac{1}{C_3}\right)^{-1} \tag{7.3}$$

where,

$$C_1 = \frac{\chi_{H_\alpha}^{eff,H}}{\chi_{H_\gamma}^{eff,H}}\frac{1}{\chi_{H_\alpha}^{eff,H^-}}, C_2 = \frac{\chi_{H_\alpha}^{eff,H}}{\chi_{H_\beta}^{eff,H}}, C_3 = \frac{\chi_{H_\alpha}^{eff,H^-}}{\chi_{H_\beta}^{eff,H^-}} \tag{7.4}$$

The factor C_1 represents the ratio of effective excitation rate coefficient for H_α

Table 7.4: Processes contributing to excited state of atomic hydrogen.

Processes	Reactions
Recombination	$H^+ + e \rightarrow H(p)$
Dissociative recombination	$H_2^+ + e \rightarrow H(p) + H$
Effective excitation	$H + e \rightarrow H(p) + e$
Mutual neutralization	$H^- + H^+ \rightarrow H(p) + H$
Dissociative excitation	$H_2 + e \rightarrow H(p) + H + e$

and H_γ divided by the effective mutual neutralization rate coefficient for H_α. C_2 can be interpreted as the line ratio H_α/H_β when the excitation takes place from atomic hydrogen only. C_3 represents the line ratio H_α/H_β when the excitation takes place from negative hydrogen ions only. These factors can be calculated using CR model for known plasma parameters [138].

7.3.2 Cavity Ring Down Spectroscopy (CRDS)

The CRDS technique, developed by O'Keefe and Deacon, is based upon the measurement of the rate of absorption of a light pulse confined within a closed optical cavity [139]. It is a very sensitive diagnostic based on photon absorption by H^- ions. It has been developed and employed in HELEN-I setup to measure the density of particles present in a trace amount [140–142], e.g. negative hydrogen ion in the present case [143]. Recently, Agnello et al. have shown that CRDS can be used for measuring the H^- ion density in a hydrogen helicon plasma where the H^- ion population is small compared to the H^+ ions [2].

When a laser of photon energy higher than the electron affinity of H^- ion ($\sim$ 0.76 eV) enters into a cavity formed by two highly reflecting mirrors placed at two ends of the cavity, the loosely bound electron in H^- ion is detached by the laser photon due to laser photo-detachment reaction and the corresponding photons are considered absorbed. In the present experiment, a Nd:YAG (Innolas make), infrared laser of 1064 nm wavelength is fed into the plasma in the expansion

chamber as shown in figure 3 through a 99.99% reflecting mirror, m_1 (attached to left side port at $z = 19cm$ from the endplate). Only 0.01% of the photons go into the plasma. The port on the opposite end of the laser entrance attached to a long (900 mm) trapping cavity also has a mirror, m_2, identical to m_1. This arrangement of two highly reflecting mirrors forms a cavity where the laser is trapped to make multiple reflections and so multiple pass through the plasma volume. Due to the cavity configuration by two mirrors, remaining laser photons bounce back and forth multiple times between the two mirrors. In each of these trips through the plasma medium, a fraction of total number of photons get absorbed with time. As a result, a temporally decaying laser intensity profile is recorded by a detector kept just outside the cavity. The decay time constant, known as ring down time (RDT) is used to calculate the density of H^- ions inside the plasma. Just outside the cavity, a photodetector is placed to receive the photons transmitted through m2.The laser beam is $2mm$ in diameter with a pulse width of $6ns$. The maximum beam energy can be as high as $180mJ$. The energy of a photon with wavelength 1064nm is 1.2 eV. This energy is sufficiently higher than the electron affinity (0.76 eV) of H atom to form H^- ions and therefore the photon is able to detach the loosely bound electron. The exponential decay of the photon beam with decay time T_1, is relatively slow in vacuum ($< 0.04mTorr$) since the photons are scattered less in vacuum. Whereas, when the plasma is switched on the interaction of the photons with the medium is stronger because of the availability of H^- ions which absorb the photons of 1064 nm and neutralize. The decay time with plasma switched on is smaller and is denoted by T_2. Using these decay times in vacuum and in plasma we can compute the H^- density by the following relation:

$$n_{H^-} = \frac{L}{\sigma dc} \left(\frac{1}{T_2} - \frac{1}{T_1} \right) \tag{7.5}$$

where, $L = 120cm$ is the total length of the cavity, length of the cavity, $d = 10cm$
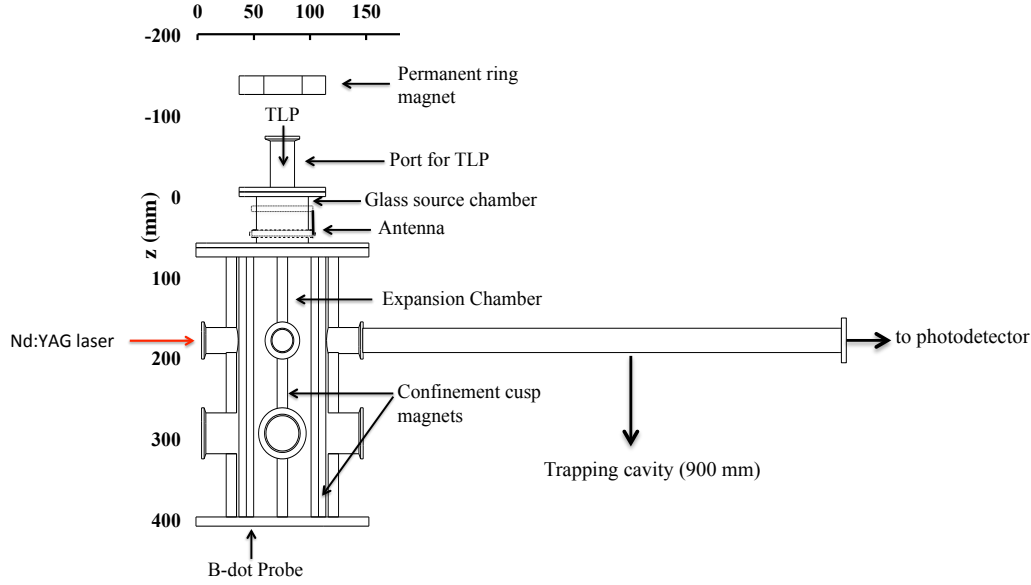
Figure 7.2: HELEN-I experimental set-up attached with $\sim$ 1 m length CRDS cavity.

is the plasma length through which laser is passing, $\sigma = 3.5 \cdot 10^{-17} cm^2$, photo-detachment cross-section or laser absorption cross-section. A detailed CRDS development description and a parametric study of negative hydrogen ion density measurement in HELEN using CRDS is done by Debrup et al. [143]. Both OES and CRDS measures line of sight averaged H^- ion density, but due to axial and associated cusp magnetic field structure in the present Helicon source, a non-uniform radial profile of H^- ion density is expected. So, a local H^- ion measurement is needed to study the profile. To measure local H^- ion density to generate its profile a Laser Photo Detachment (LPD) diagnostic is underdevelopment.

7.4 Results

- *Line Ratio method*

  The method of H_α/H_β line ratio diagnostic is explained in section 7.3.1. The line emission is measured with Ocean Optics USB 4000 spectrometer. The spectrometer

operates in the wavelength range of $\lambda = 200 - 1100$ nm with a spectral resolution of 2 nm. Emitted light from the plasma is collimated using a lens and is transported to the spectrometer with the help of an optical fibre. The diameter of the lens is $12mm$ and focal length, $f = 10mm$.
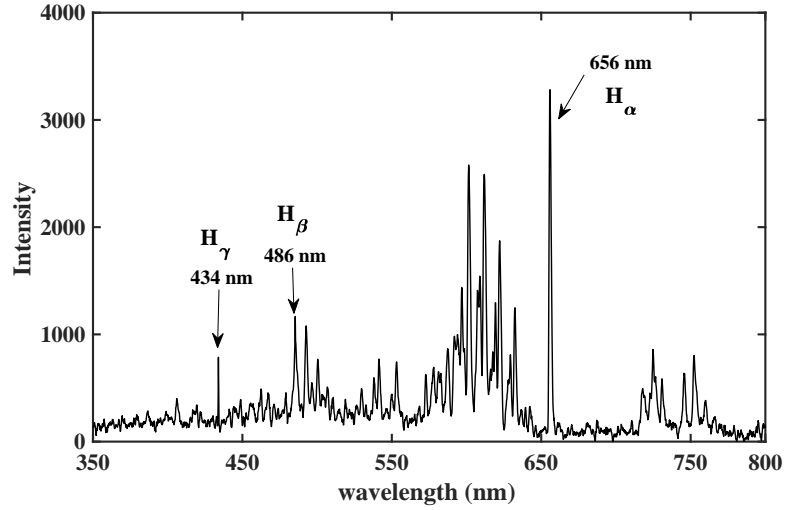
Figure 7.3: Typical OES spectrum showing different atomic and molecular lines.

A typical spectrum obtained for a hydrogen helicon plasma is shown in figure 7.3 and such spectra are recorded for three different working pressures and for five different magnetic field configurations. The values of effective emission rate coefficients used for the calculation of the coefficients C_1, C_2, and C_3 are calculated from the collisional radiative model based open access Atomic Data and Analysis Structure (ADAS) system [138]. The rate coefficients have dependence on the electron temperature and density. Plasma density and electron temperature are already known from Langmuir probe measurements (section 6.3). Using the values of electron temperature and density, the rate constants and hence the coefficients C_1, C_2, and C_3 can be found out. Using these values in equation 7.8 the negative ion density is calculated. The result is shown in figure 7.4. H^- density close to $10^{16} m^{-3}$ is obtained from the line ratio measurements at 800W rf power. This diagnostic gives the H^- density averaged over the plasma volume along the line of

sight with $\sim 40\%$ error associated with the calculated H^- density values [128].
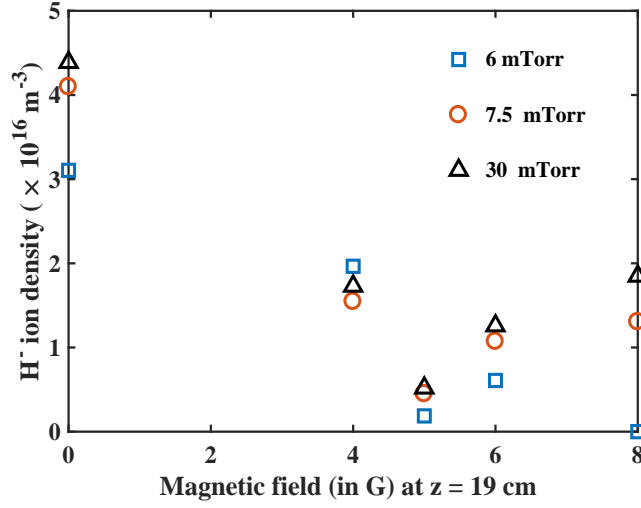
Figure 7.4: H^- ion density obtained from the H_α/H_β line ratio method.
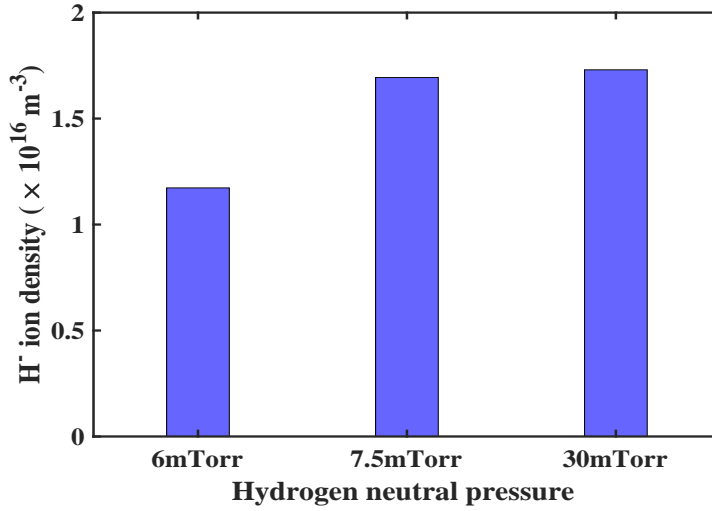
Figure 7.5: H^- density averaged over different magnetic field values.

To verify the OES measurements a more sensitive CRDS diagnostic technique is used. The H^- density calculated from the line ratio method depends inversely on the electron density from equation 7.3, which is the reason for getting the maximum H^- density for $B_0 = 0$ Gauss case in figure 7.4. The H^- density measurements

through the line ratio method have a maximum error of 40%. In the figure 7.4 the variation of H^- density with axial magnetic field is plotted at different pressures. The magnetic field due to the permanent magnet is weak at $z = 19cm$ location and is varied by varying the magnet position. The variation with pressure is not observed. Figure 7.5 shows the H^- density averaged over different magnetic field values to see the effect of pressure. The H^- density increases with pressure but saturates at high pressures. The reason for this behavior is discussed in the next section.

- *CRDS method*

  The CRDS system attached to the experimental setup is shown in figure 7.2. The preliminary results obtained from the experiments are shown in the following figures. These values are obtained at 6 mTorr neutral pressure and very low dc field ($\sim 5G$) at the location where the density is measured. A detailed parametric CRDS study of negative ion density variation in HELEN-I is given in ref [143]. As
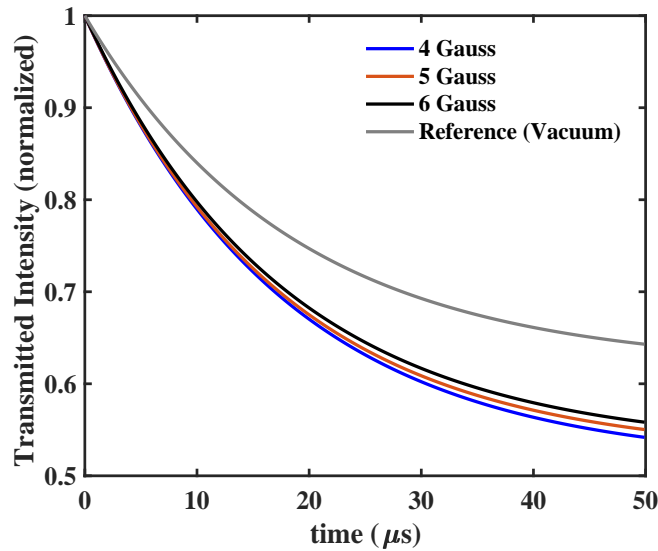
Figure 7.6: Decay signal of the normalised light intensity transmitted through mirror m_2 in the CRDS experiment for different dc magnetic field values at $z = 19$ cm. The vacuum signal is also shown for comparison.
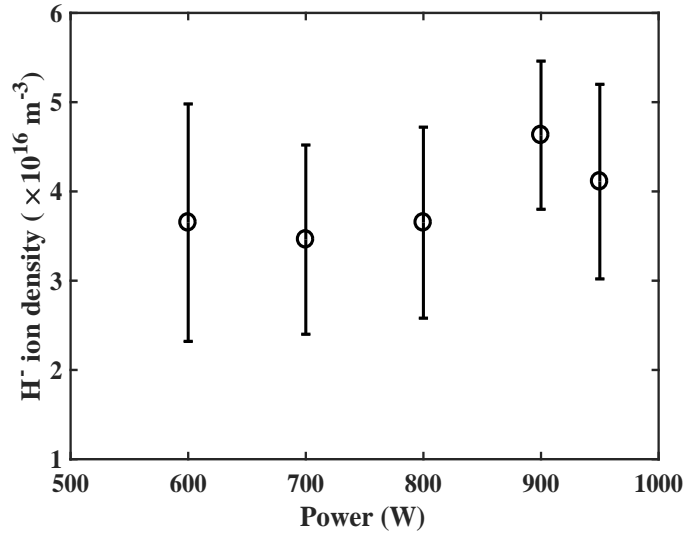
Figure 7.7: Variation of the H^- ion density with increasing RF power obtained by the CRDS experiment ($z = 19$ cm).

explained in section 7.3.2 the exponential decay of the transmitted photon signal is detected and the time in which the signal attains $\frac{1}{e}$ times its value at $t = 0$ is called the Ring Down Time. The ring down time plot of the CRDS experiment is shown in figure 7.6. The ring down time is obtained from the exponential fit of this signal. This is used in equation 7.5 to calculate the negation hydrogen ion density. Background (vacuum) time constant is T_1 and other fits are T_2 for respective plasma cases are used in the (CRDS) equation 7.5 to calculate H^- ion density for different cases. It is observed that negative ion detection starts after a certain power > 600W (figure 7.7). There are certain factors leading to this result. The plasma potential and electron temperatures are higher in the downstream region at lower applied RF power because the plasma is still in the capacitively coupled mode with lower plasma density. Since the electron temperature is high in CCP mode than in helicon mode and electron density is lower, the density of higher vibrational states of hydrogen molecule, $H_2(\nu")$, is very low and comes in the detectable limit only after $P_{RF} > 600W$. Also, the rate of destruction of

142

negative ion should be less than the rate of formation for them to be detectable. At electron temperatures > 4 eV, the rate of destruction increases sharply [129]. This can be seen from figure 7.7. Figure 7.8 shows a comparison between the H^-
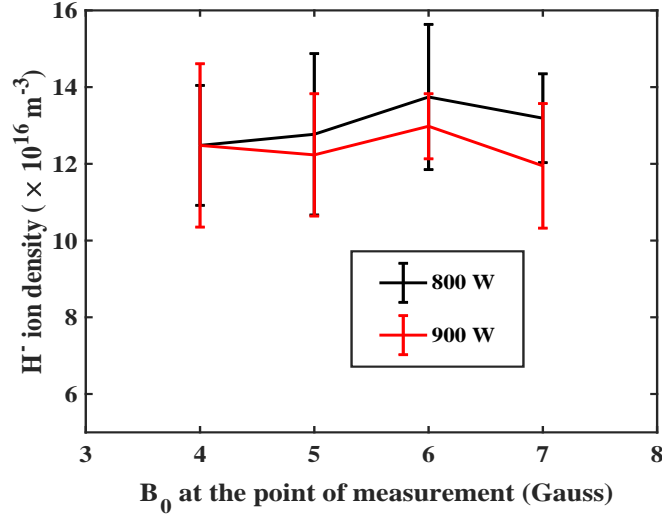
Figure 7.8: Variation of the H^- ion density with dc magnetic field at the location of the measurement ($z = 19$ cm).

density measurement done by CRDS for two different RF power cases. In both of these cases the plasma is helicon wave heated high density plasma with an electron density of $\sim 8 \times 10^{18} m^{-3}$. The OES gives the H^- density in the same order as CRDS in HELEN-I which is $\sim 10^{16} m^{-3}$ at a distance 12 cm from the driver mouth and $z = 19$ cm from the driver backplate.

7.5   Estimating H^- through particle balance

For calculating the H^- ion density through particle balance we take into account the processes primarily contributing to the production of $H_2(\nu")$ molecules and their subsequent conversion to H^- ions through the process of Dissociative attachment. The processes involved in the production of $H_2(\nu")$ are given in table 7.1.

The cross sections of these processes have been taken from [129, 135–137, 144, 145]. The major process responsible for $H_2(\nu")$ formation is the collision of hydrogen molecule with fast electrons (reaction 1 7.1). This process involves the collision of fast electrons ($T_e > 20eV$) with the hydrogen molecule and is denoted by E-V. The cross sections for $H_2(\nu")$ formation through E-V is calculated by Hiskes [137]. For calculating the population of fast electrons we use the electron energy distribution function (EEDF). The electron population is assumed maxwellian and the number of electrons in an energy interval between E and $E + dE$ can be calculated from the expression:

$$n_{dE} = n_e A_1 \int_E^{E+dE} E exp \left(-\frac{\frac{1}{2}mv^2}{E_{th}} \right) \tag{7.6}$$

Here, A_1 is the normalization constant; n_e is the total electron density, E_{th} is the mean thermal energy of the particle distribution and $E = 1/2(mv^2)$ is the kinetic energy of the particles. For the different production and destruction processes to occur in the plasma (equation 7.7) require electrons of different energies to be present in the plasma. For example, EV requires $T_e > 20eV$ and for ionization $T_e \geq 13.6eV$ is required. Therefore, the population of electrons in an energy bin $(E + dE) - E$ is calculated and used in equation 7.7 to obtain the excited population of $H_2(\nu")$ molecules by the electrons in the energy range between E and $E + dE$. The denominator in equation 7.7 contains the $H_2(\nu")$ destruction terms as explained in table 7.3. τ_ν is the life time of $H_2(\nu")$ in the chamber which is $\sim 60\mu s$ for the present experiment. The numerator in above equation contains the terms responsible for $H_2(\nu")$ formation where, f_f is the fraction of high energy electrons involved the the $H_2(\nu")$ formation and is calculated from EEDF. Using different cross section values at different electron temperatures for a given vibrational states and summing over these populations, we can calculate the total density of $H_2(\nu")$ in a given vibrational level $\nu"$. The relation for the

calculation of $H_2(\nu")$ density is given in [76].

$$n_\nu = n_{H_2} \frac{f_f \langle \sigma v \rangle_{EV}}{((1-f_f) \langle \sigma v \rangle_{DA} + f_f (\langle \sigma v \rangle_{Dis} + \langle \sigma v \rangle_{ion})) + \frac{1}{n_e \tau_\nu}} \tag{7.7}$$

This value is used in equation 7.8 to get the negative hydrogen density value. Here, τ_- is the confinement time for H^- ions before getting lost to the walls. Assuming the H^- ion temperature to be $\sim 0.1 eV$, confinement time $\sim 1\mu s$.

$$n_- = n_e \frac{\left[\langle \sigma v \rangle_{dest} + \frac{1}{n_e \tau_-} \right] + \left(\left[\langle \sigma v \rangle_{dest} + \frac{1}{n_e \tau_-} \right]^2 + 4 \langle \sigma v \rangle_{MN} \langle \sigma v \rangle_{DA} \frac{n_\nu}{n_e} \right)^{1/2}}{2 \langle \sigma v \rangle_{MN}} \tag{7.8}$$

where, $\langle \sigma v \rangle_{dest} = \langle \sigma v \rangle_{MN} + \langle \sigma v \rangle_{ED}$ is the total cross section of H^- destruction via ED and MN (table 7.3). τ_- is the life time of the H^- ion in the plasma and is $\sim 10\mu s$ for the our experiment. For incorporating the stripping loss the destruction term $\langle \sigma v \rangle_{dest}$ gets modified.

$$\langle \sigma v \rangle_{dest} = \langle \sigma v \rangle_{MN} + \langle \sigma v \rangle_{ED} + \frac{n_H}{n_e} \langle \sigma v \rangle_{AD} \tag{7.9}$$

where, n_H is the density of neutral hydrogen atoms available and $\langle \sigma v \rangle_{AD}$ stands for the cross section of the associative detachment reaction: $H^- + H(1s) \rightarrow H_2 + e$. The H^- density calculated from equation 7.8 for different pressures is plotted with the experimentally obtained H^- density value obtained from OES in figure 7.9. The equations give a good estimate of the H^- density, which is very close to the values obtained in experiment for lower pressure but deviates from the experiment at high pressure. Although ,the theoretical estimate comes closer to the experimentally obtained value after incorporating the stripping losses due to collision of H^- ion with the neutral hydrogen atoms. Since equations 7.7 and 7.8 only take into account the production and destruction mechanisms at one particular location and not the transport of the species involved (H^-, e, $H_2(\nu")$

and H^+). Therefore, they can only be used to get an estimate of the expected particle density. H^- ions are lost due to diffusion to walls during transport and through the H^- destruction processes described above. A high H^- density in the expansion chamber can be maintained by using a filter field or a slow electron source near the location of interest. It can also be seen from figure 7.9 that the slope of the plot showing $H_2(\nu")$ density is more than the experimentally obtained H^- density plot, predicting that the destruction processes are dominant.
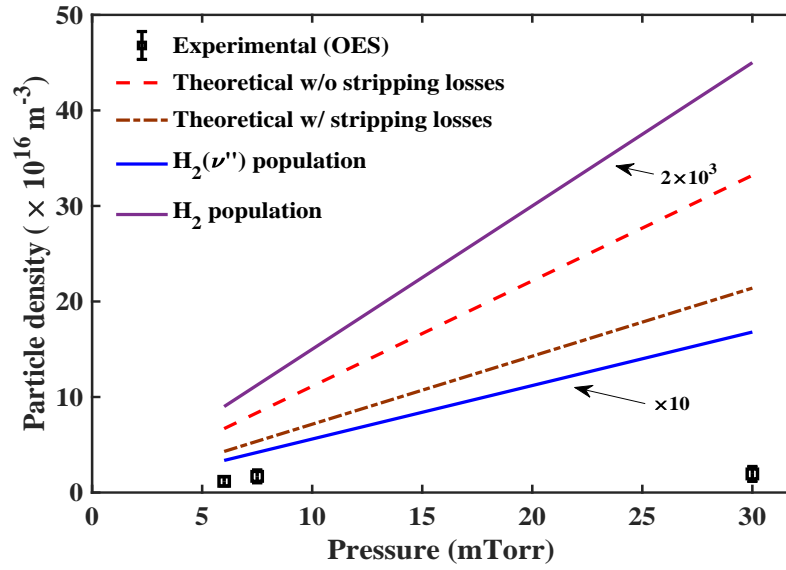
Figure 7.9: The theoretically obtained value for the H^- density is plotted with the experimental values (same as figure 12.b). The H_2 molecule density and the density of vibrationally excited $H_2(\nu")$ molecule are also shown to compare the destruction and generation processes.

7.6 Conclusion

With a very high density hydrogen plasma and an average electron temperature $\sim 5eV$, it is shown through a particle balance model that the expected density of higher vibrational states ($\nu \geq 4$) of hydrogen molecule could be as high as

$10^{17} m^{-3}$. Low energy electrons present in the plasma would interact with these excited molecules to form H^- ions through Dissociative Attachment. In the HE-LEN device, the plasma expands from driver region to expansion region due to the geometry as well as diverging field. This configuration is suitable for electron cooling and maintaining low electron temperatures and high plasma density in the downstream region of the plasma. The line averaged H^- density is measured using two different diagnostic techniques namely, Optical Emission Spectroscopy and Cavity Ring Down Spectroscopy. Laser photo detachment based H^- ion density measurement is under development for local measurement to obtain the H^- ion density profile. A particle balance model based calculation also predicts similar density values considering experimental plasma conditions. The theoretically estimated value matches closely with the OES measurements at low pressures. But at high pressure, the stripping losses become prominent. The stripping losses are due to collisions of H^- ions with H atoms, H_2 molecules, H^{3+} ions and electrons [146]. Here, we have only considered the collisions with H atoms and electrons and we see that the measured value deviates from the theoretically estimated value. Also, due to the reasons mentioned previously in the chapter at pressures higher than 7.5 mTorr, the results obtained from the line ratio method are expected to deviate from the actual value [128]. The production of H^- ions in the system is through volume process, without Caesium (Cs) injection. We are able to obtain a good yield of H^- ions even without the Cs injection or the transverse filter fields. This is due to the temperature gradient achieved due to geometrical and magnetic expansion of plasma in the expansion chamber. In future, Cs injection has to be established in HELEN plasma source. In addition, research with filter fields and low temperature electron sources are planned in HELEN to improve the H^- yield.

8

Conclusion and future scope

The HELEN (**HEL**icon **E**xperiment for **N**egative ion source) device developed during the thesis period is a compact helicon plasma device. It uses a permanent ring magnet for providing axial field and permanent magnets in the expansion chamber for confinement. Generally, the helicon plasma devices are operated with electromagnets for providing the axial field. The use of permanent magnets enables us to make a compact device and drastically reduces the electrical and cooling interfaces and makes the device practically maintenance-free. Among the various applications of a helicon plasma source, we focus here on the ion source application. Heating of fusion plasmas in a tokamak/stellerator by a high energy neutral beam is one of the most efficient ways of heating the ions in a fusion device. The generation of this high energy neutral beam of hydrogen atoms require a hydrogen ion source. This ion source provides the hydrogen ions which can be accelerated to very high energies and then neutralized to provide energetic neutral hydrogen atom beam for Neutral Beam Injection (NBI) into the tokamak. This can be done using either positive hydrogen ions (H^+) or negative hydrogen ions (H^-). But, at high energies ($> 200 keV$) the efficiency of neutralization of H^+ ions drop down drastically, whereas the neutralization of H^- ions give a comparatively high yield (60%) for gas based conventional neutralizer. Moreover, for a good H^- yield high electron densities are needed with low electron temperatures near extraction grid. A helicon plasma in an expanding magnetic field fulfills all these requirements. The results presented in this thesis indicate HELEN configuration is a promising candidate for such a H^- ion source. The HELEN configuration does not have any cooling and electrical connections for magnet systems since it uses permanent magnets

and provides a high H^- yield even without Cs. Through helicon plasma based ion source R&D, Cs-free H^- ion sources might be a reality in coming future.

8.1 Modeling the plasma source

The thesis work had started with a proposed conceptual design based on parametric optimization. The modelling of the source has been carried out using BFieldM for magnetic field profile modelling and HELIC, which is a very useful tool for helicon plasma simulations. From the geometry of the device to the controllable operating parameters leading to the performance estimation was done through HELIC. This provided a preliminary knowledge of the plasma source and its expected performance, which was used to realize the plasma device. A table with the device is given below 8.1.

8.2 Experimental Characterization

The effective RF power coupling to the loop antenna-plasma load was achieved after several modifications in the matching unit. The load and tune capacitance values for a perfectly matched condition vary with the type of gas used and the mode in which the plasma is operating. This variation is due to the change in the impedance of the plasma with gas, power and magnetic field conditions. Only after the perfectly matched condition is established, HELEN is operated. This corresponds to a reflected power of $< 2\%$ during operation.

The experiments are carried out in two stages. In the first stage, the experiments are performed with argon gas. This is essential in order to understand the power coupling to the plasma and benchmarking the helicon wave characteristics considering the relatively more abundant literature available on argon helicon plasmas. The work with hydrogen is carried out in the next stage where a helicon wave heated hydrogen plasma is produced.

8.2.1 Argon plasma characterization

The loop antenna used for the excitation of the $m = 0$ mode successfully generated a high density helicon Argon plasma with the 13.56 MHz source. The first

Table 8.1: Summary table of the device description.

Device Component	Description
Source Chamber	Borosilicate tube. ID = 50 mm. OD ∼ 65 mm. Length = 70 mm.
Expansion Chamber	SS cylinder. ID = 100 mm. OD ∼ 110 mm. Length ∼ 310 mm.
Axial Field Magnet	NdFeB permanent ring magnet ID = 50 mm. OD = 100 mm. Thickness = 25 mm. Surface Field: ∼ 4.7 mT. Location: Above the source chamber.
Cusp Magnets	NdFeB permanent bar magnets, $12 \times 10 \times 2mm^3$ magnets stacked to form a parallelepiped configuration. Location: *see table* 4.1
Loop Antenna	Made of copper tube. OD = 8 mm, ID = 4 mm.
Nagoya Antenna	Made of copper. Total length ∼ 36 mm. Copper strip thickness: ∼ 1.5 mm. Copper strip width: ∼ 8 mm.
Primary Shielding	Made of 0.5 mm thick Aluminium sheet.
Secondary Shielding	Made of 0.3 mm thick SS mesh

signatures of the helicon plasma were seen at 150 W and a stable helicon plasma operation was carried out at 200 W of input rf power. It is shown that a high density argon helicon plasma can be obtained at low rf power for smaller volume devices. In this case the total volume of the device is ~ 2600 cm^{-3} or 2.6 litre.

The wave measurements done by a B-dot probe show the radial wave profile closely matching with the expected profile. The transition from a low to high-density mode is observed in the Argon Plasma as RF power is increased beyond

150W and the density peaking at low magnetic field values.

The confinement by the cusp field configuration helped to achieve high plasma densities in the expansion chamber. An increase by two orders is observed with the confinement magnets. This is due to the reduction in the loss area by 2 orders of magnitude. This result is crucial from the point of view of H^- source development because the H^- yield depends on the availability of low temperature electrons in the expansion chamber.

The results obtained from the theoretical modelling of the plasma using particle balance for non-uniform plasma and power balance equations agree with the temperatures and densities obtained in the experiments.

8.2.2 Hydrogen plasma characterization

After characterization with argon plasma, performance evaluation in hydrogen plasma is carried out to understand its suitability as a hydrogen ion source, specifically as a negative hydrogen ion (H^-) source.

The excitation of helicon wave in hydrogen discharge requires higher electric field strength. The major challenge in exciting the helicon wave in the hydrogen plasma is the low induced field in the plasma by the loop antenna. Therefore, the experiments are carried out using Nagoya-III antenna in place of the loop antenna to ensure better RF electric field coupling. Nagoya antenna excites $m = 1$ helicon mode in the plasma.

The transition from inductively coupled plasma mode to helicon mode is observed in hydrogen (argon) plasma at $P_{RF} \sim 800\text{W}$ (~ 200 W) marked with a sudden rise in plasma density.

In the experiments with hydrogen plasma, an important feature observed is the spatial cooling of electrons when they are moving downstream along the expanding magnetic field. In the expansion chamber, plasma density and temperature gradually decrease. Density goes down from $10^{18} m^{-3}$ in the source chamber to $10^{17} m^{-3}$ in the expansion chamber, whereas the electron temperature goes from $\sim 5eV$ in the source to $< 2eV$ in the expansion. These conditions are conducive to negative hydrogen ion formation.

8.3   Towards H^- ion source

The issues related to the H^- source development mentioned in section 1.4 are addressed in the thesis work and have been discussed below along with the experimental measurements. Volume production of H^- ions is demonstrated in HELEN without the use of Caesium (Cs). Negative hydrogen ion source without the use of Caesium is important for negative ion source research. Operation without Cs ensures minimum maintenance and operational reliability.

It is shown that low electron temperatures can be obtained in the expansion region of the HELEN configuration, whereas the electron temperature near the antenna is higher. This kind of configuration can produce and sustain relatively high H^- densities in the expansion region due to lower destruction of H^- ions.

The negative hydrogen ion density is measured by two independent non-invasive techniques. The first H^- ion diagnostic technique, used for H^- ion density measurement is based on Optical Emission Spectroscopy (OES) method by analyzing the Balmer line ratios, H_α/H_β and H_α/H_γ. The negative ion density values, obtained from the OES are experimentally verified by another diagnostic technique, known as Cavity Ring Down Spectroscopy (CRDS). The measured value of H^- ion density from CRDS is in the order of $10^{16} m^{-3}$ at 6 mTorr pressure, which is close to the density obtained from OES measurements. Both OES and CRDS give the H^- ion density averaged over the line of sight. The measured H^- density is validated with a particle balance model considering experimental plasma conditions. It is shown that even for low pressure operation at 6 mTorr (0.8 Pa) high electron densities and low electron temperatures can be attained. Due to this, a good H^- yield is obtained at these conditions.

It is found that the stripping losses at high pressures do not let the H^- density to increase further and makes it saturate at around $\sim 1.6 \times 10^{16} m^{-3}$. To overcome this issue the production of H^- ions should increase. This can be done by using a low energy electron emitting source or optimising the magnetic field configuration further.

It has been demonstrated in this thesis that a Helicon plasma source is a strong candidate for a negative hydrogen ion source. The main points contributing to the motivation and conclusion has been summarized in the flow chart given in the figure 8.1. It is observed that the helicon plasma supports all the desired

parametric requirements for an efficient H^- ion source (high plasma density, high and low electron temperaures at two different places in the plasma and stable low pressure operation).
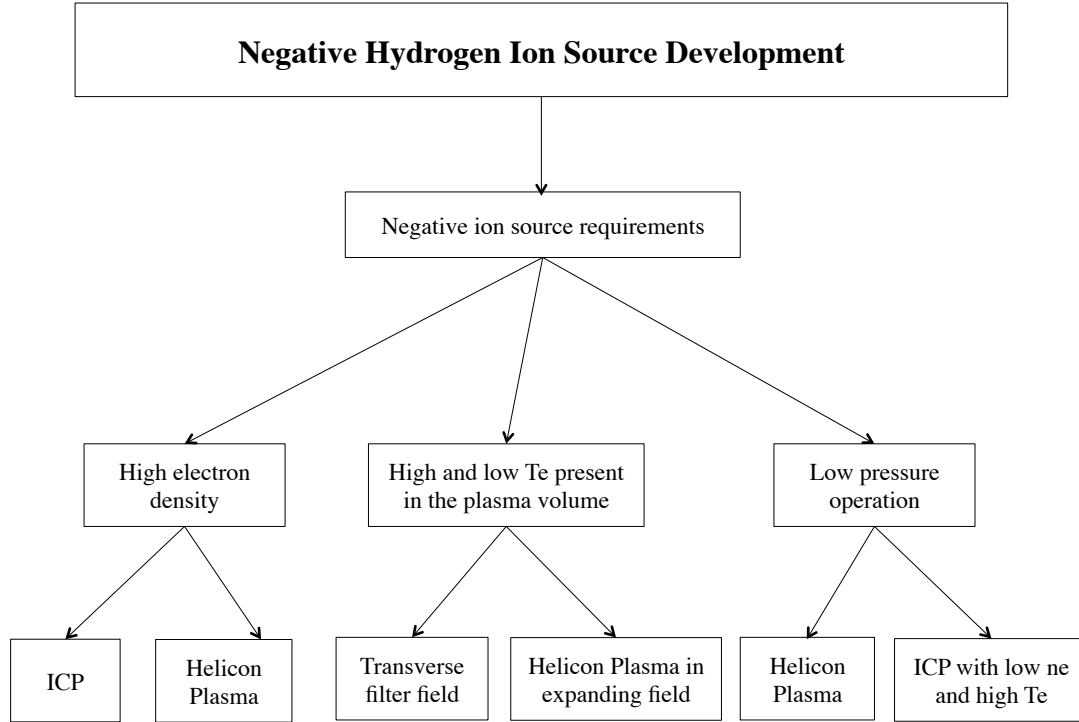
Figure 8.1: Schematic flow chart about the motivation behind choosing the helicon plasma source as a H^- ion source.

8.4 Density rise away from the antenna

In addition to the development and characterization of the device, some interesting obsevation needs further investigation to improve the performance of the device as a H^- ion source. It is observed that, in the source region (near the antenna) the density peaks and decreases downstream as axial length increases Interestingly, the density profile shows another density rise away from the antenna in the expansion chamber accompanied with a rise in the electron temperature at that location.

To understand this phenomenon wave fields are measured using a B-dot probe and based on these measurements a qualitative description of this phenomenon is

presented. Thus, it is seen that the control of wave propagation through magnetic fields in the downstream can be established. The permanent ring magnet, in addition to providing the axial field, can also be used as a control knob for exploring various propagation regimes of the helicon plasma.

The phenomenon is still under investigation due to the fact that expansion chamber will be coupled to the ion source beam extraction system in future. Downstream physics of the device will influence the ion beam characteristics.

8.5 Future Work

Argon Helicon Plasma The perpendicular wave vector of the helicon wave is affected by the magnetic field configuration in the expansion chamber. Table 5.1 shows that the values vary with z non monotonically. Thus, the affect of the existing magnetic field configuration in HELEN on wave propagation in the Argon plasma can be investigated further in this configuration to understand the limitations of the line cusp configuration and then compared with the ring cusp configuration.

Hydrogen Helicon Plasma The density rise away from the antenna poses many questions about wave propagation as well as ion and electron heating in the plasma. The cyclotron heating, the resonance cone heating and electron heating by the standing wave formation are possible around the density rise location. Although there can be different heating modes prevalent for different magnetic field configurations. The question of density rise away from the antenna has to be answered for building a better understanding of such low field helicon sources. This would also serve as an input for identifying the extraction grid location with respect to the antenna.

Localized H^- measurements The OES and CRDS diagnostics used for H^- measurements give the line of sight averaged H^- density. To obtain the local H^- density and H^- density profile in the plasma another Laser Photo Detachment (LPD) diagnostic is under development. It is important to know the equilibrium profile of the H^- ions to efficiently extract a H^- ion beam.

Enhancement of H^- production The H^- ion density obtained thus far is without the use of Caesium. Caseium provides a low work function surface and

increase the H^- density through surface mode of H^- production in addition to the volume processes already happening in the plasma. An electron emitting filament can also be introduced in the downstream region, where H^- ion population need to be higher for extraction. The filament would emit slow electrons into the plasma and facilitate the Dissociative Attachment (DA) process, thus increasing the H^- yield. By employing a magnetic filter field we can also enhance the availability of slow electrons for the DA process.

Beam extraction The next step after the H^- ion formation in the plasma is the beam extraction and its characterization. For this purpose an extraction grid is required to be incorporated into the device and the diagnostics for beam characterization are to be developed.

Multiple helicon drivers For moving towards a large size ion source, the HELEN single driver concept will be extended to multiple drivers connected to a common plasma diffusion volume. But before that, stable high power operation of HELEN device has to be established.

Bibliography

[1] R. S. Hemsworth and T. Inoue, "Positive and negative ion sources for magnetic fusion," *IEEE Transactions on Plasma Science*, vol. 33, pp. 1799–1813, Dec 2005.

[2] R. Agnello, M. Barbisan, I. Furno, P. Guittienne, A. A. Howling, R. Jacquier, R. Pasqualotto, G. Plyushchev, Y. Andrebe, S. Bchu, I. Morgal, and A. Simonin, "Cavity ring-down spectroscopy to measure negative ion density in a helicon plasma source for fusion neutral beams," *Review of Scientific Instruments*, vol. 89, no. 10, p. 103504, 2018.

[3] K. Pandya, A. Gahlaut, R. K. Yadav, M. Bhuyan, M. Bandyopadhyay, B. K. Das, P. Bharathi, M. Vupugalla, K. G. Parmar, H. Tyagi, K. Patel, J. Bhagora, H. Mistri, B. Prajapati, R. Pandey, and A. K. Chakraborty, "First results from negative ion beam extraction in robin in surface mode," *AIP Conference Proceedings*, vol. 1869, no. 1, p. 030009, 2017.

[4] M. Light and F. F. Chen, "Helicon wave excitation with helical antennas," *Physics of Plasmas*, vol. 2, no. 4, pp. 1084–1093, 1995.

[5] F. F. Chen, "Plasma ionization by helicon waves," *Plasma Physics and Controlled Fusion*, vol. 33, no. 4, p. 339, 1991.

[6] R. W. Boswell, "Very efficient plasma generation by whistler waves near the lower hybrid frequency," *Plasma Physics and Controlled Fusion*, vol. 26, no. 10, p. 1147, 1984.

[7] A. J. Perry, D. Vender, and R. W. Boswell, "The application of the helicon source to plasma processing," *Journal of Vacuum Science & Technology B: Microelectronics and Nanometer Structures Processing, Measurement, and Phenomena*, vol. 9, no. 2, pp. 310–317, 1991.

[8] A. Perry, G. Conway, R. Boswell, and H. Persing, "Modulated plasma potentials and cross field diffusion in a helicon plasma," *Physics of Plasmas*, vol. 9, no. 7, pp. 3171–3177, 2002.

[9] S. C. Thakur, C. Brandt, L. Cui, J. J. Gosselin, and G. R. Tynan, "Formation of the blue core in argon helicon plasma," *IEEE Transactions on Plasma Science*, vol. 43, pp. 2754–2759, Aug 2015.

[10] E. T. Everson, P. Pribyl, C. G. Constantin, A. Zylstra, D. Schaeffer, N. L. Kugland, and C. Niemann, "Design, construction, and calibration of a three-axis, high-frequency magnetic probe (b-dot probe) as a diagnostic for exploding plasmas," *Review of Scientific Instruments*, vol. 80, no. 11, p. 113505, 2009.

[11] Y. Takeiri, O. Kaneko, K. Tsumori, Y. Oka, M. Osakabe, K. Ikeda, E. Asano, T. Kawamoto, and R. Akiyama, "Negative hydrogen ion source development for large helical device neutral beam injector (invited)," *Review of Scientific Instruments*, vol. 71, no. 2, pp. 1225–1230, 2000.

[12] R. Boswell, "Plasma production using a standing helicon wave," *Physics Letters A*, vol. 33, pp. 457–458, Dec. 1970.

[13] H. Torreblanca, *Permanent-Magnet Helicon Discharge Array*. PhD thesis, University of California, Berkeley, 2008.

[14] A. Aanesland, A. Meige, and P. Chabert, "Electric propulsion using ion-ion plasmas," *Journal of Physics: Conference Series*, vol. 162, no. 1, p. 012009, 2009.

[15] S. Briefi and U. Fantz, "Investigation of helicon discharges as rf coupling concept of negative hydrogen ion sources," *AIP Conference Proceedings*, vol. 1515, no. 1, pp. 278–283, 2013.

[16] D. Arnush and F. F. Chen, "Generalized theory of helicon waves. ii. excitation and absorption," *Physics of Plasmas*, vol. 5, no. 5, pp. 1239–1254, 1998.

[17] A. W. Molvik, A. R. Ellingboe, and T. D. Rognlien, "Hot-electron production and wave structure in a helicon plasma source," *Phys. Rev. Lett.*, vol. 79, pp. 233–236, Jul 1997.

[18] K. P. Shamrai and V. B. Taranov, "Volume and surface rf power absorption in a helicon plasma source," *Plasma Sources Science and Technology*, vol. 5, no. 3, p. 474, 1996.

[19] A. Simonin, J. Achard, K. Achkasov, S. Bechu, C. Baudouin, O. Baulaigue, C. Blondel, J. Boeuf, D. Bresteau, G. Cartry, W. Chaibi, C. Drag, H. de Esch, D. Fiorucci, G. Fubiani, I. Furno, R. Futtersack, P. Garibaldi, A. Gicquel, C. Grand, P. Guittienne, G. Hagelaar, A. Howling, R. Jacquier, M. Kirkpatrick, D. Lemoine, B. Lepetit, T. Minea, E. Odic, A. Revel, B. Soliman, and P. Teste, "Rd around a photoneutralizer-based nbi system (siphore) in

view of a demo tokamak steady state fusion reactor," *Nuclear Fusion*, vol. 55, no. 12, p. 123020, 2015.

[20] V. F. Virko, Y. V. Virko, V. M. Slobodyan, and K. P. Shamrai, "The effect of magnetic configuration on ion acceleration from a compact helicon source with permanent magnets," *Plasma Sources Science and Technology*, vol. 19, no. 1, p. 015004, 2010.

[21] F. F. Chen and H. Torreblanca, "Large-area helicon plasma source with permanent magnets," *Plasma Physics and Controlled Fusion*, vol. 49, no. 5A, p. A81, 2007.

[22] K. Takahashi, S. Takayama, A. Komuro, and A. Ando, "Standing helicon wave induced by a rapidly bent magnetic field in plasmas," *Phys. Rev. Lett.*, vol. 116, p. 135001, Mar 2016.

[23] C. Charles, "Ion energy distribution functions in a multipole confined argon plasma diffusing from a 13.56 mhz helicon source," *Journal of Vacuum Science & Technology A*, vol. 11, no. 1, pp. 157–163, 1993.

[24] K. Leung, T. Samec, and A. Lamm, "Optimization of permanent magnet plasma confinement," *Physics Letters A*, vol. 51, no. 8, pp. 490 – 492, 1975.

[25] B. D. Blackwell, J. F. Caneses, C. M. Samuell, J. Wach, J. Howard, and C. Corr, "Design and characterization of the magnetized plasma interaction experiment (magpie): a new source for plasma-material interaction studies," *Plasma Sources Science and Technology*, vol. 21, no. 5, p. 055033, 2012.

[26] P. Sonato, P. Agostinetti, U. Fantz, T. Franke, I. Furno, A. Simonin, and M. Q. Tran, "Conceptual design of the beam source for the demo neutral beam injectors," *New Journal of Physics*, vol. 18, no. 12, p. 125002, 2016.

[27] S. T. *J. Vac. Sci. Technol. A*, vol. 19, p. 826, 2001.

[28] S. K. *Thin Solid Films*, vol. 386, p. 243, 2001.

[29] T. G.R. *Phys. Plasmas*, vol. 11, p. 5195, 2004.

[30] B. R.W. *Appl. Phys. Lett.*, vol. 47, p. 1095, 1985.

[31] B. R.W. *J. Appl. Phys.*, vol. 62, p. 3123, 1987.

[32] S. Shinohara, "Helicon high-density plasma sources: physics and applications," *Advances in Physics: X*, vol. 3, no. 1, p. 1420424, 2018.

[33] K. Toki, S. Shinohara, T. Tanikawa, and K. Shamrai, "Small helicon plasma source for electric propulsion," *Thin Solid Films*, vol. 506-507, pp. 597 – 600, 2006. The Joint Meeting of 7th APCPST (Asia Pacific Conference on Plasma Science and Technology) and 17th SPSM (Symposium on Plasma Science for Materials).

[34] W. R. *Phys. Plasmas*, vol. 14, p. 063501, 2007.

[35] C. S.A. *Phys. Plasmas*, vol. 10, p. 2593, 2003.

[36] W. L.T. *Plasma Sources Sci. Technol.*, vol. 22, p. 055019, 2013.

[37] S. S. *IEEE Trans. Plasma Sci.*, vol. 42, p. 1245, 2014.

[38] U. A. *IEEE Trans. Plasma. Sci.*, vol. 44, p. 306, 2016.

[39] M. J. Singh, D. Boilson, A. R. Polevoi, T. Oikawa, and R. Mitteau, "Heating neutral beams for iter: negative ion sources to tune fusion plasmas," *New Journal of Physics*, vol. 19, no. 5, p. 055004, 2017.

[40] E. Speth, "Neutral beam heating of fusion plasmas," *Reports on Progress in Physics*, vol. 52, no. 1, p. 57, 1989.

[41] D. Faircloth and S. Lawrie, "An overview of negative hydrogen ion sources for accelerators," *New Journal of Physics*, vol. 20, no. 2, p. 025007, 2018.

[42] E. Speth, H. Falter, P. Franzen, U. Fantz, M. Bandyopadhyay, S. Christ, A. Encheva, M. FrÃűschle, D. Holtum, B. Heinemann, W. Kraus, A. Lorenz, C. Martens, P. McNeely, S. Obermayer, R. Riedl, R. SÃijss, A. Tanga, R. Wilhelm, and D. WÃijnderlich, "Overview of the rf source development programme at ipp garching," *Nuclear Fusion*, vol. 46, no. 6, p. S220, 2006.

[43] R. S. Hemsworth, A. Tanga, and V. Antoni, "Status of the iter neutral beam injection system (invited)," *Review of Scientific Instruments*, vol. 79, no. 2, p. 02C109, 2008.

[44] D. Wnderlich, W. Kraus, M. Frschle, R. Riedl, U. Fantz, and B. Heinemann, "Long pulse, high power operation of the elise test facility," *AIP Conference Proceedings*, vol. 1869, no. 1, p. 030003, 2017.

[45] D. WÃijnderlich, U. Fantz, B. Heinemann, W. Kraus, R. Riedl, C. Wimmer, and the NNBI Team, "Progress of the elise test facility: towards one hour pulses in hydrogen," *Nuclear Fusion*, vol. 56, no. 10, p. 106004, 2016.

[46] P. S. et al., "Design of the mitica neutral beam injector: from physics analysis to engineering design," Tech. Rep. ITR/1-3, ITER, 2012.

[47] J. Santoso, R. Manoharan, S. O'Byrne, and C. S. Corr, "Negative hydrogen ion production in a helicon plasma source," *Physics of Plasmas*, vol. 22, no. 9, p. 093513, 2015.

[48] A. Chakraborty, C. Rotti, M. Bandyopadhyay, M. J. Singh, R. G. Nair, S. Shah, U. K. Baruah, R. S. Hemsworth, and B. Schunke, "Diagnostic neutral beam for iter-concept to engineering," *IEEE Transactions on Plasma Science*, vol. 38, pp. 248–253, March 2010.

[49] G. Bansal, A. Gahlaut, J. Soni, K. Pandya, K. G. Parmar, R. Pandey, M. Vuppugalla, B. Prajapati, A. Patel, H. Mistery, A. Chakraborty, M. Bandyopadhyay, M. J. Singh, A. Phukan, R. K. Yadav, and D. Parmar, "Negative ion beam extraction in robin," *Fusion Engineering and Design*, vol. 88, no. 6, pp. 778 – 782, 2013. Proceedings of the 27th Symposium On Fusion Technology (SOFT-27); Liège, Belgium, September 24-28, 2012.

[50] M. Bandyopadhyay, M. J. Singh, G. Bansal, A. Gahlaut, K. Pandya, K. G. Parmar, J. Soni, I. Ahmed, G. Roopesh, C. Rotti, S. Shah, A. Phukan, R. K. Yadav, and A. K. Chakraborty, "Two-rf-driver-based negative ion source for fusion r amp;amp;d," *IEEE Transactions on Plasma Science*, vol. 40, pp. 2767–2772, Oct 2012.

[51] M. Bandyopadhyay, R. Pandey, S. Shah, G. Bansal, D. Parmar, A. Gahlaut, J. Soni, R. Yadav, D. Sudhir, H. Tyagi, K. Pandya, K. G. Parmar, H. S. Mistri, M. Vuppugalla, and A. K. Chakraborty, "Two rf driver-based negative ion source experiment," *IEEE Transactions on Plasma Science*, vol. 42, pp. 624–627, March 2014.

[52] M. Bandyopadhyay, M. J. Singh, C. Rotti, A. Chakraborty, R. S. Hemsworth, and B. Schunke, "Beamline optimization for 100-kev diagnostic neutral beam injector for iter," *IEEE Transactions on Plasma Science*, vol. 38, pp. 242–247, March 2010.

[53] S. Gammino, L. Celona, G. Ciavola, F. Maimone, and D. Mascali, "Review on high current 2.45 ghz electron cyclotron resonance sources (invited)," *Review of Scientific Instruments*, vol. 81, no. 2, p. 02B313, 2010.

[54] G. Castro, D. Mascali, S. Gammino, G. Torrisi, F. P. Romano, L. Celona, C. Altana, C. Caliri, N. Gambino, D. Lanaia, R. Miracoli, L. Neri, and G. Sorbello, "Overdense plasma generation in a compact ion source," *Plasma Sources Science and Technology*, vol. 26, no. 5, p. 055019, 2017.

[55] R. D. Tarey, A. Ganguli, D. Sahu, R. Narayanan, and N. Arora, "Studies on plasma production in a large volume system using multiple compact ecr plasma sources," *Plasma Sources Science and Technology*, vol. 26, no. 1, p. 015009, 2017.

[56] S. Tada, W. Miyazawa, Y. Sakamoto, S. Den, and Y. Hayashi, "A rectangular large ecr plasma source," *Thin Solid Films*, vol. 281-282, pp. 149 – 151, 1996.

[57] A. Ganguli, R. D. Tarey, N. Arora, and R. Narayanan, "Development and studies on a compact electron cyclotron resonance plasma source," *Plasma Sources Science and Technology*, vol. 25, no. 2, p. 025026, 2016.

[58] Z. Q. Xie, "Production of highly charged ion beams from electron cyclotron resonance ion sources (invited)," *Review of Scientific Instruments*, vol. 69, no. 2, pp. 625–630, 1998.

[59] M. Moisan and Z. Zakrzewski, "New surface wave launchers for sustaining plasma columns at submicrowave frequencies (1âĂŞ300 mhz)," *Review of Scientific Instruments*, vol. 58, no. 10, pp. 1895–1900, 1987.

[60] C. Moutoulas, M. Moisan, L. Bertrand, J. Hubert, J. L. Lachambre, and A. Ricard, "A highâĂŘfrequency surface wave pumped heâĂŘne laser," *Applied Physics Letters*, vol. 46, no. 4, pp. 323–325, 1985.

[61] D. T. Tuma, "A quiet uniform microwave gas discharge for lasers," *Review of Scientific Instruments*, vol. 41, no. 10, pp. 1519–1520, 1970.

[62] M. Moisan, C. Beaudry, and P. Lepprince, "A new hf device for the production of long plasma columns at a high electron density," *Physics Letters A*, vol. 50, no. 2, pp. 125 – 126, 1974.

[63] Z. Zakrzewski, M. Moisan, V. M. M. Glaude, C. Beaudry, and P. Leprince, "Attenuation of a surface wave in an unmagnetized rf plasma column," *Plasma Physics*, vol. 19, no. 2, p. 77, 1977.

[64] M. Chaker and M. Moisan, "LargeâĂŘdiameter plasma columns produced by surface waves at radio and microwave frequencies," *Journal of Applied Physics*, vol. 57, no. 1, pp. 91–95, 1985.

162

[65] Y. M. Aliev, K. M. Ivanova, M. Moisan, and A. P. Shivarova, "Analytical expressions for the axial structure of surface wave sustained plasmas under various regimes of charged particle loss," *Plasma Sources Science and Technology*, vol. 2, no. 3, p. 145, 1993.

[66] M. Moisan and Z. Zakrzewski, "Plasma sources based on the propagation of electromagnetic surface waves," *Journal of Physics D: Applied Physics*, vol. 24, no. 7, p. 1025, 1991.

[67] E. E. Kunhardt and L. H. Luessen, eds., *Electrical Breakdown and Discharges in Gases.* No. 9781468444117, NATO ASI Series, 1983.

[68] M. Moisan and Z. Zakrzewski, *Radiative Processes in Discharge Plasmas*, vol. 149 of *NATO ASI Series B: Physics.* New York:Plenum, 1982.

[69] Moisan, M., Ferreira, C.M., Hajlaoui, Y., Henry, D., Hubert, J., Pantel, R., Ricard, A., and Zakrzewski, Z., "Properties and applications of surface wave produced plasmas," *Rev. Phys. Appl. (Paris)*, vol. 17, no. 11, pp. 707–727, 1982.

[70] M. Chaker, M. Moisan, and Z. Zakrzewski, "Microwave and rf surface wave sustained discharges as plasma sources for plasma chemistry and plasma processing," *Plasma Chemistry and Plasma Processing*, vol. 6, pp. 79–96, Mar 1986.

[71] J. Hopwood, "Review of inductively coupled plasmas for plasma processing," *Plasma Sources Science and Technology*, vol. 1, no. 2, p. 109, 1992.

[72] W. Kraus, M. Bandyopadhyay, H. Falter, P. Franzen, B. Heinemann, P. Mc-Neely, R. Riedl, E. Speth, A. Tanga, and R. Wilhelm, "Progress in the development of rf driven h^-/d^- sources for neutral beam injection," *Review of Scientific Instruments*, vol. 75, no. 5, pp. 1832–1834, 2004.

[73] M. D. Palma, S. D. Bello, F. Fellin, and P. Zaccaria, "Design of a cooling system for the iter ion source and neutral beam test facilities," *Fusion Engineering and Design*, vol. 84, no. 7, pp. 1460 – 1464, 2009. Proceeding of the 25th Symposium on Fusion Technology.

[74] F. F. Chen, J. D. Evans, and G. R. Tynan, "Design and performance of distributed helicon sources," *Plasma Sources Science and Technology*, vol. 10, no. 2, p. 236, 2001.

[75] D. Marcuzzi, M. D. Palma, M. Pavei, B. Heinemann, W. Kraus, and R. Riedl, "Detailed design of the rf source for the 1mv neutral beam test facility," *Fusion Engineering and Design*, vol. 84, no. 7, pp. 1253 – 1258, 2009. Proceeding of the 25th Symposium on Fusion Technology.

[76] M. Bandyopadhyay, *Studies of an inductively coupled negative hydrogen ion radio frequency source through simulations and experiments*. PhD thesis, Max-Planck-Institut für Plasmaphysik, Garching, Germany, Garching, Germany, July 2004.

[77] B. H., "Zwei mit der hilfe der neuen verstarker entdeckte erscheinungen," *Physik Z.*, vol. 20, no. 401, 1919.

[78] "An investigation of whistling atmospherics," *Philosophical Transactions of the Royal Society of London A: Mathematical, Physical and Engineering Sciences*, vol. 246, no. 908, pp. 113–141, 1953.

[79] L. C. Woods, "On the boundary conditions at an insulating wall for hydromagnetic waves in a cylindrical plasma," *Journal of Fluid Mechanics*, vol. 18, no. 3, pp. 401–408, 1964.

[80] J. P. Klozenberg, B. McNamara, and P. C. Thonemann, "The dispersion and attenuation of helicon waves in a uniform cylindrical plasma," *Journal of Fluid Mechanics*, vol. 21, no. 3, pp. 545–563, 1965.

[81] B. Davies and P. J. Christiansen, "Helicon waves in a gaseous plasma," *Plasma Physics*, vol. 11, no. 12, p. 987, 1969.

[82] B. Davies, "Helicon wave propagation: effect of electron inertia," *Journal of Plasma Physics*, vol. 4, no. 1, pp. 43–50, 1970.

[83] F. F. Chen and D. Arnush, "Generalized theory of helicon waves. i. normal modes," *Physics of Plasmas*, vol. 4, no. 9, pp. 3411–3421, 1997.

[84] S. Harada, T. Baba, A. Uchigashima, S. Yokota, A. Iwakawa, A. Sasoh, T. Yamazaki, and H. Shimizu, "Electrostatic acceleration of helicon plasma using a cusped magnetic field," *Applied Physics Letters*, vol. 105, no. 19, p. 194101, 2014.

[85] E. Åström, "Magneto-hydrodynamic waves in a plasma," *Nature*, vol. 165, pp. 1019 EP –, 06 1950.

[86] A. Sitenko and K. Stepanov, "On the oscillations of an electron plasma in a magnetic field," *Soviet Phys. JETP*.

164

[87] E. Åström, "On waves in an ionized gas," *Arkiv Fysik*, vol. 2, no. 443, 1950.

[88] T. H. Stix, *Waves In Plasmas*. 978-0-88318-859-0, AIP-Press, 1 ed., 1992.

[89] A. W. Degeling, G. G. Borg, and R. W. Boswell, "Transitions from electrostatic to electromagnetic whistler wave excitation," *Physics of Plasmas*, vol. 11, no. 5, pp. 2144–2155, 2004.

[90] R. K. Fisher and R. W. Gould, "Resonance cones in the field pattern of a radio frequency probe in a warm anisotropic plasma," *The Physics of Fluids*, vol. 14, no. 4, pp. 857–867, 1971.

[91] V. V. Nazarov, M. V. Starodubtsev, and A. V. Kostrov, "Laboratory studies of the dynamic of resonance cones formation in magnetized plasmas," *Physics of Plasmas*, vol. 20, no. 3, p. 032110, 2013.

[92] P. K. Chattopadhyay, K. K. Barada, J. Ghosh, D. Sharma, and Y. C. Saxena, "Study of density peaking in a diverging magnetic field helicon experiment," *AIP Conference Proceedings*, vol. 1582, no. 1, pp. 251–260, 2014.

[93] A. Pandey, D. Sudhir, M. Bandyopadhyay, and A. Chakraborty, "Conceptual design of a permanent ring magnet based helicon plasma source module intended to be used in a large size fusion grade ion source," *Fusion Engineering and Design*, vol. 103, pp. 1 – 7, 2016.

[94] D. Arnush, "The role of trivelpiece-gould waves in antenna coupling to helicon waves," *Physics of Plasmas*, vol. 7, no. 7, pp. 3042–3050, 2000.

[95] F. F. Chen, "Antenna mechanisms and electrostatic fields in helicon discharges," report, ltp 1212, UCLA, Dec, 2012.

[96] D. Curreli and F. F. Chen, "Equilibrium theory of cylindrical discharges with special application to helicons," *Physics of Plasmas*, vol. 18, no. 11, p. 113501, 2011.

[97] F. F. Chen, X. Jiang, J. D. Evans, G. Tynan, and D. Arnush, "Low-field helicon discharges," *Plasma Physics and Controlled Fusion*, vol. 39, no. 5A, p. A411, 1997.

[98] I. V. Kamenski and G. G. Borg, "An evaluation of different antenna designs for helicon wave excitation in a cylindrical plasma source," *Physics of Plasmas*, vol. 3, no. 12, pp. 4396–4409, 1996.

[99] D. Melazzi and V. Lancellotti, "A comparative study of radiofrequency antennas for helicon plasma sources," *Plasma Sources Science and Technology*, vol. 24, no. 2, p. 025024, 2015.

[100] K. P. Shamrai, "Stable modes and abrupt density jumps in a helicon plasma source," *Plasma Sources Science and Technology*, vol. 7, no. 4, p. 499, 1998.

[101] Y. Sakawa, N. Koshikawa, and T. Shoji, "Characteristics of the high density plasma production by m=0 helicon wave," *Applied Physics Letters*, vol. 69, no. 12, pp. 1695–1697, 1996.

[102] J. P. Sheehan and N. Hershkowitz, "Emissive probes," *Plasma Sources Science and Technology*, vol. 20, no. 6, p. 063001, 2011.

[103] R. F. Kemp and J. M. Sellen, "Plasma potential measurements by electron emissive probes," *Review of Scientific Instruments*, vol. 37, no. 4, pp. 455–461, 1966.

[104] J. R. Smith, N. Hershkowitz, and P. Coakley, "Inflection point method of interpreting emissive probe characteristics," *Review of Scientific Instruments*, vol. 50, no. 2, pp. 210–218, 1979.

[105] V. A. Godyak and R. B. Piejak, "Probe measurements of the space potential in a radio frequency discharge," *Journal of Applied Physics*, vol. 68, no. 7, pp. 3157–3162, 1990.

[106] M. A. Sobolewski, J. K. Olthoff, and Y. Wang, "Ion energy distributions and sheath voltages in a radio-frequency-biased, inductively coupled, high-density plasma reactor," *Journal of Applied Physics*, vol. 85, no. 8, pp. 3966–3975, 1999.

[107] D. Vender and R. W. Boswell, "Electron sheath interaction in capacitive radio-frequency plasmas," *Journal of Vacuum Science & Technology A*, vol. 10, no. 4, pp. 1331–1338, 1992.

[108] M. Y. Ye and S. Takamura, "Effect of space-charge limited emission on measurements of plasma potential using emissive probes," *Physics of Plasmas*, vol. 7, no. 8, pp. 3457–3463, 2000.

[109] S.-L. Chen and T. Sekiguchi, "Instantaneous direct-display system of plasma parameters by means of triple probe," *Journal of Applied Physics*, vol. 36, no. 8, pp. 2363–2375, 1965.

[110] A. Pandey, M. Bandyopadhyay, D. Sudhir, and A. Chakraborty, "Performance evaluation of a permanent ring magnet based helicon plasma source for negative ion source research," *Review of Scientific Instruments*, vol. 88, no. 10, p. 103509, 2017.

[111] V. T. et al., "Progress in the realization of the prima neutral beam test facility," *Nuclear Fusion*, vol. 55, no. 8, p. 083025, 2015.

[112] M. Hanada, A. Kojima, T. Inoue, K. Watanabe, M. Taniguchi, M. Kashiwagi, H. Tobari, N. Umeda, N. Akino, M. Kazawa, K. Oasa, M. Komata, K. Usui, K. Mogaki, S. Sasaki, K. Kikuchi, S. Nemoto, K. Ohshima, Y. Endo, T. Simizu, N. Kubo, M. Kawai, and L. R. Grisham, "Development of the jt-60sa neutral beam injectors," *AIP Conference Proceedings*, vol. 1390, no. 1, pp. 536–544, 2011.

[113] W. Jianglong, X. Yahong, L. Lizhen, G. Yuming, Y. Wei, L. Jun, H. Chundong, X. Yuanlai, J. Caichao, T. Ling, S. Peng, and X. Yongjian, "Design of the prototype negative ion source for neutral beam injector at asipp," *Plasma Science and Technology*, vol. 18, no. 9, p. 954, 2016.

[114] Y. Belchenko, G. Abdrashitov, P. Deichuli, A. Ivanov, A. Gorbovsky, A. Kondakov, A. Sanin, O. Sotnikov, and I. Shikhovtsev, "Inductively driven surface-plasma negative ion source for n-nbi use (invited)," *Review of Scientific Instruments*, vol. 87, no. 2, p. 02B316, 2016.

[115] K.-K. Chi, T. E. Sheridan, and R. W. Boswell, "Resonant cavity modes of a bounded helicon discharge," *Plasma Sources Science and Technology*, vol. 8, no. 3, p. 421, 1999.

[116] C. M. Franck, O. Grulke, and T. Klinger, "Mode transitions in helicon discharges," *Physics of Plasmas*, vol. 10, no. 1, pp. 323–325, 2003.

[117] M. A. Lieberman and A. J. Lichtenberg, *Principles of Plasma Discharges and Materials Processing*. Wiley, NJ, 2 ed., 2005.

[118] T. M. Philip, "Computation of rate coefficients for electron impact collisions," Tech. Rep. Memorandum No. UCB/ERL M98/43, Electron Research Laboratory, University of California, Berkeley, 1998.

[119] A. Simon, "Ambipolar diffusion in a magnetic field," *Phys. Rev.*, vol. 98, pp. 317–318, Apr 1955.

[120] V. Vahedi, *MODELING AND SIMULATION OF RF DISCHARGES USED FOR PLASMA PROCESSING*. PhD thesis, University of California, Berkeley, 1993.

[121] I. D. Sudit and F. F. Chen, "Discharge equilibrium of a helicon plasma," *Plasma Sources Science and Technology*, vol. 5, no. 1, p. 43, 1996.

[122] A. Pandey, D. Mukherjee, M. Bandyopadhyay, D. Borah, H. Tyagi, R. Yadav, and A. Chakraborty, "Characterization of hydrogen plasma in a permanent ring magnet based helicon plasma source for negative ion source research," *arXiv e-prints*, p. arXiv:1811.12311, Nov. 2018.

[123] Y. S. K. Hideki and T. Shoji, "Hydrogen plasma production in the lower-hybrid frequency range," *J. Plasma Fusion Res. Ser.*, vol. 5, pp. 302–305, 2002.

[124] K. P. Shamrai, V. P. Pavlenko, and V. B. Taranov, "Excitation, conversion and damping of waves in a helicon plasma source driven by an m = 0 antenna," *Plasma Physics and Controlled Fusion*, vol. 39, no. 3, p. 505, 1997.

[125] S. Takechi, S. Shinohara, and Y. Kawai, "Effects of cusp magnetic field configuration on wave propagation in large diameter r.f. produced plasma," *Surface and Coatings Technology*, vol. 112, no. 1, pp. 15 – 19, 1999.

[126] S. Ghosh, K. K. Barada, P. K. Chattopadhyay, J. Ghosh, and D. Bora, "Localized electron heating and density peaking in downstream helicon plasma," *Plasma Sources Science and Technology*, vol. 24, no. 3, p. 034011, 2015.

[127] F. F. Chen, *Introduction to Plasma Physics and Controlled Fusion*, vol. 1. Springer Science+Business Media New York: Springer US, 2 ed., 1984.

[128] U. Fantz and D. Wünderlich, "A novel diagnostic technique for h^- (d^-) densities in negative hydrogen ion sources," *New Journal of Physics*, vol. 8, no. 12, p. 301, 2006.

[129] M. Bacal and M. Wada, "Negative hydrogen ion production mechanisms," *Applied Physics Reviews*, vol. 2, no. 2, p. 021305, 2015.

[130] B. Kakati, S. S. Kausik, M. Bandyopadhyay, B. K. Saikia, and P. K. Kaw, "Development of a novel surface assisted volume negative hydrogen ion source," *Scientific Reports*, vol. 7, no. 1, p. 11078, 2017.

[131] K. Takahashi, C. Charles, R. Boswell, and A. Ando, "Adiabatic expansion of electron gas in a magnetic nozzle," *Phys. Rev. Lett.*, vol. 120, p. 045001, Jan 2018.

[132] J. M. Little and E. Y. Choueiri, "Electron cooling in a magnetically expanding plasma," *Phys. Rev. Lett.*, vol. 117, p. 225003, Nov 2016.

[133] M. B. E. Nicolopoulou and H. Doucet, "Equilibrium density of h- in a low pressure hydrogen plasma," *J. Phys. France*, vol. 38, no. 11, pp. 1399–1404, 1977.

[134] M. Bacal and G. W. Hamilton, "h$^-$ and d$^-$ production in plasmas," *Phys. Rev. Lett.*, vol. 42, pp. 1538–1540, Jun 1979.

[135] C. Bottcher and B. D. Buckley, "Dissociative electron attachment to the metastable c 3 pi u state of molecular hydrogen," *Journal of Physics B: Atomic and Molecular Physics*, vol. 12, no. 16, p. L497, 1979.

[136] J. M. Wadehra and J. N. Bardsley, "Vibrational- and rotational-state dependence of dissociative attachment in e-h$_2$ collisions," *Phys. Rev. Lett.*, vol. 41, pp. 1795–1798, Dec 1978.

[137] J. R. Hiskes, "Cross sections for the vibrational excitation of the $h_2x^1\sigma^+$g(v) levels generated by electron collisional excitation of the higher singlet states," *Journal of Applied Physics*, vol. 70, no. 7, pp. 3409–3417, 1991.

[138] H. P. Summers, W. J. Dickson, M. G. O'Mullane, N. R. Badnell, A. D. Whiteford, D. H. Brooks, J. Lang, S. D. Loch, and D. C. Griffin, "Ionization state, excited populations and emission of impurities in dynamic finite density plasmas: I. the generalized collisional-radiative model for light elements," *Plasma Physics and Controlled Fusion*, vol. 48, no. 2, p. 263.

[139] A. O'Keefe and D. A. G. Deacon, "Cavity ring-down optical spectrometer for absorption measurements using pulsed laser sources," *Review of Scientific Instruments*, vol. 59, no. 12, pp. 2544–2551, 1988.

[140] H. Nakano, K. Tsumori, M. Shibuya, S. Geng, M. Kisaki, K. Ikeda, K. Nagaoka, M. Osakabe, Y. Takeiri, and O. Kaneko, "Cavity ringdown technique for negative-hydrogen-ion measurement in ion source for neutral beam injector," *Journal of Instrumentation*, vol. 11, no. 03, p. C03018, 2016.

[141] F. Grangeon, C. Monard, J.-L. Dorier, A. A. Howling, C. Hollenstein, D. Romanini, and N. Sadeghi, "Applications of the cavity ring-down technique to a

large-area rf-plasma reactor," *Plasma Sources Science and Technology*, vol. 8, no. 3, p. 448, 1999.

[142] S. Chakraborty Thakur, D. McCarren, J. Carr, and E. E. Scime, "Continuous wave cavity ring down spectroscopy measurements of velocity distribution functions of argon ions in a helicon plasma," *Review of Scientific Instruments*, vol. 83, no. 2, p. 023508, 2012.

[143] D. M. et al., "Negative hydrogen ion density measurement in a permanent magnet based helicon ion source (helen-i) by cavity ring down spectroscopy," *To be submitted.*

[144] J. R. Hiskes, "Cross sections for the vibrational excitation of the h_2 $(x^1 \ \sigma_g^+)$ state via electron collisional excitation of the higher singlet states," *Journal of Applied Physics*, vol. 51, no. 9, pp. 4592–4594, 1980.

[145] J. M. Wadehra, "Dissociative attachment to rovibrationally excited h_2," *Phys. Rev. A*, vol. 29, pp. 106–110, Jan 1984.

[146] R. K. Janev, D. Reiter, and U. Samm, "Collision processes in low-temperature hydrogen plasmas," tech. rep., Germany, 2003.

[147] T. Lafleur, C. Charles, and R. W. Boswell, "Plasma control by modification of helicon wave propagation in low magnetic fields," *Physics of Plasmas*, vol. 17, no. 7, p. 073508, 2010.

[148] F. F. Chen and R. W. Boswell, "Helicons-the past decade," *IEEE Transactions on Plasma Science*, vol. 25, pp. 1245–1257, Dec 1997.

[149] "Instruction for bfieldm program."

[150] A. W. Degeling and R. W. Boswell, "Modeling ionization by helicon waves," *Physics of Plasmas*, vol. 4, no. 7, pp. 2748–2755, 1997.

[151] B. B. Sahu, A. Ganguli, and R. D. Tarey, "Warm electrons are responsible for helicon plasma production," *Plasma Sources Science and Technology*, vol. 23, no. 6, p. 065050, 2014.

[152] F. F. Chen and H. Torreblanca, "Density jump in helicon discharges," *Plasma Sources Science and Technology*, vol. 16, no. 3, p. 593, 2007.

[153] F. F. Chen, "Helicon discharges and sources: a review," *Plasma Sources Science and Technology*, vol. 24, no. 1, p. 014001, 2015.

170

[154] N. B. Pascal Chabert, *Physics of Radio-Frequency Plasmas.* No. 9780521763004, Cambridge University Press, April, 2011.

[155] F. F. Chen and D. D. Blackwell, "Upper limit to landau damping in helicon discharges," *Phys. Rev. Lett.*, vol. 82, pp. 2677–2680, Mar 1999.

[156] D. D. Blackwell, T. G. Madziwa, D. Arnush, and F. F. Chen, "Evidence for trivelpiece-gould modes in a helicon discharge," *Phys. Rev. Lett.*, vol. 88, p. 145002, Mar 2002.

[157] P. McNeely, H.-D. Falter, U. Fantz, P. Franzen, M. FrÃűschle, B. Heinemann, W. Kraus, C. Martens, R. Riedl, and E. Speth, "Development of a rf negative-ion source for iter neutral beam injection," *Review of Scientific Instruments*, vol. 77, no. 3, p. 03A519, 2006.

[158] M. J. Singh, M. Bandyopadhyay, G. Bansal, A. Gahlaut, J. Soni, S. Kumar, K. Pandya, K. G. Parmar, J. Sonara, R. Yadava, A. K. Chakraborty, W. Kraus, B. Heinemann, R. Riedl, S. Obermayer, C. Martens, P. Franzen, and U. Fantz, "Rf plasma source commissioning in indian negative ion facility," *AIP Conference Proceedings*, vol. 1390, no. 1, pp. 604–613, 2011.

[159] M. Bandyopadhyay, I. Ahmed, G. Roopesh, M. Singh, C. Rotti, S. Shah, A. Phukan, R. Yadav, and A. Chakraborty, "Iter dnb ion source movement mechanism," *Fusion Engineering and Design*, vol. 86, no. 6, pp. 864 – 867, 2011. Proceedings of the 26th Symposium of Fusion Technology (SOFT-26).

[160] M. Singh, M. Bandyopadhyay, C. Rotti, N. Singh, S. Shah, G. Bansal, A. Gahlaut, J. Soni, H. Lakdawala, H. Waghela, I. Ahmed, G. Roopesh, U. Baruah, and A. Chakraborty, "An indian test facility to characterise diagnostic neutral beam for iter," *Fusion Engineering and Design*, vol. 86, no. 6, pp. 732 – 735, 2011. Proceedings of the 26th Symposium of Fusion Technology (SOFT-26).

[161] M. Bandyopadhyay, R. Pandey, S. Shah, G. Bansal, D. Parmar, A. Gahlaut, J. Soni, R. Yadav, D. Sudhir, H. Tyagi, K. Pandya, K. G. Parmar, H. S. Mistri, M. Vuppugalla, and A. K. Chakraborty, "Two rf driver-based negative ion source experiment," *IEEE Transactions on Plasma Science*, vol. 42, pp. 624–627, March 2014.

[162] M. Bandyopadhyay, M. J. Singh, C. Rotti, A. Chakraborty, R. S. Hemsworth, and B. Schunke, "Beamline optimization for 100-kev diagnostic neutral beam

injector for iter," *IEEE Transactions on Plasma Science*, vol. 38, pp. 242–247, March 2010.

[163] M. Light, I. D. Sudit, F. F. Chen, and D. Arnush, "Axial propagation of helicon waves," *Physics of Plasmas*, vol. 2, no. 11, pp. 4094–4103, 1995.

[164] S. Shinohara and K. Yonekura, "Discharge modes and wave structures using loop antennae in a helicon plasma source," *Plasma Physics and Controlled Fusion*, vol. 42, no. 1, p. 41, 2000.

[165] R. I. Pinsker, "Whistlers, helicons, and lower hybrid waves: The physics of radio frequency wave propagation and absorption for current drive via landau damping," *Physics of Plasmas*, vol. 22, no. 9, p. 090901, 2015.

[166] K. Shamrai and V. Taranov, "Resonances and anti-resonances of a plasma column in a helicon plasma source," *Physics Letters A*, vol. 204, no. 2, pp. 139 – 145, 1995.

[167] R. Hemsworth, H. Decamps, J. Graceffa, B. Schunke, M. Tanaka, M. Dremel, A. Tanga, H. D. Esch, F. Geli, J. Milnes, T. Inoue, D. Marcuzzi, P. Sonato, and P. Zaccaria, "Status of the iter heating neutral beam system," *Nuclear Fusion*, vol. 49, no. 4, p. 045006, 2009.

[168] K. K. Barada, P. K. Chattopadhyay, J. Ghosh, S. Kumar, and Y. C. Saxena, "Observation of low magnetic field density peaks in helicon plasma," *Physics of Plasmas*, vol. 20, no. 4, p. 042119, 2013.

[169] M. Bacal, C. Michaut, L. I. Elizarov, and F. El Balghiti, "Basic processes of negative hydrogen ion production and destruction in sources and beams (invited)," *Review of Scientific Instruments*, vol. 67, no. 3, pp. 1138–1143, 1996.

[170] A. G. Nikitin, F. E. Balghiti, and M. Bacal, "Comparison of negative ion density measurements by probes and by photodetachment," *Plasma Sources Science and Technology*, vol. 5, no. 1, p. 37, 1996.

[171] M. Bacal, "Photodetachment diagnostic techniques for measuring negative ion densities and temperatures in plasmas," *Review of Scientific Instruments*, vol. 71, no. 11, pp. 3981–4006, 2000.

[172] K. Tsumori and M. Wada, "Diagnostics tools and methods for negative ion source plasmas, a review," *New Journal of Physics*, vol. 19, no. 4, p. 045002, 2017.

[173] P. Devynck, J. Auvray, M. Bacal, P. Berlemont, J. Bruneteau, R. Leroy, and R. A. Stern, "Photodetachment technique for measuring h^- velocities in a hydrogen plasma," *Review of Scientific Instruments*, vol. 60, no. 9, pp. 2873–2878, 1989.